

# The influence of morphology, AGN and environment on the quenching histories of galaxies



Rebecca Jane Smethurst  
Pembroke College  
University of Oxford

A thesis submitted for the degree of  
*Doctor of Philosophy*  
Michaelmas 2016

Oy with the poodles already!

## **Acknowledgements**

Thank ALLL TEH people. Including, for inspiration and the help with perseverance: T. Swift, B. Springsteen, C. Martin et al., Dr M. Grey, L. Gilmore, R. Gilmore, A. Haim et al., E. Sheeran,

## **Abstract**

GZ shit happens.

# Contents

<b>1</b>	<b>Introduction</b>	<b>1</b>
1.1	Galaxy Zoo . . . . .	3
1.1.1	Defining the GZ2-GALEX main galaxy sample . . . . .	6
<b>2</b>	<b>STARPY: Bayesian inference of a galaxy's star formation history</b>	<b>8</b>
2.1	Star Formation History Models . . . . .	8
2.2	Probabilistic Fitting Methods . . . . .	13
2.2.1	A short introduction to Bayesian statistics . . . . .	13
2.2.2	STARPY . . . . .	15
2.3	Testing STARPY . . . . .	18
2.4	Speeding up STARPY . . . . .	21
2.5	POPSTARPY: studying populations of galaxies with STARPY . . . . .	22
2.5.1	Alternative Hierarchical Bayesian approach . . . . .	25
<b>3</b>	<b>The morphological dependance of quenching</b>	<b>31</b>
3.1	Defining the Green Valley . . . . .	32
3.2	Results . . . . .	38
3.2.1	The Red Sequence . . . . .	40
3.2.2	Green Valley Galaxies . . . . .	41
3.2.3	Blue Cloud Galaxies . . . . .	44
3.3	Discussion . . . . .	47
3.3.1	Rapid Quenching Rates . . . . .	48
3.3.2	Intermediate Quenching Rates . . . . .	49
3.3.3	Slow Quenching Rates . . . . .	52
3.4	Conclusions . . . . .	53
<b>4</b>	<b>Black hole-galaxy co-evolution in the context of quenching</b>	<b>55</b>
4.1	Rapid, recent quenching within a population of Type 2 AGN host galaxies	55
4.1.1	AGN Sample . . . . .	56
4.1.2	Defining a control sample . . . . .	60
4.1.3	Results . . . . .	62
4.1.4	Discussion . . . . .	66
4.2	Bulgeless galaxies hosting growing black holes . . . . .	72
4.2.1	Observational Data . . . . .	73
4.2.1.1	AGN Selection . . . . .	73

4.2.1.2	Selecting disc-dominated AGN host galaxies . . . . .	74
4.2.1.3	Spectra . . . . .	74
4.2.1.4	Selecting a Control Sample . . . . .	76
4.2.2	Galaxy and Black Hole Properties . . . . .	76
4.2.2.1	Photometry . . . . .	79
4.2.2.2	Total stellar masses . . . . .	80
4.2.2.3	Bulge stellar masses . . . . .	80
4.2.2.4	Black hole mass estimates . . . . .	83
4.2.2.5	Bolometric Luminosities . . . . .	85
4.2.3	Results . . . . .	87
4.2.4	Discussion . . . . .	92
4.3	Conclusions . . . . .	96
<b>5</b>	<b>The influence of the group environment</b>	<b>97</b>
5.1	Group Identification . . . . .	97
5.1.1	Field sample . . . . .	97
5.2	Results . . . . .	100
5.3	Discussion . . . . .	106
<b>6</b>	<b>Discussion</b>	<b>110</b>
<b>7</b>	<b>Conlusions</b>	<b>112</b>
7.1	Summary . . . . .	112
7.2	Future Work . . . . .	112
	<b>Bibliography</b>	<b>113</b>

# List of Figures

1.1	GZ2 classification decision tree . . . . .	4
1.2	GZ2-GALEX sample completeness . . . . .	5
1.3	Example SDSS images with GZ2 vote fractions . . . . .	5
2.1	SFH models in observational planes . . . . .	10
2.2	Predicted colours and SFRs of quenching models . . . . .	12
2.3	Is my coin biased? An example of the strength of Bayesian statistics .	14
2.4	Example STARPY output . . . . .	17
2.5	Testing STARPY . . . . .	19
2.6	Comparing complete and look-up table versions of STARPY . . . . .	20
2.7	Colours of discarded galaxies . . . . .	24
2.8	Replica colour-colour distributions using a hierarchical method . . . . .	27
2.9	Replica colour-colour distributions using the POPSTARPY method . .	28
3.1	Optical $u - r$ colour histograms in absolute r-band magnitude slices of the GZ2-GALEX and Baldry et al. (2004) complete SDSS samples . .	33
3.2	Colour-magnitude diagram showing the location of the Baldry et al. (2004) green valley definition . . . . .	34
3.3	SFR-stellar mass plane split by morphology and colour . . . . .	37
3.4	Population densities of red smooth and disc galaxies . . . . .	39
3.5	Population densities of green smooth and disc galaxies . . . . .	42
3.6	Time spent in the green valley across parameter space . . . . .	43
3.7	Population densities of blue smooth and disc galaxies . . . . .	45
3.8	Best fit contours for red, green and blue clean galaxies . . . . .	46
4.1	BPT diagram used to select AGN host galaxies . . . . .	56
4.2	Distribution of measured galaxy parameters in the AGN-HOST sample .	57
4.3	SDSS images of galaxies in the AGN-HOST sample . . . . .	58
4.4	Morphology and mass distributions of the AGN-HOST and INACTIVE samples . . . . .	60
4.5	Colour-magnitude and SFR-mass diagram for AGN-HOST galaxies . .	61
4.6	Quenching time and rate population density distributions for the AGN-HOST sample split by Eddington ratio . . . . .	62
4.7	Quenching time population density distributions for the AGN-HOST and INACTIVE samples . . . . .	63

4.8	Quenching rate population density distributions for the AGN-HOST and INACTIVE samples . . . . .	64
4.9	Galaxy luminosity function from observations and simulations: Figure 1 of Benson et al. (2003) . . . . .	70
4.10	SDSS images of DISKDOM sample . . . . .	75
4.11	SDSS images of 5 galaxies observed with the IDS on the INT . . . . .	76
4.12	Optical SDSS spectra of 5 galaxies in the DISKDOM sample . . . . .	77
4.13	Optical spectra of 5 bulgeless galaxies observed on the INT with the IDS	78
4.14	Redshift distribution of bulgeless galaxies . . . . .	79
4.15	Parametric fits and residuals for the 5 galaxies observed at the INT . .	81
4.16	Zoom in on $H\alpha$ region of the spectra of 5 galaxies observed with the IDS on the INT . . . . .	86
4.17	Galaxy and black hole properties of the DISKDOM sample in comparison to the QSOCONTROL sample . . . . .	87
4.18	Black hole stellar mass relation for the DISKDOM sample . . . . .	89
4.19	Black hole bulge mass relation for the DISKDOM sample . . . . .	90
4.20	Black hole mass against luminosity for the bulgeless AGN sample . .	91
4.21	Eddington ratio distribution of the bulgeless AGN sample . . . . .	92
4.22	Colour-magnitude diagram for the DISKDOM sample, coloured by black hole mass accretion rate . . . . .	93
5.1	SDSS images of galaxies in the GZ-GROUP and GZ-FIELD samples . .	98
5.2	Redshift distribution comparison of the GZ-GROUP sample and matched control GZ-CENT-FIELD-Q sample . . . . .	99
5.3	Mean GZ vote fractions for satellite galaxies with projected cluster centric radius . . . . .	100
5.4	Bar fraction of satellite disc galaxies with projected cluster centric radius	101
5.5	Merger fraction of satellite galaxies with projected cluster centric radius	102
5.6	GZ2 bulge fractions of satellite disc galaxies with projected cluster centric radius . . . . .	103
5.7	Median SFR of the GZ-GROUP sample with projected cluster centric radius . . . . .	104
5.8	The time since quenching of the GZ-GROUP sample with projected cluster centric radius . . . . .	107
5.9	The time since quenching of the GZ-GROUP sample with projected cluster centric radius . . . . .	108

# Chapter 1

## Introduction

Previous large scale surveys of galaxies have revealed a bimodality in the colour-magnitude diagram (CMD) with two distinct populations; one at relatively low mass, with blue optical colours and another at relatively high mass, with red optical colours (Baldry et al., 2004, 2006; Willmer et al., 2006; Ball et al., 2008; Brammer et al., 2009). These populations were dubbed the ‘blue cloud’ and ‘red sequence’ respectively (Chester & Roberts, 1964; Bower et al., 1992; Driver et al., 2006; Faber et al., 2007). The Galaxy Zoo project (Lintott et al., 2011), which produced morphological classifications for a million galaxies, helped to confirm that this bimodality is not entirely morphology driven (Strateva et al., 2001; Salim et al., 2007; Schawinski et al., 2007; Constantin et al., 2008; Bamford et al., 2009; Skibba et al., 2009), detecting larger fractions of spiral galaxies in the red sequence (Masters et al., 2010a) and elliptical galaxies in the blue cloud (Schawinski et al., 2009) than had previously been detected.

The sparsely populated colour space between these two populations, the so-called ‘green valley’, provides clues to the nature and duration of galaxies’ transitions from blue to red. This transition must occur on rapid timescales, otherwise there would be an accumulation of galaxies residing in the green valley, rather than an accumulation in the red sequence as is observed (Arnouts et al., 2007; Martin et al., 2007). Green valley galaxies have therefore long been thought of as the ‘crossroads’ of galaxy evolution, a transition population between the two main galactic stages of the star forming blue cloud and the ‘dead’ red sequence (Bell et al., 2004; Wyder et al., 2007; Schiminovich et al., 2007; Martin et al., 2007; Faber et al., 2007; Mendez et al., 2011;

Gonçalves et al., 2012; Schawinski et al., 2014; Pan et al., 2014).

The intermediate colours of these green valley galaxies have been interpreted as evidence for recent quenching (suppression) of star formation (Salim et al., 2007). Star forming galaxies are observed to lie on a well defined mass-SFR relation, however quenching a galaxy causes it to depart from this relation (Noeske et al. 2007; Peng et al. 2010).

By studying the galaxies which have just left this mass-SFR relation, I can probe the quenching mechanisms by which this occurs. There have been many previous theories for the initial triggers of these quenching mechanisms, including negative feedback from AGN (Di Matteo et al., 2005; Martin et al., 2007; Nandra et al., 2007; Schawinski et al., 2007), mergers (Darg et al., 2010; Cheung et al., 2012; Barro et al., 2013), supernovae winds (Marasco et al., 2012), cluster interactions (Coil et al., 2008; Mendez et al., 2011; Fang et al., 2013) and secular evolution (Masters et al., 2010a, 2011; Mendez et al., 2011). By investigating the *amount* of quenching that has occurred in the blue cloud, green valley and red sequence; and by comparing the amount across these three populations, I can apply some constraints to these theories.

The nature of the observed co-evolution of galaxies and their central supermassive black holes (Magorrian et al., 1998; Marconi & Hunt, 2003; Häring & Rix, 2004) and the effects of AGN feedback on galaxies are two of the most important open issues in galaxy evolution. AGN feedback was first suggested as a mechanism for regulating star formation in simulations (Silk & Rees, 1998; Croton et al., 2006; Bower et al., 2006; Somerville et al., 2008) and indirect evidence has been observed for both positive and negative feedback in various systems (see the comprehensive review from Fabian 2012).

The strongest observational evidence for AGN feedback in a population is that the largest fraction of AGN are found in the green valley (Cowie & Barger, 2008; Hickox et al., 2009; Schawinski et al., 2010), suggesting some link between AGN activity and the process of quenching which moves a galaxy from the blue cloud to the red sequence. However, concrete statistical evidence for the effect of AGN feedback on the host galaxy population has so far been elusive.

There are many mechanisms which are proposed to cause quenching; including mergers (Daddi et al., 2010), mass quenching (Kennicutt et al., 1987; Peng et al., 2012), morphological quenching (?) and the environment of a galaxy.

The galaxy environment as a cause of quenching was proposed due to the correlation of both morphology (Dressler, 1980) and the quenched galaxy fraction (?) with environmental density.

BUT does this correlation truly imply causation? Evidence from simulations (?) suggests that the environment may not be the dominant quenching mechanisms for galaxies. Perhaps the correlation of increased galaxy quenched fractions with environment is due to a combination of mergers, mass and morphological quenching. In denser environments, galaxies are more likely to encounter another galaxy in a merger scenario and large viral radii give rise to long infall times during which gas reservoirs can be depleted due to star formation.

To study this I need to look at how quenching timescale changes in groups and clusters of galaxies with different properties in order to isolate the cause of the density-morphology and density-SFR correlations.

## 1.1 Galaxy Zoo

In this investigation I use visual classifications of galaxy morphologies from the Galaxy Zoo 2<sup>1</sup> citizen science project (Willett et al., 2013), which obtains multiple independent classifications for each galaxy image; the full question tree is shown in Figure 1.1.

The Galaxy Zoo 2 (GZ2) project consists of 304,022 images from the SDSS DR8 (a subset of those classified in Galaxy Zoo 1; GZ1) all classified by *at least* 17 independent users, with the mean number of classifications standing at  $\sim 42$ . The GZ2 sample is more robust than the GZ1 sample and provides more detailed morphological classifications, including features such as bars, the number of spiral arms and the ellipticity of smooth galaxies. It is for these reasons I use the GZ2 sample, as opposed to the GZ1, allowing for further investigation of specific galaxy classes in the future.

The decision tree that users are led through whilst classifying galaxies with GZ2 is shown in Figure 1.1. The first task of GZ2 asks users to choose whether a galaxy is mostly smooth, is featured and/or has a disc or is a star/artefact. Unlike other tasks further down in the decision tree, every user who classifies a galaxy image will

---

<sup>1</sup><http://zoo2.galaxyzoo.org/>

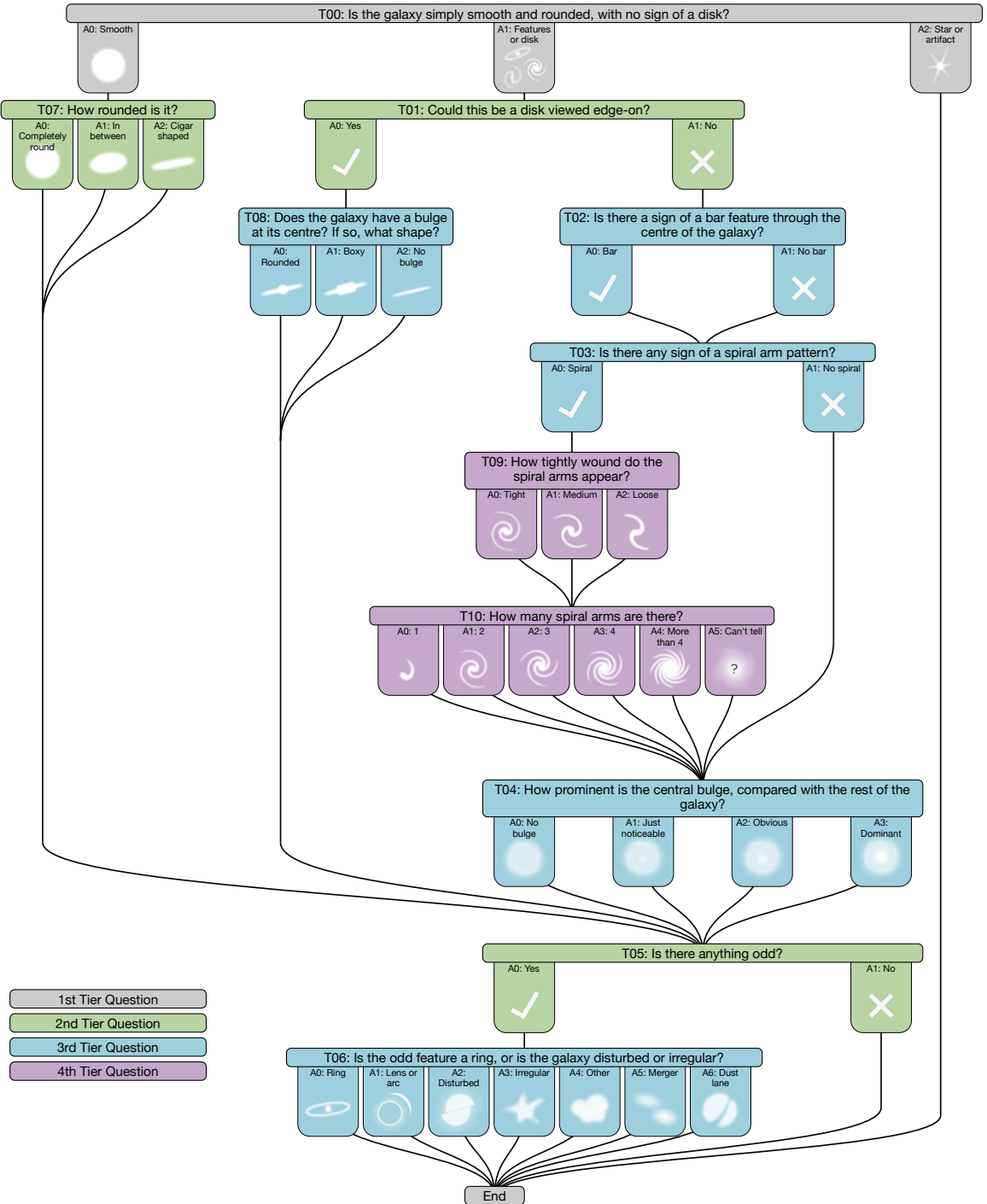


Figure 1.1: Flowchart of the classification tree for GZ2, beginning at the top. Tasks are colour-coded by their relative depths in the decision tree with tasks in green, blue and purple respectively one, two or three steps below branching points in the decision tree.

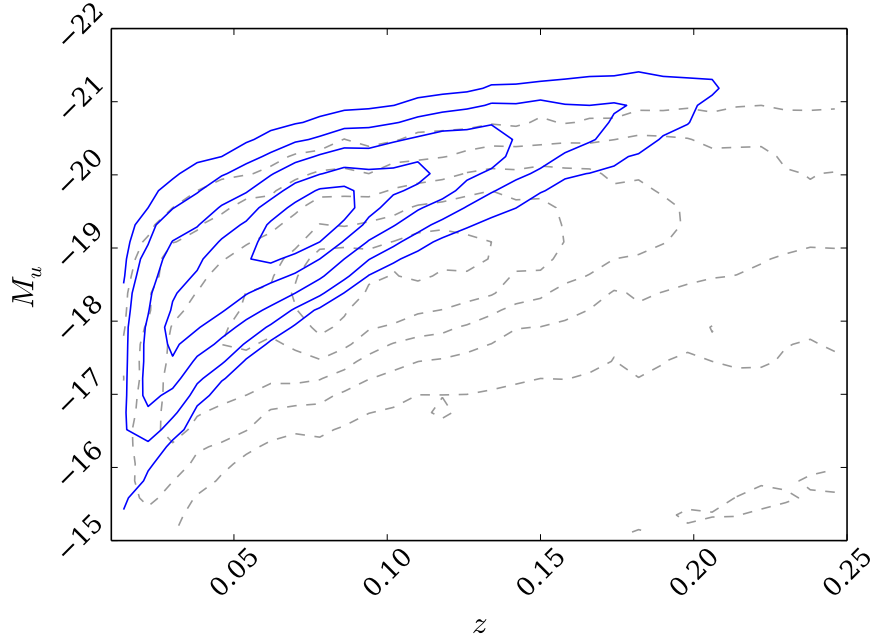


Figure 1.2: Absolute  $u$ -band magnitude against redshift for the whole of SDSS (grey dashed lines) in comparison to the GZ2 subsample (blue solid lines). Typical Milky Way  $L_*$  galaxies with  $M_u \sim -20.5$  are still included in the GZ2 subsample out to the highest redshift of  $z \sim 0.25$ .

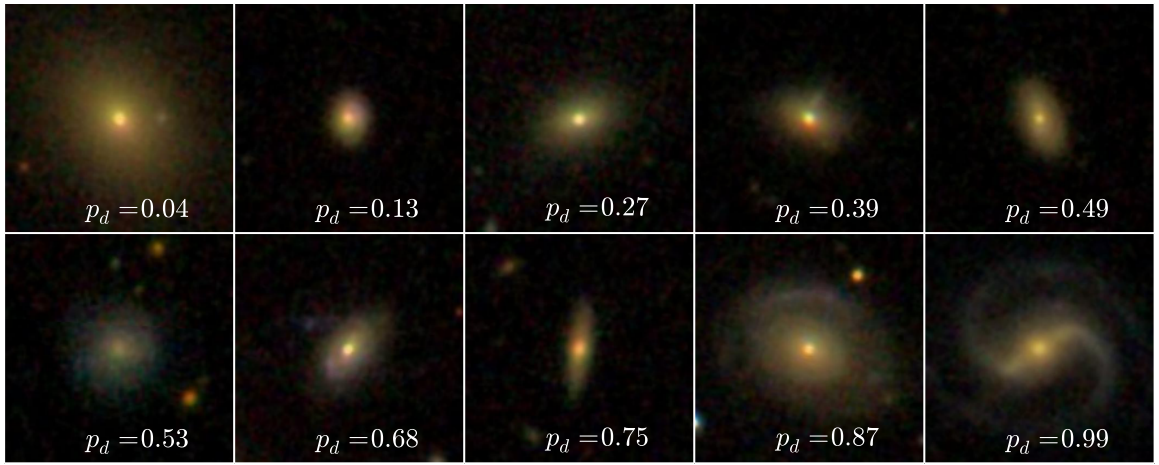


Figure 1.3: Randomly selected SDSS  $gri$  composite images showing the continuous probabilistic nature of the Galaxy Zoo sample from a redshift range  $0.070 < z < 0.075$ . The debiased disc vote fraction (see Willett et al. 2013) for each galaxy is shown. The scale for each image is 0.099 arcsec/pixel.

complete this task (others, such as whether the galaxy has a bar, is dependent on a user having first classified it as a featured galaxy). Therefore I have the most statistically robust classifications at this level.

The classifications from users produces a vote fraction for each galaxy (the debiased fractions calculated by Willett et al. (2013) were used in this investigation); for example if 80 of 100 people thought a galaxy was disc shaped, whereas 20 out of 100 people thought the same galaxy was smooth in shape (i.e. elliptical), that galaxy would have vote fractions  $p_s = 0.2$  and  $p_d = 0.8$ . In this example this galaxy would be included in the ‘clean’ disc sample ( $p_d \geq 0.8$ ) according to Willett et al. (2013) and would be considered a late-type galaxy. All previous Galaxy Zoo projects have incorporated extensive analysis of volunteer classifications to measure classification accuracy and bias, and compute user weightings (for a detailed description of debiasing and consistency-based user weightings, see either Section 3 of Lintott et al. 2009 or Section 3 of Willett et al. 2013).

The classifications are highly accurate and provide a continuous spectrum of morphological features, as shown in Figure 4.3, rather than a simple binary classification separating elliptical and disc galaxies. These classifications allow each galaxy to be considered as a probabilistic object with both bulge and disc components.

### 1.1.1 Defining the GZ2-GALEX main galaxy sample

The only selection that was made on the GZ2 sample was to remove objects considered to be stars, artefacts or merging pairs by the users (i.e. with  $p_{\text{star/artefact}} \geq 0.8$  or  $p_{\text{merger}} \geq 0.420$ ; see Willett et al. 2013 Table 3 and discussion for details of this fractional limit). Further to this, I required NUV photometry from the GALEX survey, within which  $\sim 42\%$  of the GZ2 sample were observed, giving a total sample size of 126,316 galaxies. This will be referred to as the GZ2-GALEX sample.

The completeness of the GZ2-GALEX sample is shown in Figure 1.2 with the  $u$ -band absolute magnitude against redshift, compared with the SDSS data set. Typical Milky Way  $L_*$  galaxies with  $M_u \sim -20.5$  are still included in the GZ2 subsample out to the highest redshift of  $z \sim 0.25$ ; however dwarf and lower mass galaxies are only detected at the lowest redshifts.

Galaxy colours were once again not corrected for intrinsic dust attenuation. This is of particular consequence for disc galaxies, where attenuation increases with increasing inclination. Buat et al. (2005) found the median value of the attenuation in the GALEX NUV passband to be  $\sim 1$  mag. Similarly Masters et al. (2010b) found a total extinction from face-on to edge-on spirals of 0.7 and 0.5 mag for the SDSS  $u$  and  $r$  passbands and show spirals with  $\log(a/b) > 0.7$  have signs of significant dust attenuation. For the AGN-HOST (INACTIVE) sample we find 23% (25%) of discs (with  $p_d > 0.5$ ) have  $\log(a/b) > 0.7$ , therefore we must be aware of possible biases in our results due to dust.

From the findings of Masters et al. (2010b) and Buat et al. (2005) above, I estimate the extinction to be  $u - r \sim 0.2$  mag and  $NUV - u \sim 0.3$  mag, therefore the average change in the SFH parameters across a range of input colours  $0 < u - r < 4$  and  $-1 < NUV - u < 5$ , are  $\Delta t_q = 0.985$  Gyr,  $\Delta \tau = 1.571$  Gyr. This change therefore causes the SFH parameters derived to move towards earlier times and faster quenching rates. Results should be viewed with the caveat, particularly for higher mass, disc galaxies, that earlier values of  $t_q$  and more rapid values of  $\tau$  may be inferred by STARPY. However, I note that (i) applying these average corrections across each sample population does not change our main conclusions, (ii) that results are consistent if the population of edge-on and face-on galaxies are compared (see Figure ?? and (iii) that results do not change if only face-on galaxies are used in the investigation, strongly suggesting that internal galactic extinction does not systematically bias our results.

# Chapter 2

## STARPY: Bayesian inference of a galaxy's star formation history

*The work in the following chapter has been published in Smethurst et al. (2015).*

### 2.1 Star Formation History Models

The quenched star formation history (SFH) of a galaxy can be simply modelled as an exponentially declining star formation rate (SFR) across cosmic time ( $0 \leq t$  [Gyr]  $\leq 13.8$ ) as:

$$SFR = \begin{cases} I_{sfr}(t_q) & \text{if } t < t_q \\ I_{sfr}(t_q) \times \exp\left(\frac{-(t-t_q)}{\tau}\right) & \text{if } t > t_q \end{cases} \quad (2.1)$$

where  $t_q$  is the onset time of quenching,  $\tau$  is the timescale over which the quenching occurs and  $I_{sfr}$  is an initial constant star formation rate dependent on  $t_q$ . A smaller  $\tau$  value corresponds to a rapid quench, whereas a larger  $\tau$  value corresponds to a slower quench. This model is not a fully hydrodynamical simulation, it is a deliberately simple model built in order to test our understanding of the evolution of galaxy populations. This SFH model has previously been shown to appropriately characterise quenching galaxies (Weiner et al., 2006; Martin et al., 2007; Noeske et al., 2007; Schawinski et al., 2014); but are not expected to accurately determine the SFH of every galaxy in the GZ2-GALEX sample, in particular galaxies which have not undergone

any quenching.

Here I assume that all galaxies formed at a time  $t = 0$  Gyr with an initial burst of star formation,  $I_{sfr}(t_q)$ . This initial constant star formation rate must be defined in order to ensure the ‘model’ galaxy has a reasonable stellar mass by  $z \sim 0$ . This value will therefore be dependent on the epoch at which quenching is modelled to occur, hence the  $I_{sfr}(t_q)$  in Equation 2.1. To tackle this problem, I looked to the literature; Peng et al. (2010, Equation 1) define a relation between the average sSFR and redshift (cosmic time,  $t$ ) by fitting to measurements of the mean sSFR of blue star forming galaxies from SDSS, zCOSMOS and literature values at increasing redshifts (Elbaz et al., 2007; Daddi et al., 2007):

$$sSFR(m, t) = 2.5 \left( \frac{m}{10^{10} M_\odot} \right)^{-0.1} \left( \frac{t}{3.5 \text{ Gyr}} \right)^{-2.2} \text{Gyr}^{-1}. \quad (2.2)$$

Beyond  $z \sim 2$  the characteristic SFR flattens and is roughly constant back to  $z \sim 6$ . This flattening can be seen across similar observational data (Peng et al., 2010; González et al., 2010; Béthermin et al., 2012) but the cause of it is poorly understood but may reflect a physical limit to the sSFR of a galaxy.

Motivated by these observations, the relation defined in Peng et al. (2010) is taken up to a cosmic time of  $t = 3$  Gyr ( $z \sim 2.3$ ) and prior to this a constant average SFR is assumed (see middle panel of Figure 2.1). At the point of quenching,  $t_q$ , the SFH models are therefore defined to have an  $I_{sfr}(t_q)$  which lies on this relationship for the sSFR, for a galaxy with mass,  $m = 10^{10.27} M_\odot$  (the mean mass of the GZ2-GALEX sample; see left panel of Figure 2.1). This choice of  $I_{sfr}(t_q)$  is an important one, however does not impact on the predicted colours output by the model (see below) as it is merely a normalisation factor on the SFH;  $[t_q, \tau]$ , which set the shape of the SFH, are the crucial parameters.

Under these assumptions the average SFR of these models will result in a lower value than the relation defined in Peng et al. (2010) at all cosmic times as each galaxy only resides on the ‘main sequence’ at the point of quenching. However galaxies cannot remain on the ‘main sequence’ from early to late times throughout their entire lifetimes given the unphysical stellar masses and SFRs that would result in the local Universe (Béthermin et al., 2012; Heinis et al., 2014). If prescriptions for starbursts, mergers, AGN etc. were included in this model, the reproduction of the average SFR across cosmic time would improve; however I have chosen to focus first on the simplest possible model.

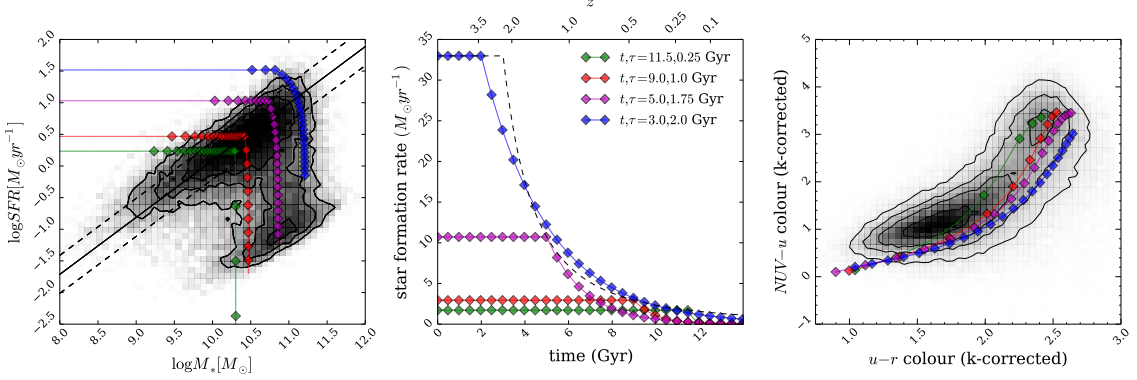


Figure 2.1: Left panel: SFR-stellar mass plane for all 126,316 galaxies in the GZ2-GALEX sample (shaded contours), with model galaxy trajectories shown by the coloured lines, with each point representing a time step of 0.5 Gyr. The ‘main sequence’ of star formation as defined by Peng et al. (2010) is shown by the solid line with  $\pm 1\sigma$  (dashed lines). Middle panel: The SFHs of the models are shown, where the SFR is initially constant before quenching at time  $t_q$  and thereafter exponentially declining with a characteristic timescale  $\tau$ . The SFR at the point of quenching is set to be consistent with the typical SFR of a star-forming galaxy at the quenching time,  $t_q$  (dashed curve; Peng et al. 2010). Right panel: The full range of models can reproduce the observed colour-colour properties of the GZ2-GALEX sample; for clarity the figures show only 4 of the possible models explored in this study. Note that some of the model tracks produce colours redder than the apparent peak of the red sequence in the GZ2 subsample; however this is not the *true* peak of the red sequence due to the necessity for NUV colours from GALEX (see Section 3.1.)

Once this SFH is obtained, it is convolved with the Bruzual & Charlot (2003) population synthesis models to generate a model SED at each time step. The observed features of galaxy spectra can be modelled using simple stellar population techniques which sum the contributions of individual, coeval, equal-metallicity stars. The accuracy of these predictions depends on the completeness of the input stellar physics. Comprehensive knowledge is therefore required of (i) stellar evolutionary tracks and (ii) the initial mass function (IMF) to synthesise a stellar population accurately.

These stellar population synthesis (SPS) models are an extremely well explored (and often debated) area of astrophysics (Maraston, 2005; Eminian et al., 2008; Conroy et al., 2009; Falkenberg et al., 2009; Chen et al., 2010; Kriek et al., 2010; Miner et al., 2011; Melbourne et al., 2012). In this work I have chosen to utilise the Bruzual & Charlot (2003) *GALEXEV* SPS models, along with a Chabrier IMF (Chabrier, 2003), across a large wavelength range ( $0.0091 < \lambda [\mu\text{m}] < 160$ ) with solar metallicity (m62 in the Bruzual & Charlot (2003) models; hereafter BC03), to allow a direct comparison with Schawinski et al. (2014).

Fluxes from stars younger than 3 Myr in the SPS model are suppressed to mimic the large optical depth of protostars embedded in dusty formation clouds (as in Schawinski et al. 2014). Filter transmission curves are then applied to the fluxes to obtain AB magnitudes and ultimately colours. For a particular galaxy at an observed redshift,  $z$ , I calculate the observed time,  $t^{obs}$  for that galaxy using the standard cosmological conversion between redshift and time provided in the *ASTROPY Python* module (Astropy Collaboration et al., 2013). The predicted colours of the SFH models at the observed redshift of each individual galaxy can then be compared to the observed colours directly, as in the right panel of Figure ???. Note that some of the SFHs shown produce colours redder than the apparent peak of the red sequence in the GZ2-GALEX sample; however this is not the *true* peak of the red sequence due to the necessity for NUV colours from GALEX (see Section 3.1). Star forming galaxies in this regime are fit by a constant SFR up until  $t_q \simeq t^{obs}$ , with a very low probability.

Figure 2.2 shows these predicted optical and NUV colours at a time of  $t^{obs} = 12.8$  Gyr (the average observed time of the GZ2-GALEX sample,  $z \sim 0.076$ ) for the exponential SFH model. These predicted colours will be referred to as  $d_{c,p}(t_q, \tau, t^{obs})$ , where  $c=\{\text{opt,NUV}\}$  and  $p = \text{predicted}$ . The SFR at a time of  $t^{obs} = 12.8$  Gyr is also shown in Figure 2.2 to compare how this impacts on the predicted colours. The  $u - r$  predicted colour shows an immediate correlation with the SFR, however the

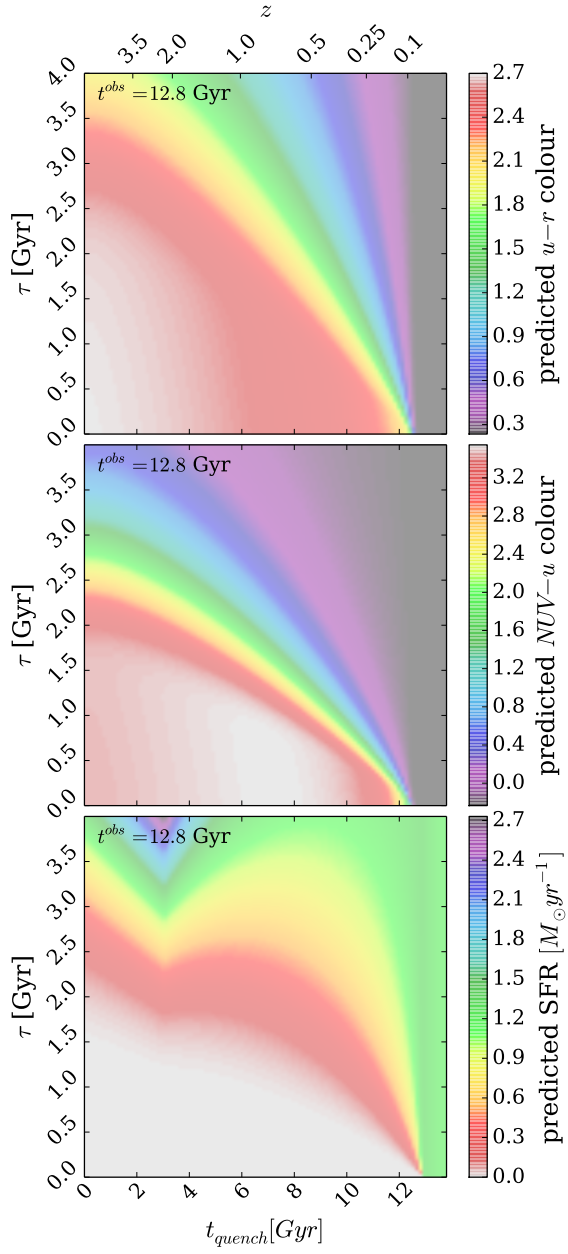


Figure 2.2: Quenching timescale  $\tau$  versus quenching onset time  $t_q$  in all three panels for the quenched SFH models used in STARPY. Colour shadings show model predictions of the  $u - r$  optical colour (top panel),  $NUV - u$  colour (middle panel), and star formation rate (lower panel), at  $t^{obs} = 12.8$  Gyr, the mean observed redshift of the GZ2 sample (see Section 2.1). The combination of optical and NUV colours is a sensitive measure of the  $\theta = [t_q, \tau]$  parameter space. Note that all models with  $t > 12.8$  Gyr are effectively un-quenched. The ‘kink’ in the bottom panel is due to the assumption that the sSFR is constant prior to  $t \sim 3$  Gyr ( $z \sim 2.2$ ).

$NUV - u$  colour is more sensitive to the value of  $\tau$  and so is ideal for tracing any recent star formation in a population . At small  $\tau$  (rapid quenching timescales) the  $NUV - u$  colour is insensitive to  $t_q$ , whereas at large  $\tau$  (slow quenching timescales) the colour is very sensitive to  $t_q$ . Together the two colours are ideal for tracing the effects of  $t_q$  and  $\tau$  in a population.

## 2.2 Probabilistic Fitting Methods

In order to achieve robust conclusions I conducted a Bayesian analysis (Sivia & Skilling, 2006; Mackay, 2003) of the predicted colours from the SFH models in comparison to the observed colours of the GZ2-GALEX sample.

### 2.2.1 A short introduction to Bayesian statistics

Frequentist statistics allows you to test whether an event (i.e. a hypothesis) occurs or not and calculate the probability of it occurring over many trials of an experiment. The accuracy of the derived probability is also dependant on the number of experiment trials conducted. Conversely, a Bayesian approach allows you to directly test whether a hypothesis,  $\theta$ , is true, given the data you already have,  $d$ , by relating this to something you can easily calculate: the probability that you would observe the data if the hypothesis was true. It does so by employing the rules of conditional probability into Bayes' theorem:

$$P(\theta|d) \propto P(d|\theta)P(\theta), \quad (2.3)$$

which is made up of three separate terms:

- (i)  $P(\theta)$ , known as the *prior* probability which represents your knowledge (or ignorance) about the hypothesis before you have analysed any data.
- (ii)  $P(d|\theta)$ , the *likelihood* function which gives the probability of observing the data you have given the hypothesis being tested.
- (iii)  $P(\theta|d)$ , the *posterior* probability which summarises your knowledge of the hypothesis given your observed data.

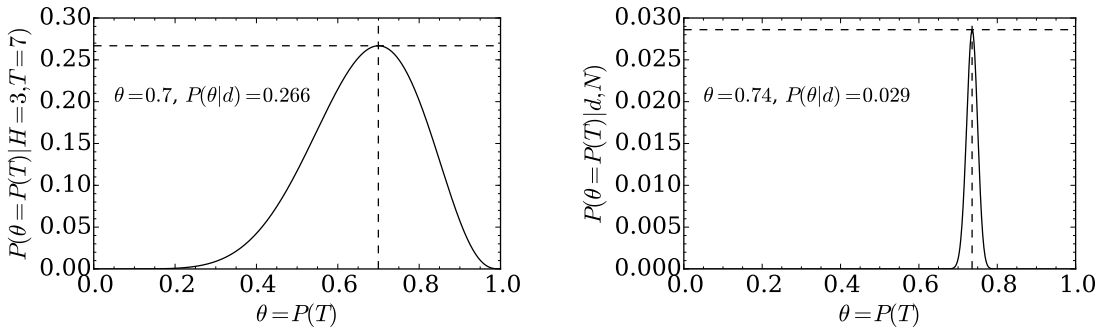


Figure 2.3: The unnormalised posterior probability calculated for multiple hypotheses for the probability of tossing a tails,  $P(T)$  in the case of 10 data points (left) and 1000 data points (right). The dashed lines in both cases show the posterior probability values at the peak of the distribution.

The missing normalisation constant in Equation 2.3 doesn't explicitly depend on your hypothesis and so doesn't have to be calculated for model parameter estimation problems (for example, where your hypothesis,  $\theta$ , is a model described by some number of parameters with the goal of emulating your data). Deciding on a prior and likelihood function is very much dependent on the problem you are trying to solve; the decision is often informed by your knowledge of the problem.

This difference between frequentist and Bayesian statistics is often highlighted by the example of a coin being tossed; if I toss a coin 10 times and get 3 heads ( $H = 3$ ) and 7 tails ( $T = 7$ ) what is the probability that the coin is weighted? With frequentist statistics, you are limited by the fact that I only tossed the coin 10 times; I haven't repeated the experiment enough for you to be sure of your response that the probability of tossing a tails,  $P(T) = 0.7$ . Perhaps if I'd tossed the coin a 1000 times and recorded 720 tails then you could be more certain that the coin was weighted. Herein lies the problem of frequentist statistics; not only is your answer dependent on the number of experiment trials but you also can't quantify how likely your answer is of being correct.

To quantify this you can use Bayesian statistics; first you need to choose your likelihood,  $P(d|\theta)$ , and your prior distributions,  $P(\theta)$ , but there are many choices available. For example, given that most coins that you encounter are not weighted, you might choose a Gaussian as your prior distribution, centered on  $P(T) = 0.5$ . Or, you may decide that all scenarios are equally likely and therefore choose a flat prior

distribution.

For the likelihood function you need to think about what hypothesis (or model,  $\theta$ ) best describes your problem. In this case you might choose a Bernouilli likelihood distribution, e.g.

$$P(d|\theta, N) = \theta^d (1 - \theta)^{N-d}, \quad (2.4)$$

where  $d$  is the number of tails flipped,  $\theta$  is our guess (or hypothesis) for  $P(T)$ , i.e. how biased the coin is, and  $N$  is the number of flips of the coin. If you calculate this likelihood,  $P(d|\theta, N)$  for many possible values of  $\theta = P(T)$  and multiply it by your flat prior distribution, you get the unnormalised posterior probability distribution shown in the left panel of Figure 2.3. From this you can see that  $P(T) = 0.7$  is indeed the most likely value for the probability of tossing a tails given the 10 data points you have. Not only have you been able to determine the best model to describe the coin, given the data you have, but have also been able to say how certain you are of this model (since this is an unnormalised posterior distribution you can't give a definitive probability but can say how certain you are in comparison to other  $\theta$  values). As you increase the number of trials in the experiment,  $N$ , you become more certain of your result, as in the right panel of Figure 2.3.

This is the strength of using a Bayesian method over a frequentist one. In particular, the output of a Bayesian analysis is probabilistic in nature, returning the posterior probability distribution across the model parameter space,  $\theta$  (in the example in Figure 2.3 this is demonstrated in one dimension, but this can be visualised over as many dimensions as needed in the problem). This distribution encodes a huge amount of useful information that can be utilised in the analysis of the hypothesis.

Since this investigation is focussed on finding the most likely star formation history model in a very degenerative parameter space for a large sample of galaxies, the obvious choice of method for analysis is therefore a Bayesian one.

### 2.2.2 STARPY

For the SFH problem at hand, using this Bayesian approach requires consideration of all possible combinations of the model parameters  $\theta \equiv (t_q, \tau)$  (the hypothesis in this instance). Assuming that all galaxies formed at  $t = 0$  Gyr with an initial burst of star formation, we can assume that the ‘age’ of each galaxy in the GZ2 sample is

equivalent to an observed time,  $t_k^{obs}$ . I then used this ‘age’ to calculate the predicted model colours at this cosmic time for a given combination of  $\theta$ :  $d_{c,p}(\theta_k, t_k^{obs})$  for both optical and NUV ( $c = opt, NUV$ ) colours. The predicted model colours can now directly be compared with the observed GZ2-GALEX sample colours, so that for a single galaxy  $k$  with optical ( $u - r$ ) colour,  $d_{opt,k}$  and NUV ( $NUV - u$ ) colour,  $d_{NUV,k}$ , I have chosen the likelihood of a given model  $P(d_k|\theta_k, t_k^{obs})$  to be:

$$P(d_k|\theta_k, t_k^{obs}) = \frac{1}{\sqrt{2\pi\sigma_{opt,k}^2}} \frac{1}{\sqrt{2\pi\sigma_{NUV,k}^2}} \exp \left[ -\frac{(d_{opt,k} - d_{opt,p}(\theta_k, t_k^{obs}))^2}{\sigma_{opt,k}^2} \right] \exp \left[ -\frac{(d_{NUV,k} - d_{NUV,p}(\theta_k, t_k^{obs}))^2}{\sigma_{NUV,k}^2} \right]. \quad (2.5)$$

Here I have assumed that  $P(d_{opt}|\theta_k, t_k^{obs})$  and  $P(d_{NUV}|\theta_k, t_k^{obs})$  are independent of each other and that the errors on the observed colours are also independent. To obtain the probability of a combination of  $\theta$  values given the GZ2 data:  $P(\theta_k|d_k, t^{obs})$ , i.e. how likely a single SFH model is given the observed colours of a single GZ2 galaxy, I utilise Bayes’ theorem as:

$$P(\theta_k|d_k, t^{obs}) = \frac{P(d_k|\theta_k, t^{obs})P(\theta_k)}{\int P(d_k|\theta_k, t^{obs})P(\theta_k)d\theta_k}. \quad (2.6)$$

I assume a flat prior on the model parameters so that:

$$P(\theta_k) = \begin{cases} 1 & \text{if } 0 \leq t_q \text{ [Gyr]} \leq 13.8 \text{ and } 0 \leq \tau \text{ [Gyr]} \leq 4 \\ 0 & \text{otherwise.} \end{cases} \quad (2.7)$$

As the denominator of Equation 2.6 is a normalisation factor, comparison between likelihoods for two different SFH models (i.e., two different combinations of  $\theta_k = [t_q, \tau]$ ) is equivalent to a comparison of the numerators. Markov Chain Monte Carlo (MCMC; Mackay 2003; Foreman-Mackey et al. 2013; Goodman & Weare 2010) provides a robust comparison of the likelihoods between  $\theta$  values.

MCMC allows for a more efficient exploration of the parameter space by avoiding those areas with low likelihood. A large number of ‘walkers’ are started at an initial position (i.e. an initial hypothesis,  $\theta$ ), where the likelihood is calculated; from there they individually ‘jump’ a randomised distance to a randomised new area of parameter space. If the likelihood in this new position is greater (less) than the original

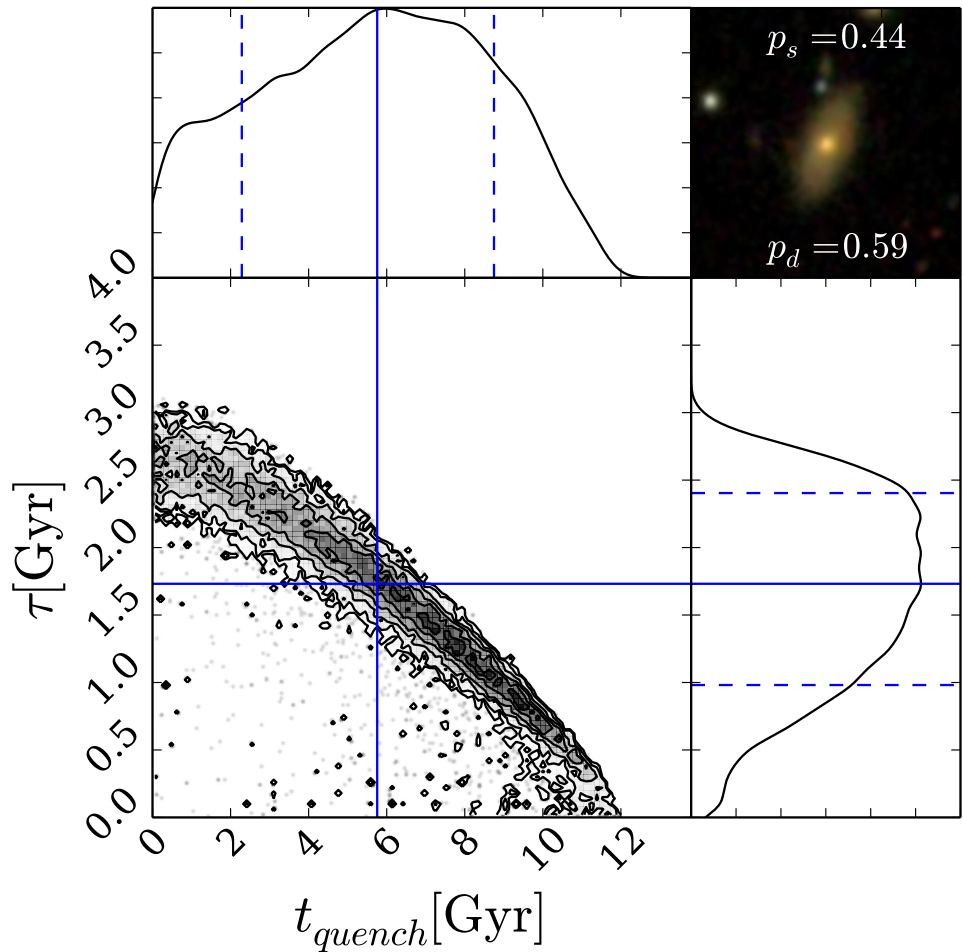


Figure 2.4: Example output from STARPY for a galaxy within the red sequence. The contours show the positions of the ‘walkers’ in the Markov Chain (which are analogous to the areas of high probability) for the quenching models described by  $\theta = [t_q, \tau]$ . The histograms show the 1D projection along each axis. Solid (dashed) blue lines show the best fit parameters (with  $\pm 1\sigma$ ) to the data. The postage stamp image from SDSS is shown in the top right along with the debiased vote fractions for smooth ( $p_s$ ) and disc ( $p_d$ ) from Galaxy Zoo 2.

position then the ‘walkers’ accept (reject) this change in position. Any new position then influences the direction of the ‘jumps’ of other walkers (this is the case in ensemble MCMC as used in this investigation but not for simple MCMC, which is much slower at converging). This is repeated for the defined number of steps after an initial ‘burn-in’ phase. The length of this burn-in phase is determined after sufficient experimentation to ensure that the ‘walkers’ had converged on a region of parameter space. I chose to use *emcee*,<sup>1</sup> a Python module which implements an affine invariant ensemble sampler to explore the parameter space, written by Foreman-Mackey et al. (2013). *emcee* outputs the positions of these ‘walkers’ in the parameter space, which are analogous to the regions of high posterior probability.

The routine outlined above has been coded using the *Python* programming language into a package named STARPY which has been released with an open source license<sup>2</sup>. An example output from this module for a single galaxy from the GZ2-GALEX sample in the red sequence is shown in Figure 2.2.2 wherein the degeneracies of the SFH model can be clearly seen and reflect those seen in the colours in Figure 2.2. These degeneracies are present for all galaxies run through STARPY therefore if differences in the distributions arise when comparing two galaxies (or two populations), this is due to intrinsic differences in their SFHs and not due to the degeneracies of the model.

## 2.3 Testing STARPY

In order to test that STARPY can find the correct quenching model for a given observed colour, 25 synthesised galaxies were created with known SFHs (i.e. known values of  $\theta = [t_q, \tau]$ ) from which optical and NUV colours were generated using the BC03 SPS models. These were input into STARPY to test whether the known values of  $\theta$  were reproduced, within error, for each of the 25 synthesised galaxies. Figure 2.5 shows the results for each of these synthesised galaxies, with the known values of  $\theta$  shown by the red lines (the largest difference between the known and derived values being  $[\Delta t_q, \Delta \tau] \approx [4.5, 2.0]$ ). In some cases this red line does not coincide with the inferred best fit  $\theta$  values shown by the blue lines, however in all cases the intersection of the red lines (i.e. the known or true values input) resides within the parameter space explored

---

<sup>1</sup>[emcee13.iel.fm/emcee/](https://github.com/aeli13/iel.emcee)

<sup>2</sup>[github.com/zooniverse/starp](https://github.com/zooniverse/starp)

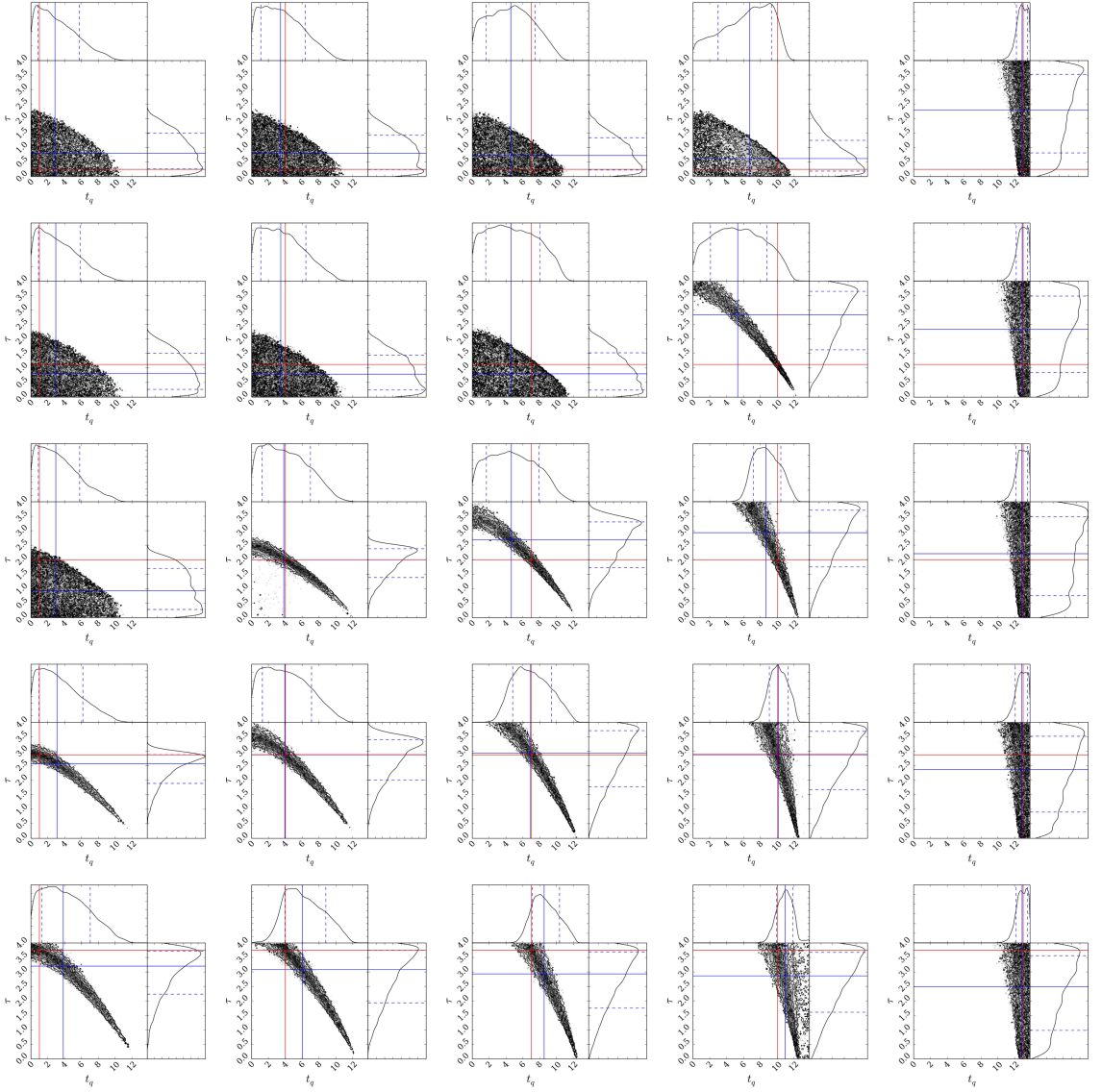


Figure 2.5: Results from STARPY for an array of synthesised galaxies with known, i.e. true,  $t_q$  and  $\tau$  values (marked by the red lines) using the complete function to calculate the predicted colour of a proposed set of  $\theta$  values in each MCMC iteration, assuming an error on the calculated known colours of  $\sigma_{u-r} = 0.124$  and  $\sigma_{NUV-u} = 0.215$  (the average errors on the GZ sample colours). I also assume that each synthesised galaxy has been observed at a redshift of  $z = 0$ . In each case STARPY succeeds (50th percentile best fit parameters are shown by the blue lines) in locating the true parameter values within the degeneracies of the star formation history model.

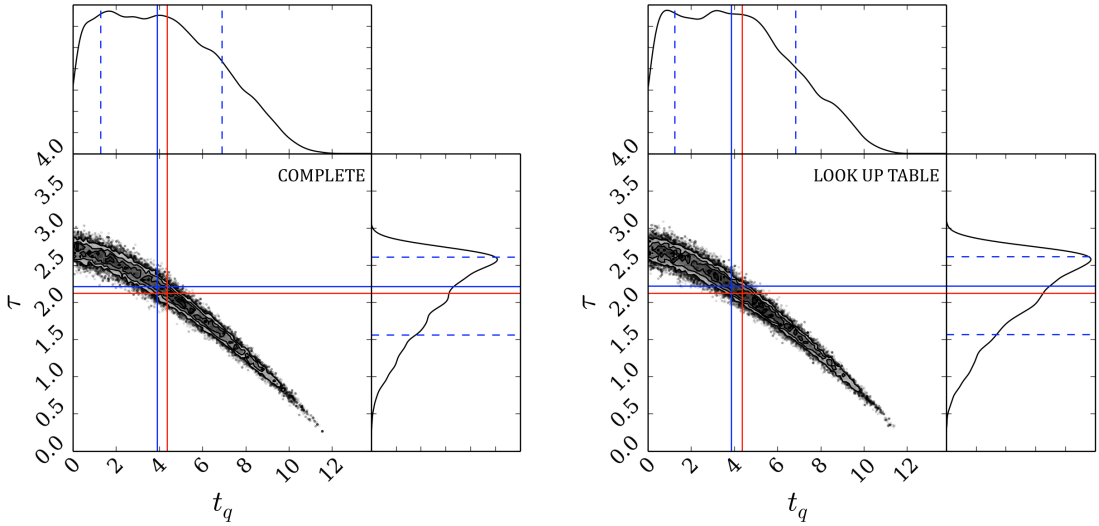


Figure 2.6: Left panel: Results from STARPY for true  $t_q$  and  $\tau$  values (red lines) using the complete function to calculate the predicted colour of a proposed set of  $\theta$  values in each MCMC iteration. The median walker position (the 50th percentile of the Bayesian probability distribution) is shown by the solid blue line with the dashed lines encompassing 68%( $\pm 1\sigma$ ) of the samples (the 16th and 84th percentile positions). The time taken to run for a single galaxy using this method is approximately 2 hours. Right panel: Results from STARPY for true  $t_q$  and  $\tau$  values using a look up table generated from the complete function to calculate the predicted colour of a proposed set of  $\theta$  values in each MCMC iteration. The time taken to run for a single galaxy using this method is approximately 2 minutes.

by the walkers, which trace the region of highest posterior probability. Therefore STARPY succeeds in locating the true parameter values within the degeneracies of the SFH model.

## 2.4 Speeding up STARPY

I wish to consider the SFH model parameters for a large populations of galaxies across the colour magnitude diagram, however for each combination of  $\theta$  values which *emcee* proposes for a single galaxy, a new SFH must be built, prior to convolving it with the BC03 SPS models at the observed age and then predicted colours calculated from the resultant SED. For a single galaxy this takes up to 2 hours on a typical

Table 2.1: Median walker positions (the 50th percentile; as shown by the blue solid lines in Figure 2.6) found by STARPY for a single galaxy, using the complete star formation history function and a look up table to speed up the run time. The errors quoted define the region in which 68% of the samples are located (blue lines in Figure 2.6). The known true values are also quoted, as shown by the red lines in Figure 2.6. All values are quoted to three significant figures.

	$t_q$	$\tau$
True	4.37	2.12
Complete	$3.893 \pm^{3.014}_{2.622}$	$2.215 \pm^{0.395}_{0.652}$
Look up table	$3.850 \pm^{2.988}_{2.619}$	$2.218 \pm^{0.399}_{0.649}$

desktop machine for long Markov Chains. A 3-dimensional look-up table was therefore generated at 50  $t^{obs}$ , 100  $t_{quench}$  and 100  $\tau$  values; which were interpolated over for a given observed galaxy’s age and proposed  $\theta$  values at each step in the Markov Chain. This ensured that a single galaxy SFH takes approximately 2 minutes to infer on a typical desktop machine.

Figure 2.6 shows one example of how using the look up table in place of the full function does not affect the results to a significant level. Table 2.1 quotes the median walker positions (the 50th percentile of the Bayesian probability distribution) along with their  $\pm 1\sigma$  ranges for both methods in comparison to the true values specified to test STARPY. The uncertainties incorporated into the quoted values by using the look up table are therefore minimal with a maximum  $\Delta = 0.043$  (the difference between the complete & look up table derived values quoted in Table 2.1). This test was run with 1000 randomised  $[t_q, \tau]$  values across the entire parameter space; the example shown in Figure 2.6 (with values quoted in Table 2.1) was found to have the largest difference between complete and look up table derived values,  $\Delta$ .

Using this lookup table, each of the 126,316 total galaxies in the GZ2-GALEX sample was run through STARPY on multiple cores of a computer cluster to obtain the Markov Chain positions (analogous to  $P(\theta_k|d_k)$ ) for each galaxy,  $k$  (see Figure 2.2.2). In each case the Markov Chain consisted of 100 ‘walkers’ which took 400 steps in the ‘burn-in’ phase and 400 steps thereafter, at which point the MCMC acceptance fraction was checked to be within the range  $0.25 < f_{acc} < 0.5$  (the fraction of proposed walker ‘jumps’ that were accepted), which was true in all cases. This acceptance fraction ensures that the walkers are sampling the probability space correctly as they

explore. If  $f_{acc} \sim 0$  then all the walker jumps are rejected and so the walkers won't move from their initial starting positions and the output will not represent the posterior distribution accurately. If  $f_{acc} \sim 1$  then all jumps are accepted and the walkers will just be performing a random walk around the parameter space, which again will not represent the posterior distribution accurately. The range of  $0.25 < f_{acc} < 0.5$  used in this case is the general rule of thumb stated by Gelman, Roberts, & Gilks (1996).

## 2.5 POPSTARPY: studying populations of galaxies with STARPY

To study the SFH of a large population of galaxies, the individual galaxy walker positions output by STARPY (analogous to the posterior probability distribution) are combined across  $[t, \tau]$  space. The Markov Chain walker positions are binned and weighted by their corresponding logarithmic posterior probability  $\log[P(\theta_k|d_k)]$ , provided by the *emcee* package, in order to emphasise the features and differences between various populations. This weighting by  $\log[P(\theta_k|d_k)]$  is to minimise the contribution of galaxies poorly fit by this exponentially declining SFH (e.g. star forming galaxies). This is no longer inference of model parameters but merely a method to visualise the results across a population of galaxies (see Section 2.5.1).

I also discard those walker positions with a corresponding normalised posterior probability of  $P(\theta_k|d_k) < 0.2$  in order to exclude galaxies which are not well fit by the quenching model, therefore galaxies in each sample which reside on the main sequence will not contribute to the final population distribution of quenching parameters. This raises the issue of whether I exclude a significant fraction of the GZ2-GALEX sample and whether those galaxies reside in a specific location of the colour-magnitude diagram. The fraction of galaxies which had all or more than half of their walker positions discarded due to low probability are shown in Table 2.2. Using the  $P(\theta_k|d_k) < 0.2$  constraint, 2.4%, 7.0% and 5.4% of green, red and blue galaxies respectively had *all* of their walker positions discarded.

This is not a significant fraction of any population, therefore the STARPY module is effective in fitting the majority of galaxies and this method of discarding walker positions ensures that poorly fit galaxies are removed from the analysis of the results. Figure 2.7 shows that these galaxies with discarded walker positions are also scattered

Table 2.2: The number of galaxies in each population which had walker positions discarded due to low posterior probability values in order to exclude those galaxies from the analysis which were poorly fit by the SFH quenching model.

	<b>Red Sequence</b>	<b>Green Valley</b>	<b>Blue Cloud</b>
All walkers discarded	1420 (7.00%)	437 (2.41%)	3109 (5.37%)
More than half walker positions discarded	2010 (9.92%)	779 (4.30%)	6669 (11.52%)

across the optical-NUV colour-colour diagram and therefore STARPY is also effective in fitting galaxies across this entire plane. The galaxies that are discarded can be seen to mostly lie outside the contours of the GZ2-GALEX sample in the colour-colour plane shown in Figure 2.7. This is due to the SPS models used to produce the SEDs of the model SFHs; these models are calibrated with typical galaxies rather than the extremes of galaxy evolution. Those galaxies with red (blue) optical colours but blue (red) NUV colours are oddities which cannot be explained by the SPS models and so STARPY has particular difficulty fitting a SFH to these galaxies.

Figure 2.5 shows how peaks in the histograms are found across all areas of the parameter space in both dimensions  $[t, \tau]$ , ensuring that any conclusions drawn from combined population distributions are due to a superposition of extended probability distributions, as opposed to a bimodal distribution of probability distributions across all galaxies.

I also utilise the GZ2 debiased user vote fractions to obtain separate population density distributions for both smooth and disc galaxies. This is obtained by also weighting by the morphology vote fraction of each individual galaxy when the binned walker positions of each galaxy in a population are combined. This ensures that the entirety of the GZ2-GALEX sample is used, negating the need for a threshold on the GZ2 vote fractions (e.g.,  $p_d > 0.8$  as used in Schawinski et al., 2014) to give two separate definitively disc and smooth galaxy populations. This ensures that those galaxies of intermediate morphology are still included in the analysis. The walkers of those galaxies with a higher morphological vote fraction,  $p_d$  ( $p_s$ ), are weighted more heavily and so contribute more to the disc (smooth) weighted combined walker distributions. These distributions will be referred to as the population densities.

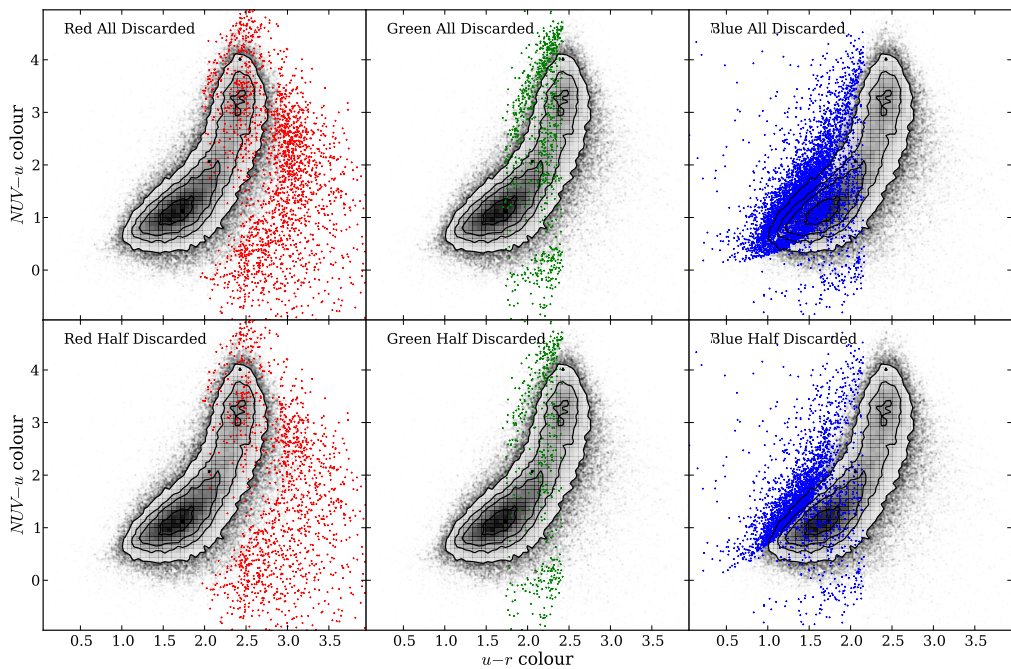


Figure 2.7: Contours show the GZ2-GALEX sample optical-NUV colour-colour diagram. The points show the positions of the galaxies which had all (top panels) or more than half (bottom panel) of their walker positions discarded due to their low probability for the red sequence (left), green valley (middle) and blue cloud (right).

For example, the galaxy shown in Figure 2.2.2 would contribute almost evenly to both the smooth and disc parameters due to the GZ2 vote fractions. Since galaxies with similar vote fractions contain both a bulge and disc component, this method is effective in incorporating intermediate galaxies which are thought to be crucial to the morphological changes between early- and late-type galaxies. It was the consideration of these intermediate galaxies which was excluded from the investigation by Schawinski et al. (2014).

### 2.5.1 Alternative Hierarchical Bayesian approach

The approach presented above relies upon a visualisation of the SFHs across each population, with no inference involved beyond the use of STARPY to derive the individual galaxy SFHs. An alternative approach to this problem would be to use a hierarchical Bayesian method to determine the ‘hyper-parameters’ that describe the distribution of the parent population  $\theta' = [t'_q, \tau']$  that each individual galaxy’s SFH is drawn from.

The posterior PDF for  $\vec{\theta}'$  to describe such a galaxy population:

$$P(\vec{\theta}'|\vec{d}) = \frac{P(\vec{d}|\vec{\theta}')P(\vec{\theta}')}{P(\vec{d})}, \quad (2.8)$$

where  $\vec{d}$  represents all of the optical and NUV colour data in a population  $\{\vec{d}_k\}$ . For one galaxy,  $k$ , the marginalised likelihood is:

$$P(d_k|\vec{\theta}') = \iint P(d_k|t_k, \tau_k)P(t_k, \tau_k|\vec{\theta}') \, dt_k \, d\tau_k \quad (2.9)$$

and for all galaxies,  $N$ , therefore:

$$P(\vec{d}|\vec{\theta}') = \prod_k^N P(d_k|\vec{\theta}'). \quad (2.10)$$

Using STARPY for an individual galaxy,  $k$  the output is the ‘interim’ posterior  $P(t_k, \tau_k|d_k)$  which I can relate to  $P(d_k|t_k, \tau_k)$  so that:

$$P(d_k|\vec{\theta}') = \iint P(t_k, \tau_k|d_k).P(d_k).\frac{P(t_k, \tau_k|\vec{\theta}')}{P(t_k, \tau_k)} \, dt_k \, d\tau_k. \quad (2.11)$$

In order to calculate this I draw  $N_s$  random samples,  $r$ , from each interim posterior,  $P(t_k, \tau_k | d_k)$  so that Equation 2.11 can be expressed as a sum over a number of random samples,  $N_s$  (as with the calculation of an expected mean):

$$P(d_k | \vec{\theta}') = \frac{P(d_k)}{N_s} \sum_r^{N_s} \frac{P(t_{k,r}, \tau_{k,r} | \vec{\theta}')}{P(t_k, \tau_k)}, \quad (2.12)$$

for the  $r^{th}$  sample of  $N_s$  total samples taken from one galaxy's,  $k$ , interim posterior PDF. This fraction is known as the 'importance weight',  $w_r$ , in importance sampling.

However, I also have two morphological vote fractions that I can weight by to determine separate hyper-parameters,  $\vec{\theta}' = [\vec{\theta}_d', \vec{\theta}_s']$ , for both disc,  $d$ , and smooth,  $s$ , galaxies. Therefore:

$$w_r = \frac{P(t_{k,r}, \tau_{k,r} | \vec{\theta}')}{P(t_k, \tau_k)} = \frac{p_{d,k} P(t_{k,r}, \tau_{k,r} | \vec{\theta}_d') + p_{s,k} P(t_{k,r}, \tau_{k,r} | \vec{\theta}_s')}{P(t_k, \tau_k)} \quad (2.13)$$

If we substitute equation 2.12 into equation 2.8 we find that the  $P(d_k)$  terms cancel and we are left with:

$$P(\vec{\theta}' | \vec{d}) = P(\vec{\theta}') \prod_k^N \frac{1}{N_{s,k}} \sum_r^{N_s} w_r, \quad (2.14)$$

where  $P(\vec{\theta}')$  is the assumed prior on the hyper-parameters, which is assumed to be uniform.

This approach is heavily dependent on what shape is assumed for the hyper-distribution; a decision which is not trivial. It is often common for this function to take the form of a multi-component Gaussian mixture model (Mackay, 2003; Lahav et al., 2000). For example a two component Gaussian mixture model in  $[t, \tau]$  space is described by eight hyper-parameters for a single morphology,  $\vec{\theta}' = [\mu_{t,1}, \sigma_{t,1}, \mu_{\tau,1}, \sigma_{\tau,1}, \mu_{t,2}, \sigma_{t,2}, \mu_{\tau,2}, \sigma_{\tau,2}]$ . This approach assumes no covariance between hyper-parameters for simplicity. The equations outlined above, combined with MCMC methods can be used to infer these  $8\vec{\theta}'$  parameters from which the hierarchical population distribution can be determined.

In order to test whether this assumption of a multi-component Gaussian mixture model is appropriate, I sampled the inferred hierarchical distributions to produce replica datasets in optical-NUV colour space. These are shown here in Figure 2.8

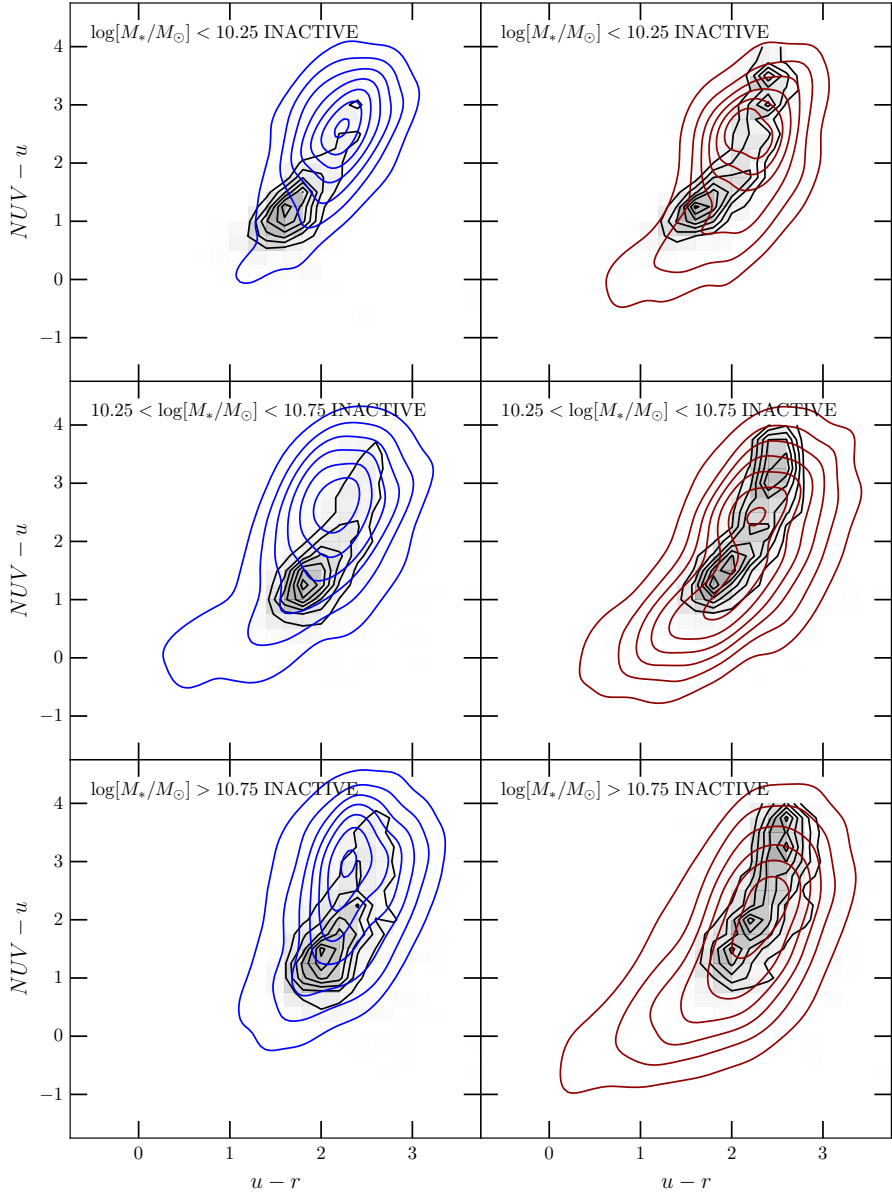


Figure 2.8: Optical-NUV colour-colour diagrams for the INACTIVE galaxies shown by the black contours, split into low mass (top), medium mass (middle) and high mass (bottom) galaxies weighted by  $p_d$  (left) and  $p_s$  (right). Kernel smoothing has been applied to the overlaid replica datasets, which are created by sampling from the **inferred 2 component Gaussian mixture model hierarchical parent distributions**. Gaussian random noise is also added to the inferred colours, with a mean and standard deviation of the errors on the observed colours of the respective sample. Contours are shown for samples taken from the disc (blue) and smooth weighted (red) inferred hierarchical distributions.

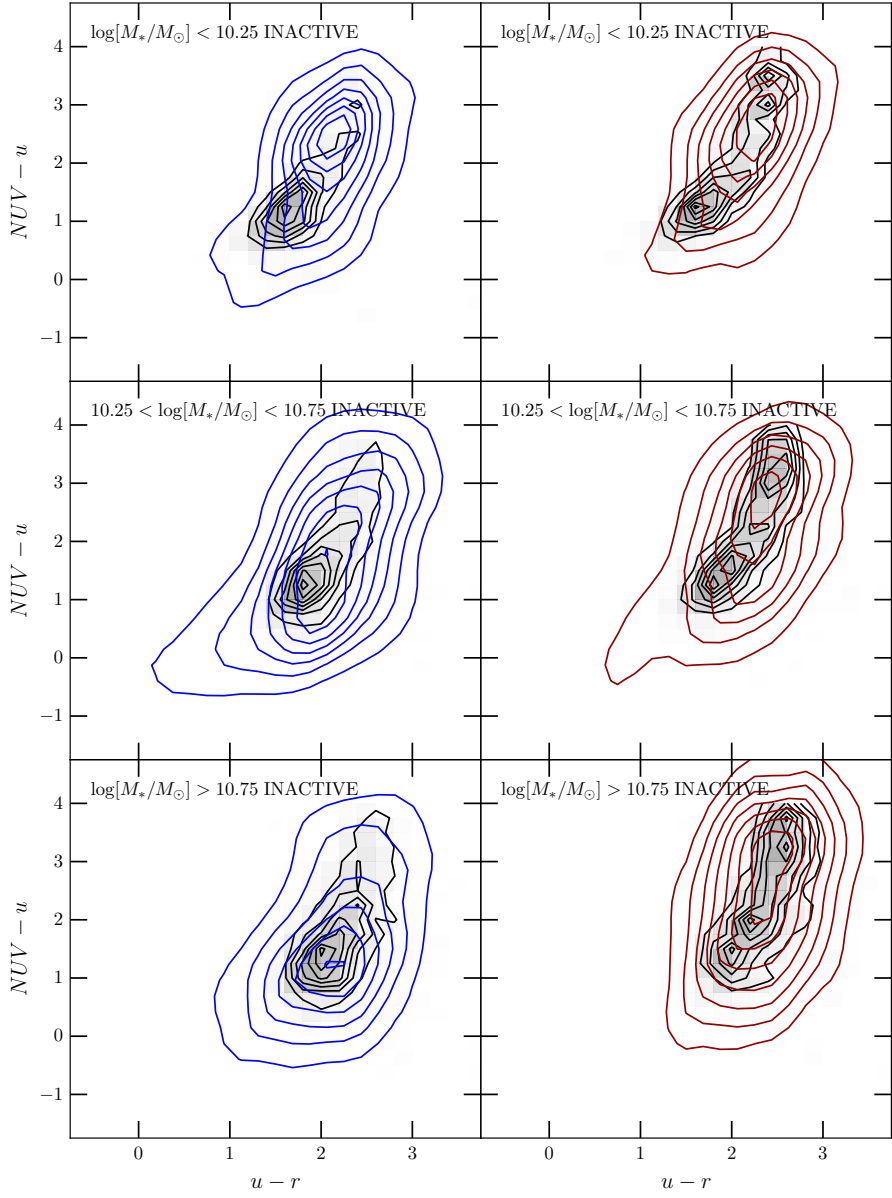


Figure 2.9: Optical-NUV colour-colour diagrams for the INACTIVE galaxies shown by the black contours, split into low mass (top), medium mass (middle) and high mass (bottom) galaxies weighted by  $p_d$  (left) and  $p_s$  (right). Kernel smoothing has been applied to the overlaid replica datasets, which are created by sampling from the **popstarpy population density distributions described in Section 2.5**. Gaussian random noise is also added to the inferred colours, with a mean and standard deviation of the errors on the observed colours of the respective sample. Contours are shown for samples taken from the disc (blue) and smooth weighted (red) inferred hierarchical distributions.

in comparison to the observed colour-colour distributions of the INACTIVE sample (a subset of  $\sim 6,000$  galaxies from the GZ2-GALEX sample, see Section 4). For all masses and morphologies the replicated  $u - r$  and  $NUV - u$  colours do not accurately match the observed data.

I also varied the value of  $N_s$  and found that increasing the number of samples drawn did not improve this fit for the INACTIVE population. Similarly increasing the number of components in the Gaussian mixture model did not immediately improve the accuracy of the fit along with other functional forms which require too many assumptions to be made about the shape of the parent distribution. I therefore concluded that assuming any functional form of the population distribution was unsatisfactory.

The POPSTARPY approach described in section 2.5 was motivated by the investigation increasing the number of samples,  $N_s$  drawn from the posterior of each galaxy,  $k$ , until the point where all the samples were drawn. Instead of attempting to infer parameters to describe this distribution, as above, I presented the combined distributions of all individual galaxies in a population (as described in Section 2.5). The distributions produced by this visualisation method reveal the complexity that the parent distribution must describe which, as concluded earlier, cannot be effectively modelled.

I also tested whether the POPSTARPY method is reasonable by producing replica datasets in optical-NUV colour space, as before, by drawing 1000  $[t, \tau]$  values from the population density distributions derived for the INACTIVE sample (see Section 4). These replica datasets are shown here in Figure 2.9 in comparison to the observed colour-colour distributions of the INACTIVE sample. Comparing these replica colours in Figure 2.9, with those produced by drawing from the inferred hierarchical distributions, shown in Figure 2.8, they can be seen to produce a more accurate match to the observed data for the majority of masses and morphologies.

Considering these issues with assuming a functional form for the hierarchical parent distribution, an expansion on this approach would be to perform ‘heat map optimization’, similar to image reconstruction, to determine the parent distribution for a given population. The population parameter space would be divided into an NxN grid of pixels and the value of each pixel would be a model parameter to be inferred by hierarchical Bayesian methods. Each pixel would need a prior (e.g. a basic entropic

prior) and the heat map would sum to unity. In order for this pixel map to accurately characterise the detail expected in the parent populations, this pixel grid would need to be sufficiently large, with at least a 50x50 grid of pixels (i.e. upwards of 2500 model parameters,  $\theta'$  to be inferred). This is a significant expansion upon the work presented here and is something the author wishes to investigate in future work.

For the results presented in the following chapters, I therefore use the POPSTARPY method to visualise the population distribution, rather than quoting inferred values to describe it.

# Chapter 3

## The morphological dependance of quenching

*The work in the following chapter has been published in Smethurst et al. (2015).*

By studying the galaxies which have just left the ‘main sequence’ of star formation (see top panel of Figure 2.1), the nature of the quenching mechanisms which cause this departure can be probed. By investigating the *amount* of quenching that has occurred in the blue cloud, green valley and red sequence; and by comparing that amount across the three populations, we can apply constraints to the many possible quenching mechanisms outlined in Chapter 1.

I have been motivated by a recent result suggesting there are two contrasting evolutionary pathways through the green valley for different morphological types (Schawinski et al. 2014, hereafter S14). S14 used the same exponentially declining star formation model, as described in Section 2.1, to obtain predicted optical and NUV colours for four possible SFHs through the green valley; two with fast quenching rates ( $\tau = [0.001, 0.25]$  Gyr) and two with slower quenching rates ( $\tau = [1, 2.5]$  Gyr). These predicted colours were then compared to observed colours of early- and late-type green valley galaxy colours on an optical-NUV colour-colour diagram. They concluded from this diagram that late-type galaxies quench with a slower rate and form a nearly static disc population in the green valley, whereas early-type galaxies quench with very rapid rates, transitioning through the green valley and onto the red sequence in  $\sim 1$  Gyr (Wong et al., 2012).

Although this result of morphologically dependent quenching is intriguing, the work of S14 is hindered for the following reasons: (i) the incompleteness of the galaxy sample; only definitively early- ( $p_s \geq 0.8$ ) and late-type ( $p_s \leq 0.8$ ) galaxies were studied, whereas galaxies of intermediate morphology were excluded, and (ii) the lack of statistics to support the conclusions. Here I use the same toy SFH model but implement STARPY in order to statistically study the star formation histories of galaxies of all morphologies across the colour magnitude diagram.

### 3.1 Defining the Green Valley

To define which of the 126,316 galaxies of the GZ2-GALEX sample are in the green valley, I looked to previous definitions in the literature defining the separation between the red sequence and blue cloud. For example, Baldry et al. (2004) traced this bimodality with a large sample of 66,846 local SDSS galaxies ( $0.004 < z < 0.08$ ) by fitting double-peaked Gaussians to the colour magnitude diagram. Their relation between the  $u - r$  colour,  $C'_{ur}$ , and r-band magnitude,  $M_r$ , to define the colour cut between the blue and red galaxy populations is defined in their Equation 11 as:

$$C'_{ur}(M_r) = 2.06 - 0.244 \tanh\left(\frac{M_r + 20.07}{1.09}\right). \quad (3.1)$$

Due to the necessity for NUV photometry in this study, matching to GALEX removed typical ‘red and dead’ galaxies from the GZ2-GALEX sample. This is apparent in the optical  $u - r$  colour histograms shown in the right panels of Figure 3.1; the GZ2-GALEX sample is split in bins of absolute r-band magnitude and for each bin the position of the green valley at that  $M_r$ , as defined by Baldry et al. (2004) is shown. For the GZ2-GALEX sample at brighter r-band magnitudes (i.e. larger mass), this definition of the green valley seems to intersect with the observed peak at red colours.

However, for a larger SDSS sample (from the MPA-JHU catalog; Kauffmann et al. 2003b; Brinchmann et al. 2004, left panels of Figure 3.1) the Baldry et al. (2004) green valley definition does not intersect with the peak at red colours, as this sample is complete, containing the high mass typical ‘red and dead’ galaxies of the red sequence. It would therefore not be appropriate to define the green valley by a visual fit to the colour magnitude diagram for this study (this method was used in S14 and adopting

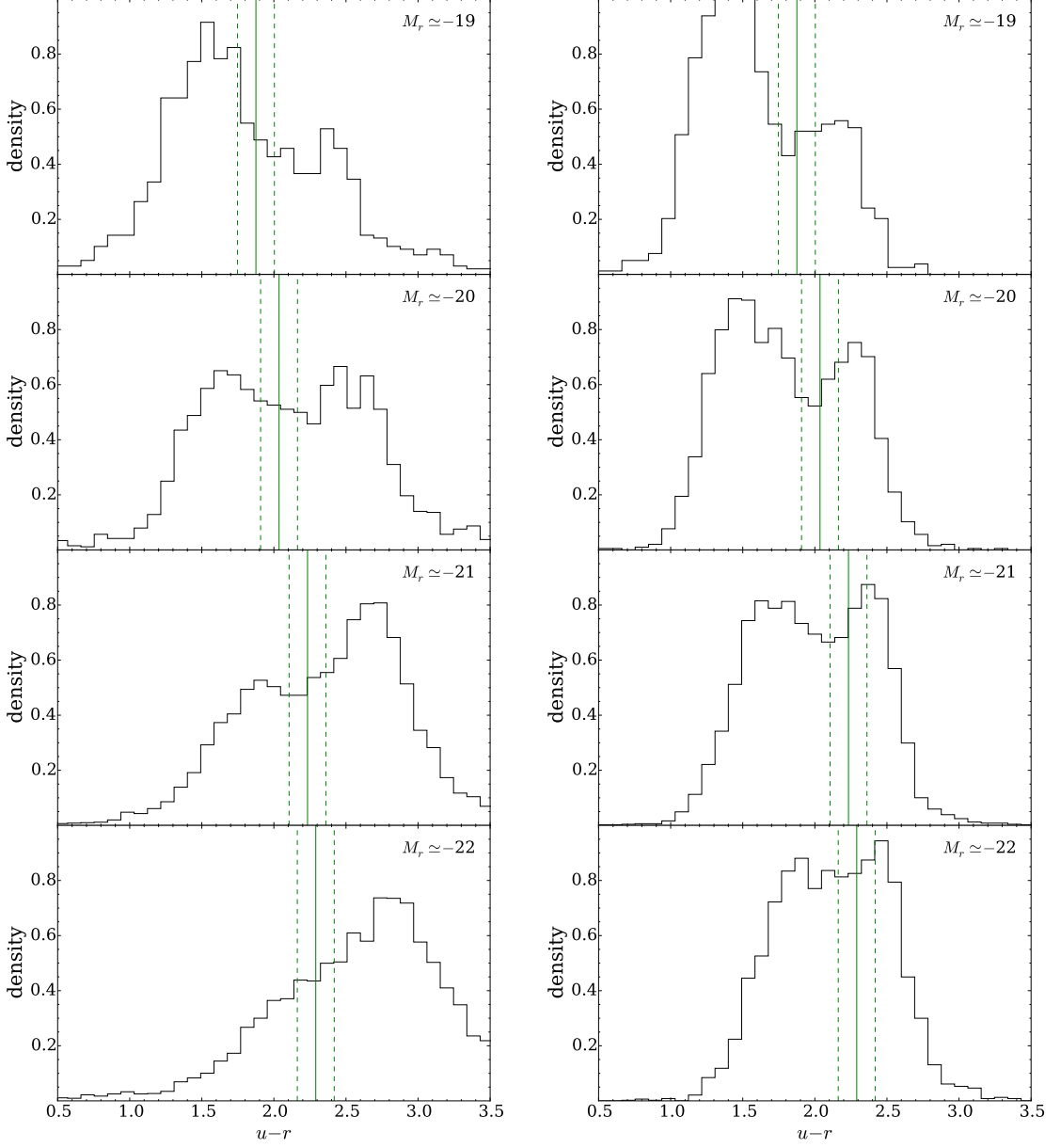


Figure 3.1: Optical  $u - r$  colour histograms, sliced in absolute r-band magnitude for a complete SDSS sample (MPA-JHU catalog; left) and for the GZ2-GALEX sample (right). In each panel the definition between the blue cloud and the red sequence from Baldry et al. (2004) is shown by the dashed line (as defined in Equation 3.1); the solid lines show  $\pm 1\sigma$  either side of this definition.

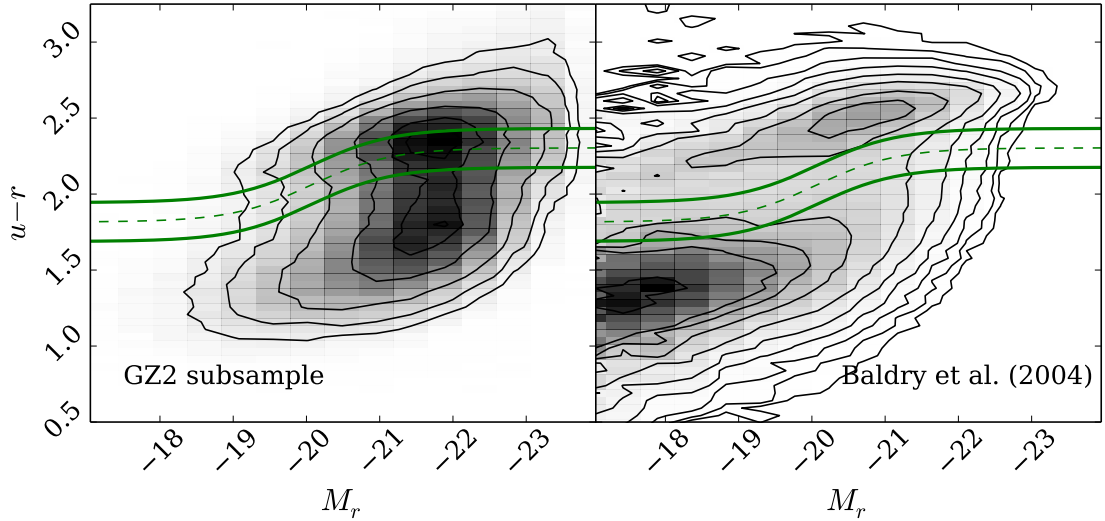


Figure 3.2: Colour-magnitude diagram for the GZ2-GALEX sample (left) and the SDSS sample from Baldry et al. (2004, right). In both panels the definition between the blue cloud and the red sequence from Baldry et al. (2004) is shown by the dashed line, as defined in Equation 3.1. The solid lines show  $\pm 1\sigma$  either side of this definition; any galaxy within the boundary of these two solid lines is considered a green valley galaxy. The lack of red sequence galaxies due to the necessity for NUV GALEX colours skews the apparent location of the green valley in the GZ2-GALEX sample, therefore a literature definition of the green valley is used to ensure galaxies are correctly classified.

it here would have allowed for a direct comparison to this previous work) as this would cause green valley galaxies to be misclassified as red sequence.

I therefore adopt the Baldry et al. (2004) green valley definition for this study, which is shown in Figure 3.2 by the dashed line, in comparison to both the GZ2-GALEX sample (left) and the SDSS data used by Baldry et al. (2004, right). Any galaxy within  $\pm 1\sigma$  of this relationship, shown by the solid lines in Figure 3.2, is therefore considered a green valley galaxy.

Despite the requirement for NUV photometry, the GZ2-GALEX sample still contains typical galaxies from across the entirety of the colour magnitude diagram, including the red sequence. Ko et al. (2013) show that in a sample of quiescent red-sequence galaxies without H $\alpha$  emission (i.e. without spectral indication of recent star formation), 26% show NUV excess emission and that the fraction with recent star

Table 3.1: Table showing the decomposition of the GZ2-GALEX sample by galaxy type into the subsets of the colour-magnitude diagram.

	All	Red Sequence	Green Valley	Blue Cloud
Smooth-like ( $p_s > 0.5$ )	42453 (33.6%)	17424 (61.9%)	10687 (44.6%)	14342 (19.3%)
Disc-like ( $p_d > 0.5$ )	83863 (80.7%)	10722 (38.1%)	13257 (55.4%)	59884 (47.4%)
Early-type ( $p_s \geq 0.8$ )	10517 (8.3%)	5337 (18.9%)	2496 (10.4%)	2684 (3.6%)
Late-type ( $p_s \geq 0.8$ )	51470 (40.9%)	4493 (15.9%)	6817 (28.5%)	40430 (54.4%)
<b>Total</b>	<b>126316</b> (100.0%)	28146 (22.3%)	23944 (18.9%)	74226 (58.7%)

formation is 39%. Therefore this requirement for NUV photometry still allows for the selection of typical red sequence quiescent galaxies. Using the definition of the star forming ‘main sequence’ from Peng et al. (2010, see Section 2.1) I find that 94% of the red sequence galaxies in the GZ2-GALEX sample lie  $1\sigma$  below the main sequence; see Table 3.2).

The decomposition of the GZ2-GALEX sample into red sequence, green valley and blue cloud galaxies is shown in Tables 3.1 and 3.2 along with further division by galaxy type and SFR (where available for the GZ2-GALEX sample from the MPA-JHU catalog) respectively. The tables also list the definitions I adopt henceforth for early-type ( $p_s \geq 0.8$ ), late-type ( $p_d \geq 0.8$ ), smooth-like ( $p_s > 0.5$ ), disc-like ( $p_d > 0.5$ ), quenched ( $\text{SFR} < P - 5\sigma$ ), quenching ( $P - 5\sigma < \text{SFR} < P - \sigma$ ) and star forming ( $\text{SFR} > P - \sigma$ ) galaxies, where  $P$  is the SFR as defined by Peng et al. (2010) for a given stellar mass and observed time (see Equation 2.2).

Figure 3.3 shows the SFR against the stellar mass for the GZ2-GALEX sample (where available from the MPA-JHU catalog) by splitting it into blue cloud, green valley, red sequence, late- and early-type populations. This figure (see bottom row, middle panel) confirms that the green valley galaxies in the GZ2-GALEX sample are indeed a population which have either left, or begun to leave, the star forming ‘main sequence’. A small fraction (20.6%; see Table 3.2) are also classified as star forming

Table 3.2: Table showing the decomposition of the GZ2-GALEX sample by their star formation rate in the subsets of the colour-magnitude diagram.

	All	Red Sequence	Green Valley	Blue Cloud
Quenched (SFR < $P - 5\sigma$ )	24278 (19.7%)	17018 (60.9%)	6440 (27.5%)	820 (1.1%)
Quenching ( $P - 5\sigma < \text{SFR} < P - \sigma$ )	34743 (28.2%)	9277 (33.1%)	12181 (51.9%)	13285 (18.6%)
Star Forming (SFR > $P - \sigma$ )	63957 (52.0%)	1665 (5.9%)	4828 (20.6%)	57464 (80.3%)
<b>Total</b>	<b>122,978</b> (100.0%)	27960 (22.7%)	23449 (19.1%)	71569 (58.2%)

galaxies, however the middle panel, bottom row of Figure 3.3 shows that these galaxies reside on the low SFR side of the ‘main sequence’.

## 3.2 Results

The population density distributions for both smooth and disc weighted populations in the red sample, green valley and blue cloud are shown in Figures 3.4, 3.5 & 3.7 respectively. The full two dimensional distributions in  $[t, \tau]$  are shown in each case, along with a histogram showing the one dimensional projection for each individual parameter. The percentages shown in Figures 3.4, 3.5 & 3.7 are calculated as the fractions of the population densities located in each region of parameter space for a given population.

Since the sample contains such a large number of galaxies, a peak in the population densities will be caused by a large number of galaxies with peaks in their individual posterior distribution at that location in parameter space. This will overwhelm contributions to this area of the population density from galaxies where this region of parameter space is not dominant in their individual posterior distributions. Therefore these fractions can be interpreted as broadly equivalent to the percentage of galaxies in a given population undergoing quenching at a rate within the stated range. Although this is not quantitatively exact, it is nevertheless a useful framework for interpreting the population densities.

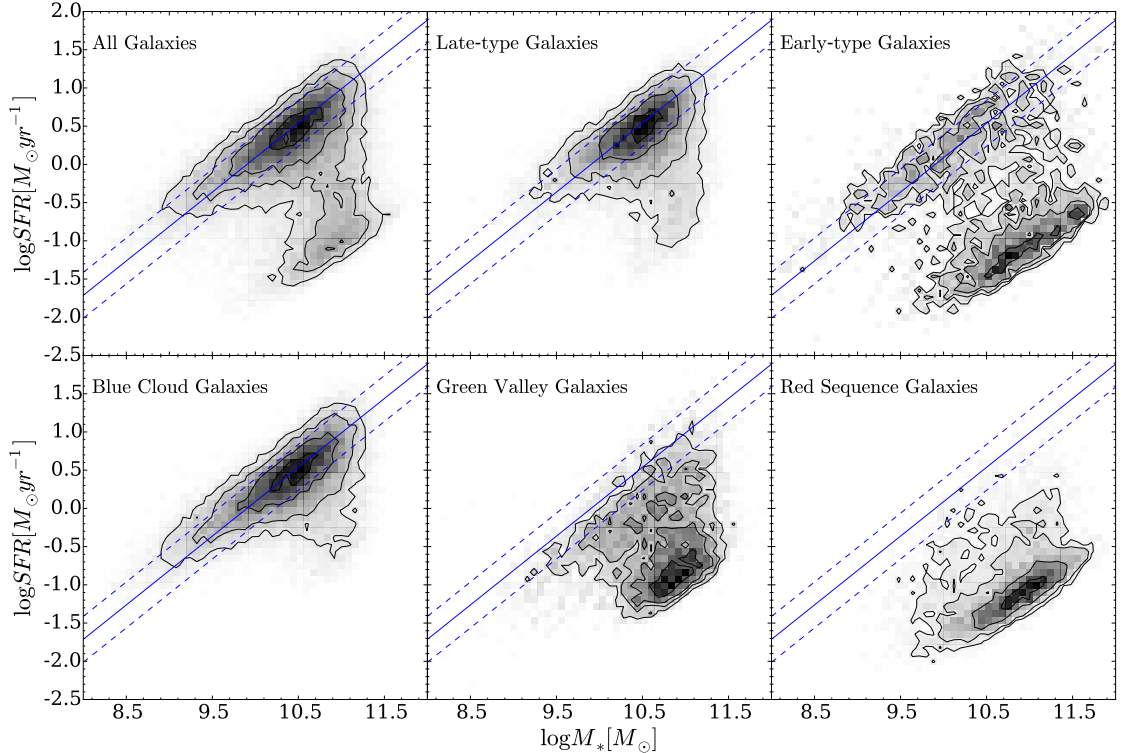


Figure 3.3: Star formation rate against stellar mass for the different populations of galaxies (top row, left to right: all galaxies, late-type galaxies, early-type galaxies; bottom row, left to right: blue cloud, green valley and red sequence galaxies) and how they contribute to the star forming sequence (from Peng et al. (2010), shown by the solid blue line with 0.3 dex scatter by the dashed lines). Based on positions in these diagrams, the green valley does appear to be a transitional population between the blue cloud and the red sequence. Detailed analysis of star formation histories can elucidate the nature of the different populations' pathways through the green valley.

Figure 3.8 shows the distribution of the median walker positions (the 50th percentile of the posterior probability distribution) of each individual galaxy, split into red, green and blue disc-like ( $p_d > 0.5$ ) and smooth-like ( $p_s > 0.5$ ; in order to incorporate the full GZ2-GALEX sample and still investigate the morphological dependance of the results) populations. Unlike in the POPSTARPY method (see Section 2.5) these plots were made without discarding any walker positions due to low probability and without weighting by the GZ2 morphological vote fractions; therefore may be more intuitive to understand than Figures 3.4, 3.5 & 3.7.

Although the quenching rates are continuous in nature, in this Section I will refer to rapid, intermediate and slow quenching rates which correspond to ranges of  $\tau$  [Gyr]  $< 1.0$ ,  $1.0 < \tau$  [Gyr]  $< 2.0$  and  $\tau$  [Gyr]  $> 2.0$  respectively for ease of discussion.

### 3.2.1 The Red Sequence

The top panel of Figure 3.4 reveals that the red smooth weighted population density is dominated (49.5%; see Figure 3.4) by rapid quenching rates across all cosmic time. At early quenching times (high redshift), the population density is dominated by slow and intermediate rates (top panel of Figure 3.4). Perhaps this is the influence of intermediate galaxies (with  $p_s \sim p_d \sim 0.5$ ), hence why similar high density areas exist for both the smooth and disc weighted populations in both panels of Figure 3.4. This is especially apparent considering there are far more of these intermediate galaxies than those that are definitively early- or late-types (see Table 3.1).

The bottom panel of Figure 3.4 reveals a bimodal distribution for the disc weighted population density between rapid (31.3%) and slow (44.1%) quenching rates. The *very* slow ( $\tau > 3.0$  Gyr) quenching rates present in the red disc population density (which are not seen in either the green valley or blue cloud, see Figures 3.5 and 3.7) suggests that these galaxies have only just reached the red sequence after a very slow evolution across the colour-magnitude diagram. Considering their limited number and the requirement for NUV emission, it is likely that these galaxies are currently on the edge of the red sequence having recently (and finally) moved out of the green valley.

Tojeiro et al. (2013) used the VErsatile SPectral Analyses spectral fitting code

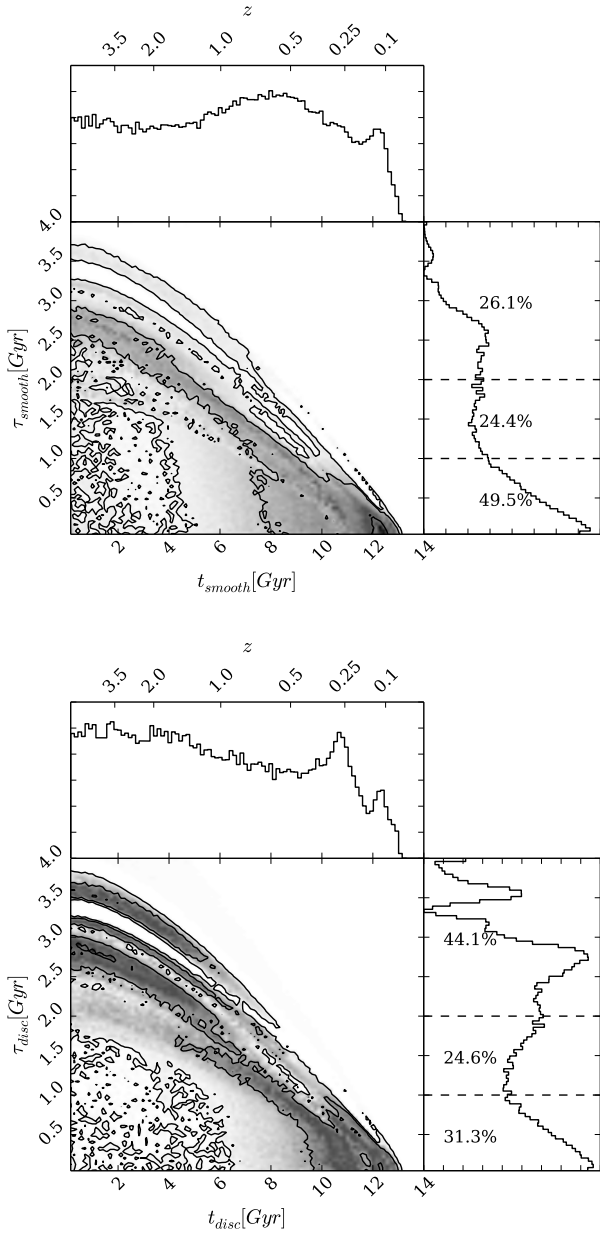


Figure 3.4: Contour plots showing the population densities for red galaxies of the GZ2-GALEX sample, weighted by the morphological vote fractions from GZ2 to give both bulge (top) and disc (bottom) dominated distributions. The histograms show the projection into one dimension for each parameter. The dashed lines show the separation between rapid ( $\tau$  [Gyr]  $<$  1.0), intermediate ( $1.0 < \tau$  [Gyr]  $<$  2.0) and slow ( $\tau$  [Gyr]  $>$  2.0) quenching rates with the fraction of the combined posterior probability distribution in each region shown (see Section 2.2).

(VESPA; Tojeiro et al. 2007) and found that red late-type spirals show 17 times more recent star formation than red elliptical galaxies. The results in Figure 3.4 can be tested against this finding by comparing the SFRs predicted by the inferred SFH model of both the smooth and disc weighted population densities (these SFRs are shown in Figure 2.2). For the peak at early times and slow quenching rates in the red disc weighted population density, this SFH model still has some residual star formation occurring with a  $SFR \sim 0.105 M_{\odot} yr^{-1}$ . Whereas for the peak at recent times and rapid quenching rates in the red smooth weighted population density, this SFH model has a resultant  $SFR \sim 0.0075 M_{\odot} yr^{-1}$ . This is approximately 14 times less than the residual SFR still occurring in the red disc weighted population; within error, this is in agreement with the findings of Tojeiro et al. (2013).

These results for the red sequence galaxies have many implications for green valley galaxies, as all of these systems must have passed through the green valley on their way to the red sequence.

### 3.2.2 Green Valley Galaxies

Figure 3.5 shows how the smooth weighted green valley population density is dominated by both intermediate quenching rates (40.6%) and slow quenching at rates early times ( $z > 1$ ; 40.7%). The fraction of the population density at rapid quenching rates in this smooth weighted population has dropped by over a half compared to the red sequence smooth weighted population. This is caused in part, due to the fact that rapidly quenching galaxies will transition through the green valley very quickly. To quantify this, I tested the time spent in the green valley across the  $[t, \tau]$  parameter space, which is shown in Figure 3.6. The galaxies with such a rapid decline in star formation rate spend very little time in the green valley, therefore less of these galaxies will reside in the green valley at any one time, in comparison to those galaxies transitioning with slower quenching rates. The amount of rapid quenching occurring across the entire galaxy population is not underestimated however, as all galaxies which have undergone a rapid quenching history will now be found in the red sequence. This explains the dominance of rapid quenching rates in the red sequence population densities (see Figure 3.4) and explains the observed number of intermediate morphology galaxies (see Table 3.1) which are present in the green valley (assuming a morphological change occurs during the quench).

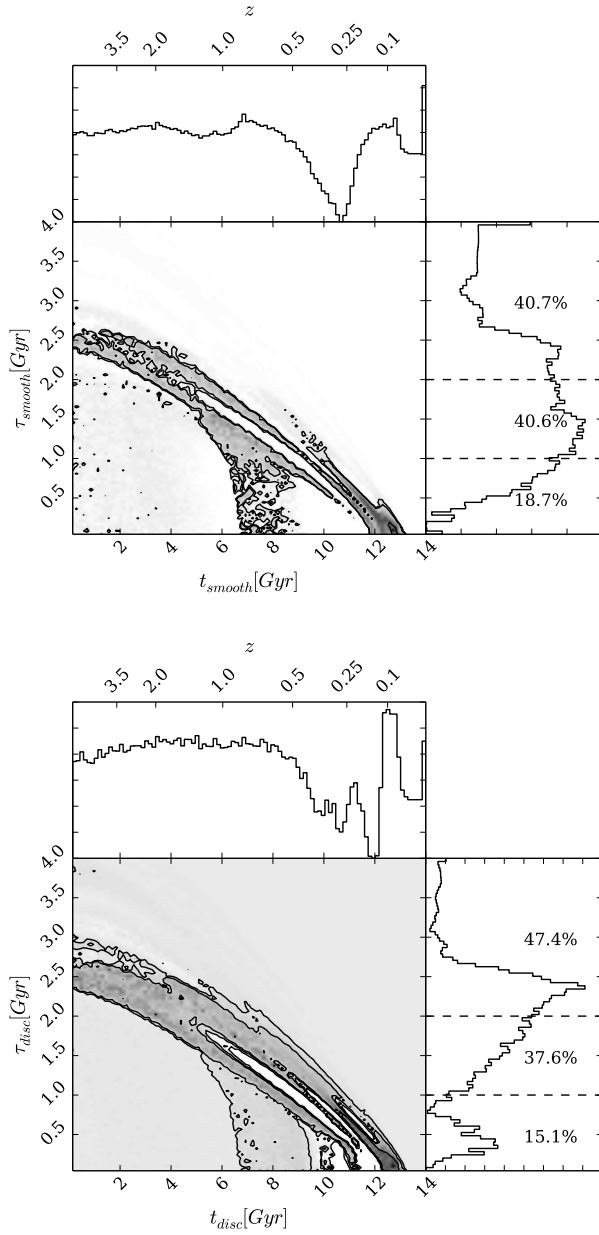


Figure 3.5: Contour plots showing the population densities for green valley galaxies in the GZ2-GALEX sample weighted by the morphological vote fractions from GZ2 to give both bulge (top) and disc (bottom) dominated distributions. The histograms show the projection into one dimension for each parameter. The dashed lines show the separation between rapid ( $\tau$  [Gyr] < 1.0), intermediate (1.0 <  $\tau$  [Gyr] < 2.0) and slow ( $\tau$  [Gyr] > 2.0) quenching rates with the fraction of the combined posterior probability distribution in each region shown (see Section 2.2).

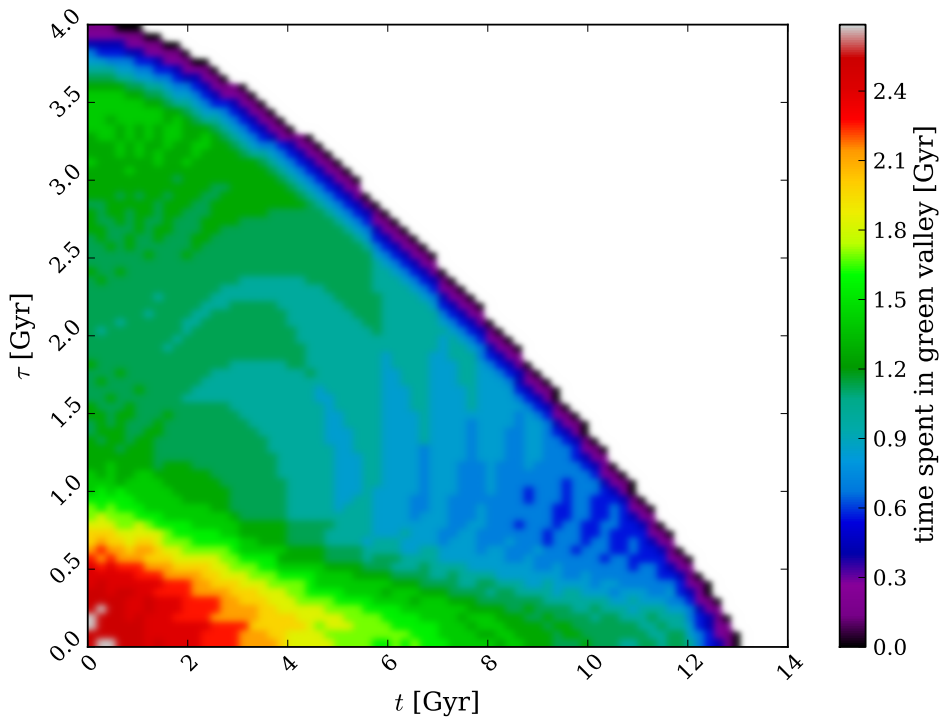


Figure 3.6: Plot showing the time spent in the green valley across the SFH model parameter space by the current epoch. This affects the observability of those galaxies which have quenched rapidly and recently and have passed too quickly through the green valley to be detected. The white region denotes those models with colours that do not enter the green valley by the present cosmic time.

Conversely, the green valley disc weighted population density is now completely dominated by slow quenching rates (47.4%) with a slightly smaller fraction of intermediate quenching rates detected (37.6%; see Figure 3.5).

If the population densities of Figures 3.5 & 3.4 are compared, quenching is detected at later cosmic times (lower redshift) in the green valley than in the red sequence for both morphological types. This therefore suggests that both morphologies are tracing the evolution of the red sequence, confirming that the green valley is indeed a transitional population between blue cloud and red sequence regardless of morphology.

Given enough time ( $t \sim 4 - 5$  Gyr), the current green valley disc galaxies will therefore eventually transition through to the red sequence (the right panel of Figure 2.1 shows galaxies with  $\tau > 1.0$  Gyr do not approach the red sequence within 3 Gyr post quench). This is most likely the origin of the ‘red spirals’, attributed to the *very* slow quenching rates discussed in Section 3.2.1 (and see bottom panel of Figure 3.4). This is in contradiction to the conclusions of S14 who state that the green valley disc population is static in nature.

Considering this result that the green valley is a transitional population, the ratio of smooth : disc galaxies that is currently observed in the green valley is expected to evolve into the ratio observed in the red sequence (assuming that the decreased number of galaxies detected in the red sequence due to matching to GALEX is independent of morphology). Table 3.1 shows the ratio of smooth-like : disc-like galaxies in the red sequence is 62 : 38, whereas in the green valley this ratio is 45 : 55. Making the very simple assumptions that this ratio does not change with redshift and that quenching is the only mechanism which causes a morphological transformation, then 31.2% of the disc-like galaxies in the green valley would have to undergo a morphological change to a smooth-like galaxy.

Inspecting the the disc weighted green valley population density (bottom panel of Figure 3.5) reveals that 29.4% of the distribution occupies the  $\tau < 1.5$  Gyr parameter space. Since this is a similar fraction to the number of green valley disc-like galaxies which would have to undergo a morphological change to a smooth-like galaxy to match the ratio of smooth : disc galaxies in the red sequence, this suggests that quenching mechanisms with  $\tau < 1.5$  Gyr are capable of destroying the disc-dominated structure of galaxies.

All of this evidence suggests that there are not just two contrasting evolutionary pathways through the green valley for different morphological types as concluded by S14. The intermediate quenching rates reside in the space between the extremes sampled by the optical-NUV colour-colour diagrams of S14. The inclusion of the intermediate galaxies in this investigation and the use of a statistical method, elucidates a continuum of quenching rates, with all galaxies transitioning through the green valley to the red sequence during quenching, regardless of morphology.

Therefore instead of concluding that '*the green valley is a red herring*' as in S14, I would conclude that the '*grass is always redder on the other side*'.

### 3.2.3 Blue Cloud Galaxies

Since the blue cloud is considered to be made of star forming galaxies STARPY is expected to have some difficulty inferring any quenching model to describe them, as confirmed by Figure 3.7. The attempt to characterise a star forming galaxy with a quenched SFH model leads STARPY to attribute the extremely blue colours of the majority of these galaxies with a constant SFR until recent times with a fast quench at the observed redshift (i.e. the colour has not had enough time to change from blue post-quench).

This is particularly apparent for the blue disc weighted population. Perhaps even galaxies which are currently quenching slowly across the blue cloud cannot be well fit by the quenching models implemented, as they still have high SFRs despite some quenching. By definition although a galaxy is undergoing quenching, star formation can still be occurring in a galaxy, just at a slower rate than at earlier times, described by  $\tau$ .

A very small fraction of the blue smooth weighted population density is found at slower quenching rates which began prior to  $z \sim 0.5$ . These populations have been blue for a considerable period of time, slowly using up their gas for star formation by the Kennicutt–Schmidt law (Schmidt, 1959; Kennicutt, 1997). However the dominant fraction of the blue smooth weighted population density occurs at rapid quenching rates at recent times. This therefore provides some support to the theories for blue ellipticals as either merger-driven ( $\sim 76\%$ ; like those identified as recently quenched ellipticals with properties consistent with a merger origin by McIntosh et al. 2014) or

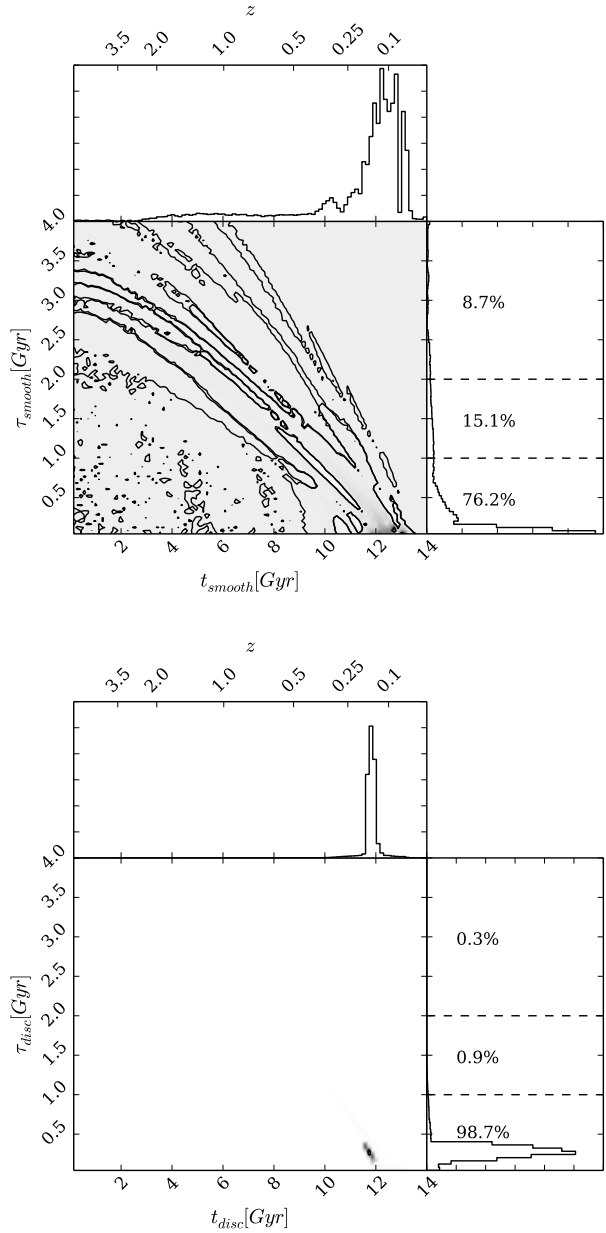


Figure 3.7: Contour plots showing the population densities blue cloud galaxies in the GZ2-GALEX sample, weighted by the morphological vote fractions from GZ2 to give both bulge (top) and disc (bottom) dominated distributions. The histograms show the projection into one dimension for each parameter. The dashed lines show the separation between rapid ( $\tau$  [Gyr]  $<$  1.0), intermediate ( $1.0 < \tau$  [Gyr]  $<$  2.0) and slow ( $\tau$  [Gyr]  $>$  2.0) quenching rates with the fraction of the combined posterior probability distribution in each region shown (see Section 2.2). Positions with probabilities less than 0.2 are discarded as poorly fit models, therefore unsurprisingly blue cloud galaxies are not well described by a quenching star formation model.

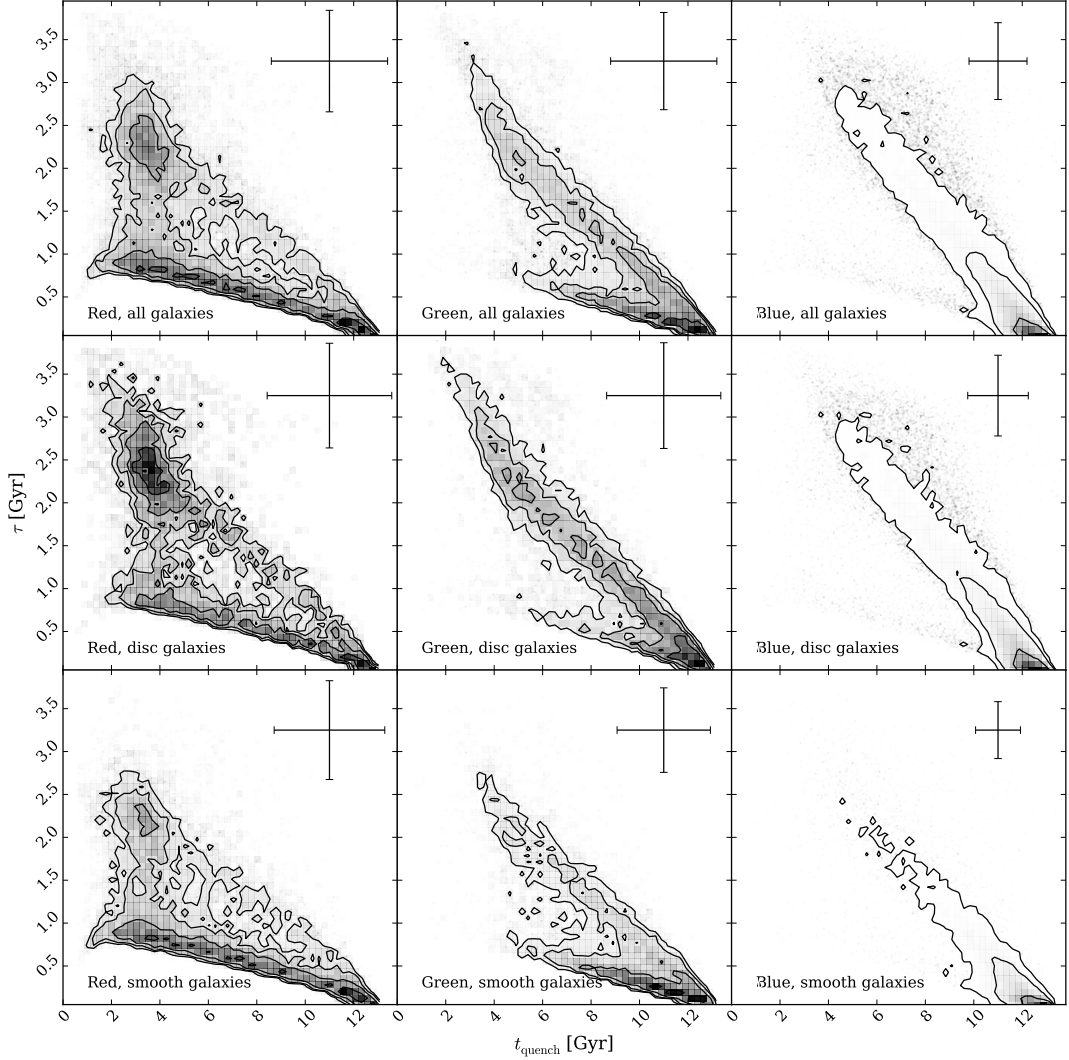


Figure 3.8: Contours showing the positions in the  $[t, \tau]$  parameter space of the median walker position (the 50th percentile; as shown by the intersection of the solid blue lines in Figure 2.2.2) for each galaxy for all (top), disc ( $p_d > 0.5$ ; middle), and smooth ( $p_s > 0.5$ ; bottom) red sequence, green valley and blue cloud galaxies in the left, middle and bottom panels respectively. The error bars on each panel shows the average 68% confidence on the median positions (calculated from the 16th and 84th percentile, as shown by the blue dashed lines in Figure 2.2.2). These positions were calculated without discarding any walker positions due to low probability and without weighting by vote fractions, therefore this plot may be more intuitive than Figures 3.4, 3.5 & 3.7. The differences between the smooth and disc populations and between the red, green and blue populations remain clearly apparent.

Table 3.3: Table summarising the main results in Section 3.2 by describing the distributions derived for each population across the colour-magnitude diagram.

	Red Sequence	Green Valley	Blue Cloud
Smooth-weighted	Dominated by rapid quenching rates	Dominated by intermediate quenching rates	Dominated by rapid quenching rates
Disc-weighted	Bimodal between slow and rapid quenching rates	Dominated by slow quenching rates	-

gas inflow-driven reinvigorated star formation that is now slowly decreasing ( $\sim 24\%$ ; such as the population of blue spheroidal galaxies studied by Kaviraj et al. 2013).

The blue cloud is therefore primarily composed of both star forming galaxies of all morphologies and a smooth population undergoing a rapid quench, presumably after a previous event triggered star formation and turned them blue.

### 3.3 Discussion

In the previous section I presented the results of using POPSTARPY to derive the distribution of quenching histories for galaxies across the colour magnitude diagram. I found differences between the SFHs of smooth- and disc-weighted populations of the red sequence, green valley and blue cloud. These results are summarised in Table 3.3. In this section I will speculate on the following question: what are the possible mechanisms driving these differences?

#### 3.3.1 Rapid Quenching Rates

Rapid quenching is found at larger fractions in the smooth weighted population densities than the disc weighted population (comparing top and bottom panels in Figures 3.4 & 3.5). The red sequence populations also have larger fractions of rapid quenching rates than green valley population densities population (compare Figures 3.4 & 3.5)..

This result suggests that rapid quenching mechanisms can cause a change in morphology from a disc- to a smooth dominated galaxy as it quickly traverses the colour-magnitude diagram to the red sequence. This is supported by the number of disc galaxies that would need to undergo a morphological change in order for the smooth : disc ratio of galaxies in the green valley to match that of the red sequence (see Section 3.2.2). From this indirect evidence I suggest that this observed rapid quenching mechanism is caused by major mergers. However, since a significant fraction of the red disc weighted population density is found at rapid quenching rates (bottom panel Figure 3.4), this suggests that the quenching may have occurred more rapidly than the morphological change in such a merger.

In order to achieve such rapid quenching rates ( $\tau \lesssim 0.5$ ) in a simulation of a major merger, Springel, Di Matteo, & Hernquist (2005) showed that feedback from black hole activity is necessary. As discussed in Section 1, powerful quasar outflows are thought to be able to remove much of the gas from the inner regions of the galaxy, terminating star formation on extremely short rates. Bell et al. (2006), using data from the COMBO-17 redshift survey ( $0.4 < z < 0.8$ ), estimate a merger timescale of  $\sim 0.4$  Gyr for the merger to go from being classified as a close galaxy pair to morphologically disturbed. Springel, Di Matteo, & Hernquist (2005) consequently find using hydrodynamical simulations that after  $\sim 1$  Gyr the merger remnant has reddened to  $u - r \sim 2.0$ .

These simulation results are in agreement with the simple exponential quenching models used here which show (Figure 2.1) that the models with a SFH with  $\tau < 0.4$  Gyr (under the simple assumption that the merger timescale will be  $\sim$  quenching rate) have reached  $u - r \gtrsim 2.2$ , within  $\sim 1$  Gyr. This could explain the fraction of the red disc weighted population with very rapid quenching rates. These galaxies may have undergone a major merger recently but are still undergoing a morphological change from disc, to disturbed, to an eventual smooth galaxy (see also van der Wel et al. 2009). Similarly they may have retained their disc structure in a merger, such as in recent simulations by Pontzen et al. (2016). This possible connection between AGN feedback and rapid quenching rates is explored further in Chapter 4.

These rapid quenching rates, while found across all populations do not fully characterise the entire red sequence or green valley populations. Dry major mergers therefore cannot fully account for the formation of any galaxy population, supporting

the observational conclusions made by Bell et al. (2007); Bundy et al. (2007); Kaviraj (2014b) and simulations by Genel et al. (2008).

### 3.3.2 Intermediate Quenching Rates

Intermediate quenching rates are found to be equally prevalent across both smooth and disc weighted populations across cosmic time and are particularly dominant in the green valley (see Figure 3.5). This suggests that this intermediate quenching rate must therefore be caused by mechanisms that both preserve and transform morphology. It is this result of another route through the green valley that is in contradiction with the findings of S14.

I propose that these intermediate quenching rates ( $1 \leq \tau [\text{Gyr}] \leq 2$ ) are caused by gas rich major mergers, major mergers without black hole feedback, minor mergers and galaxy interactions. This is supported by the findings of Lotz et al. (2011), who find in simulations that increasing the baryonic gas fraction in a merger (mass ratios  $\sim 1 : 1 - 1 : 4$ ) the observability timescale of the merger increases from  $\sim 0.2$  Gyr (with little gas, as above for major mergers which can cause rapid quenching rates) up to  $\sim 1.5$  Gyr (with large gas fractions).

Intermediate quenching rates are equally dominant for both smooth and disc populations across Figures 3.4 and 3.5. Lotz et al. (2008) show that the remnants of simulated equal mass gas rich disc mergers (wet disc mergers) are observable for  $\gtrsim 1$  Gyr post merger and state that they appear “disc-like and dusty” in the simulations, which is consistent with an “early-type spiral morphology”. Such galaxies are often observed to have spiral features with a dominant bulge, suggesting that such galaxies may divide the votes of the GZ2 users, producing vote fractions of  $p_s \sim p_d \sim 0.5$ . Such a vote fraction may also arise because the galaxy is at a large distance or because it is an S0 galaxy whose morphology can be interpreted by different GZ2 users in different ways. Willett et al. (2013) find that S0 galaxies expertly classified by Nair & Abraham (2010) are more commonly classified as ellipticals by GZ2 users, but have a significant tail to high disc vote fractions. A galaxy with these ambiguous GZ2 vote fractions will therefore contribute equally to the smooth and disc weighted population densities which may explain the dominance of these intermediate quenching rates across all populations.

By inspecting Figure 2.2, we find that SFH models with these intermediate quenching rates of  $1.0 \lesssim \tau$  [Gyr]  $\lesssim 2.0$  take approximately  $2.5 - 5.5$  Gyr to reach the red sequence. In the simulations of Springel, Di Matteo, & Hernquist (2005), which do not include feedback from black holes, merger remnants can sustain low levels of star formation for several Gyrs if even a small fraction of gas is not consumed in the merger triggered starburst (either because the mass ratio is not large enough or from the lack of strong black hole activity). The remnants from these simulations take  $\sim 5.5$  Gyr to reach red optical colours of  $u - r \sim 2.1$ , providing support for the hypothesis that the intermediate quenching rates may be caused by minor mergers.

Observationally, Darg et al. (2010) showed an increase in the spiral to elliptical ratio for merging galaxies ( $0.005 < z < 0.1$ ) by a factor of two compared to the typical galaxy population. They attribute this to the mergers of spirals being observable for much longer compared to mergers with elliptical galaxies. This supports the hypothesis that the slower quenching rates in the  $\tau < 1.5$  Gyr region of the disc weighted green valley population density (see bottom panel of Figure 3.5) may be caused by a minor or wet major merger and eventually give rise to the morphological change needed to match the ratio of smooth:disc galaxies seen in the red sequence (see Section 3.2.2).

Darg et al. (2010) also show (in their Figure 6) that less than a merger ratio of  $1 : 10$  (up to  $\sim 1 : 100$ ), green is the dominant average galaxy colour of visually identified merging pairs in GZ. These pairs are also dominated by spiral-spiral mergers as opposed to elliptical-elliptical and elliptical-spiral mergers. The remnants of these green spiral-spiral mergers would contribute to the green disc weighted population density in the bottom panel of Figure 3.5, where these intermediate quenching rates are found to be the dominant SFH. This lends more support to the idea that these intermediate quenching rates are caused in part by minor mergers.

For the smooth weighted green valley population (shown in the top panel of Figure 3.5), 40.6% of the distribution is found in the intermediate quenching rate regime. Similarly, Kaviraj (2014b,a) by studying SDSS photometry ( $z < 0.07$ ) state that approximately half of the star formation in all galaxies is driven by minor mergers at  $0.5 < z < 0.7$ . These minor mergers would therefore exhaust available gas for star formation and consequently causing a gradual decline in the star formation rate. This is therefore complimentary to the fraction of smooth green valley galaxies found to be undergoing intermediate quenching rates in the top panel of Figure 3.5.

Assuming that rapid and intermediate quenching rates are therefore caused by major or minor mergers, the fraction of population density with  $\tau \leq 2$  Gyr can provide an estimate for the percentage of galaxies with a merger dominated evolutionary history. This is calculated to be 73.9% and 59.3%, for the smooth weighted red sequence and green valley populations (top panels Figures 3.4 and 3.5) respectively. This estimate for the fraction of smooth galaxies with merger dominated histories is supported by the earlier work of Kaviraj et al. (2011). They use multi wavelength photometry of galaxies in COSMOS (Scoville et al., 2007), to estimate that 70% of early-type galaxies appear morphologically disturbed, suggesting either a minor or major merger in their history. Note that the star formation model used here is a basic one and has no prescription for reignition of star formation post-quench which can also cause morphological disturbance of a galaxy, like those detected by Kaviraj et al. (2011) and seen in simulations by Pontzen et al. (2016).

Any external event which can cause either a burst of star formation (depleting the gas available) or directly strip a galaxy of its gas, for example galaxy harassment, interactions, ram pressure stripping, strangulation and interactions internal to clusters, should also cause quenching with an intermediate rate. Such mechanisms would be the dominant cause of quenching in dense environments; considering that the majority of galaxies reside in groups or clusters (Coil et al. 2008 find that green valley galaxies are just as clustered as red sequence galaxies). It is not surprising therefore that the majority of the GZ2-GALEX galaxies ( $\sim 50\%$ ) are considered intermediate in morphology (i.e.,  $p_d \sim p_s \sim 0.5$ , see Table 3.1) and therefore may be undergoing or have undergone such an interaction. This obvious dependency of the quenching parameters with the galaxy environment will be investigated further in Chapter 5.

### 3.3.3 Slow Quenching Rates

Although intermediate and rapid quenching rates are the dominant mechanisms across the colour-magnitude diagram, together they cannot completely account for the quenching of disc galaxies. S14 concluded that slow quenching rates were the most dominant mechanism for disc galaxies. However I show that: (i) intermediate quenching rates are equally important in the green valley (bottom panel Figure 3.5) and (ii) rapid quenching rates are equally important in the red sequence (bottom panel Figure 3.4). There is also a significantly lower fraction in the smooth weighted

population densities for slow quenching rates (top panels of Figures 3.4 & 3.5); suggesting that the evolution (or indeed creation) of typical smooth galaxies is dominated by processes external to the galaxy. The exceptions are galaxies in the blue cloud where a small fraction of the smooth weighted population density is found at slow quenching rates (top panel Figure 3.7), which could be due to a reinvigoration of star formation which is slowly depleting the gas available (via the Kennicutt–Schmidt law).

Table 3.1 shows that 3.9% of the GZ2-GALEX sample are red sequence late-type galaxies, i.e. red late-type spirals. This is, within uncertainties, in agreement with the findings of Masters et al. (2010a), who find  $\sim 6\%$  of late-type spirals are red when defined by a cut in the  $g - r$  optical colour (rather than with  $u - r$  as used in this investigation) and are at the ‘blue end of the red sequence’. Bamford et al. (2009) using GZ1 vote fractions of galaxies in the SDSS, found a significant fraction of field galaxies are in fact high stellar mass red spiral galaxies. As these galaxies are isolated from the effects of interactions from other galaxies, the slow quenching mechanisms dominant in the disc weighted population densities (bottom panels of Figures 3.4 & 3.5) are most likely due to secular processes (i.e. mechanisms internal to the galaxy, in the absence of sudden accretion or merger events; Kormendy & Kennicutt 2004; Sheth et al. 2012). Bar formation in a disc galaxy is such a mechanism, whereby gas is funnelled to the centre of the galaxy by the bar over long rates where it is used for star formation (Masters et al., 2012; Saintonge et al., 2012; Cheung et al., 2013), consequently forming a ‘pseudo-bulge’ (Kormendy et al., 2010; Simmons et al., 2013).

If these slow quenching rates are due to secular evolution processes, this is to be expected since these processes do not change the disc dominated nature of a galaxy.

## 3.4 Conclusions

I have used morphological classifications from the Galaxy Zoo 2 project to determine the morphology-dependent star formation histories of galaxies via a Bayesian analysis of an exponentially declining star formation quenching model. The most likely parameters were determined for the quenching onset time,  $t_q$  and quenching timescale  $\tau$  in this model for galaxies across the blue cloud, green valley and red sequence to

trace the morphological dependance of galactic evolution across the colour-magnitude diagram.

The green valley is found to be a transitional population for all morphological types (in conflict with S14), however this transition proceeds slowly for the majority of disc dominated galaxies and occurs rapidly for the majority of smooth dominated galaxies in the red sequence (in agreement with S14). However, in addition to the results of S14, the inclusion of both (i) the entire GZ2-GALEX sample with no morphology thresholds, and (ii) a robust statistical analysis of the results has revealed a more nuanced result; specifically that the prevailing mechanism across all morphologies and populations is quenching with intermediate rates. The main findings are summarised as follows:

- (i) Quenching within the red sequence population occurs at earlier quenching times (i.e. higher redshift) than in the green valley population regardless of morphology (see Figures 3.4 and 3.5). Therefore the quenching mechanisms currently occurring in the green valley were also active in creating the ‘blue end of the red sequence’ at earlier times; confirming that the green valley is indeed a transitional population, regardless of morphology.
- (ii) The red sequence is dominated by galaxies which are elliptical in morphology and have undergone a rapid to intermediate quench at some point in cosmic time, resulting in a very low current SFR (see Section 3.2.1).
- (iii) The green valley as it is currently observed is dominated by very slowly evolving disc dominated galaxies along with intermediate- and smooth dominated galaxies which pass across it with intermediate rates within  $\sim 1.0 - 1.5$  Gyr (see Section 3.2.2).
- (iv) There are many different mechanisms responsible for quenching, all causing a galaxy to progress through the green valley. These mechanisms are dependant on galaxy type, with the smooth and disc dominated galaxies each having different dominant star formation histories across the colour-magnitude diagram.
- (v) Blue cloud galaxies are not well fit by a quenching model of star formation due to the continuous high star formation rates occurring (see Figure 3.7).
- (vi) Rapid quenching rates are found at a lower fraction in the green valley population than the red sequence population (see Figures 3.4 & 3.5). I speculate that

this quenching mechanism is caused by major mergers with black hole feedback, which are able to expel the remaining gas not initially exhausted in the merger-induced starburst and which can cause a change in morphology from disc- to bulge-dominated. The colour-change rates from previous simulations of such events agree with the derived quenching rates (see Section 3.3.1). These rapid quenching rates are instrumental in forming red galaxies, however galaxies at the current epoch passing through the green valley do so at more intermediate quenching rates (see Figure 3.5).

- (vii) Intermediate quenching rates ( $1.0 < \tau [\text{Gyr}] < 2.0$ ) are found with constant density across red and green galaxies for both smooth- and disc-weighted populations, the rates for which agree with observed and simulated minor merger rates (see Section 3.3.2). I hypothesise that such rates can also be caused by a number of external processes, including gas rich major mergers, mergers without black hole feedback, galaxy harassment, interactions and ram pressure stripping. The rates and observed morphologies from previous studies agree with the results, including that this is the dominant mechanism for intermediate morphology galaxies such as early-type spiral galaxies with spiral features but a dominant bulge, which split the GZ2 vote fractions (see Section 3.3.2).
- (viii) Slow quenching rates are the most dominant mechanism in the disc galaxy population across the colour-magnitude diagram population (see bottom panels Figures 3.4 & 3.5). Disc galaxies are often found in the field, therefore I hypothesise that such slow quenching rates are caused by secular evolution and processes internal to the galaxy (see Section 3.2.3). A small amount of slow quenching rates is also detected for blue elliptical galaxies which is attributed to a reinvigoration of star formation, the peak of which has passed and has started to decline by slowly depleting the gas available (see Section 3.2.3).

# Chapter 4

## Black hole-galaxy co-evolution in the context of quenching

The following chapter is split into two parts; in Section 4 I investigate the connection between quenching parameters and the presence of an AGN and in Section 4.2 investigate how black holes grow in disc galaxies with merger free evolutionary histories.

### 4.1 Rapid, recent quenching within a population of Type 2 AGN host galaxies

*The work in the following chapter has been published in Smethurst et al. (2016).*

In Chapter 3, rapid quenching rates were dominant across the smooth weighted population densities in Figures 3.5 & 3.4. In Section 3.3.1 I discussed how simulations suggest that such rapid quenching rates can only be achieved if AGN feedback is present in a major merger scenario. I therefore decided to investigate this possible connection between AGN feedback and rapid quenching rates further. I shall do so by analysing the SFHs of a population of AGN host galaxies with POPSTARPY in comparison to an inactive galaxy control sample. I aim to determine the following: (i) Are galaxies currently hosting an AGN undergoing quenching? (ii) If so, when and at what rate does this quenching occur? (iii) Is this quenching occurring at different times and rates compared to a control sample of inactive galaxies? This builds on

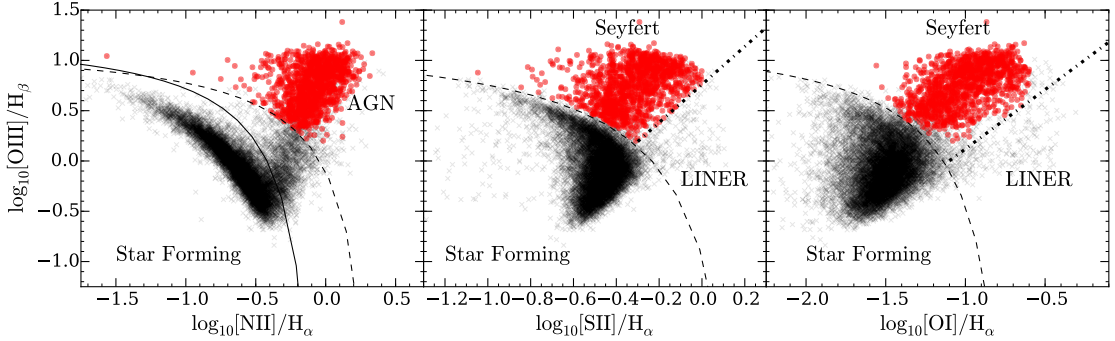


Figure 4.1: BPT diagrams for galaxies in the GZ2-GALEX sample (black crosses) with  $S/N > 3$  for each emission line. Inequalities defined in: Kewley et al. (2001) to separate SF galaxies from AGN (dashed lines), Kauffmann et al. (2003a) to separate SF from composite SF-AGN galaxies (solid line) and Kewley et al. (2006) to separate LINERS and Seyferts (dotted lines). Galaxies are included in the AGN-HOST sample (red circles) if they satisfy all the inequalities to be classified as Seyferts. LINERS are excluded for purity.

the work of Martin et al. (2007) but improves significantly on previous techniques.

#### 4.1.1 AGN Sample

Type 2 AGN were selected from the GZ2-GALEX sample using a BPT diagram (Baldwin et al., 1981) using line and continuum strengths for [OIII], [NII], [SII] and [OII] obtained from the MPA-JHU catalogue (Kauffmann et al., 2003b; Brinchmann et al., 2004). A BPT diagram uses emission line ratio diagnostics to determine whether a galaxy is a star forming galaxy, a Seyfert (i.e. hosting an AGN) or a LINER. The signal-to-noise ratio was required to be  $S/N > 3$  for each emission line as in Schawinski et al. (2010). Those galaxies which satisfied all of the inequalities defined in Kewley et al. (2001, to separate SF galaxies from AGN) and Kauffmann et al. (2003a, to separate SF galaxies from composite SF-AGN galaxies) were selected as Type 2 AGN, giving 1,299 host galaxies ( $\sim 10\%$  of the GZ2-GALEX sample; in agreement with estimates of the local AGN fraction of Kauffmann et al. 2004; Pimbblet et al. 2013).

Sarzi et al. (2010); Yan & Blanton (2012) and Singh et al. (2013) have all demonstrated that LINERS are not primarily powered by AGN, therefore for purity, these

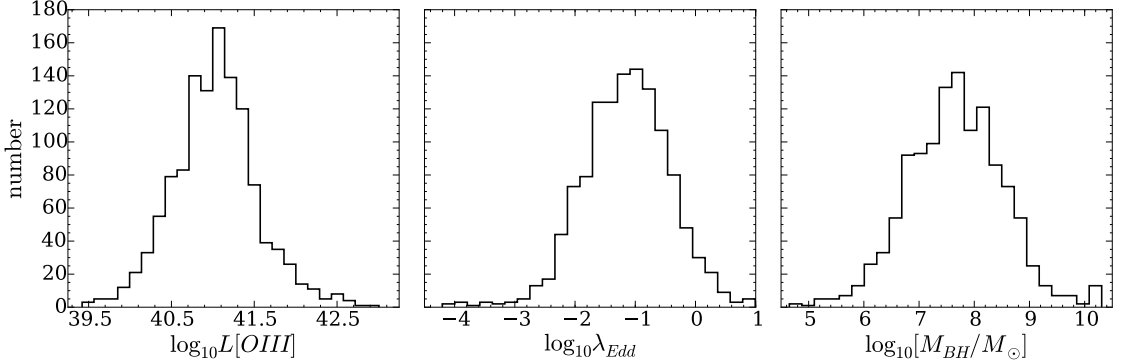


Figure 4.2: Distribution of the [OIII] luminosity (left), Eddington ratio (middle) and black hole masses (right) in the AGN-HOST sample.

galaxies were excluded from the sample using the definition from (Kewley et al., 2006, 55 galaxies total) with no change to the results. These 1,244 galaxies will be referred to as the AGN-HOST sample; Figure 4.1 shows the entire AGN-HOST and GZ2-GALEX samples with the selection criteria used on a BPT diagram.

I do not use Type 1 AGN in this instance due to concerns about contamination of the observed galaxy colours, used in the SFH analysis, from potentially strong NUV emission by unobscured active nuclei. The obscuration of Type 2 AGN is highly efficient, considerably more so in the NUV than the optical (Simmons et al., 2011). Residual NUV flux from a Type 2 AGN can therefore be neglected in comparison to that of the galaxy. However, I did investigate the possibility of contamination of optical galaxy colours from unobscured AGN emission and found that subtracting measured nuclear magnitudes (SDSS `psfMag`) from the total galaxy magnitude (SDSS `modelMag`) produces a negligible change in host galaxy colour ( $\Delta(u-r) \sim 0.09$ ). I therefore use the total galaxy magnitudes (with extinction corrections as described in Section 1.1.1) to avoid unnecessary complexity and minimise the propagation of uncertainty from the observed colours through to the inferred SFHs. However, I note that including these corrected colours does not change the results.

Since this investigation is focussed on whether an AGN can have an impact on the SF of its host galaxy, possible selection effects must be considered. The extent to which SF could obscure AGN emission was addressed by Schawinski et al. (2010). They showed, via analysis of simulated AGN emission added to star-forming galaxies, that BPT-based selection of AGN produces a complete sample at luminosities of

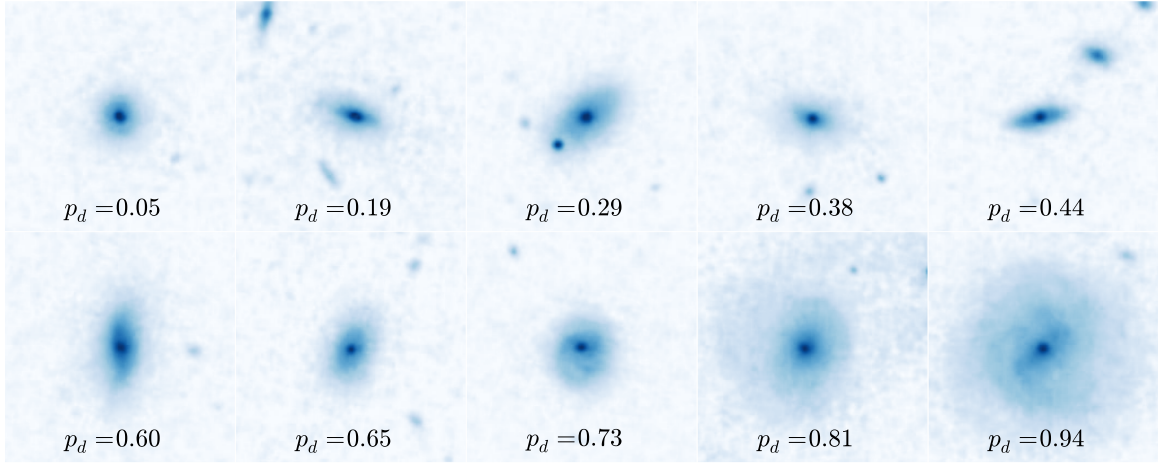


Figure 4.3: Randomly selected SDSS *gri* composite images from the sample of 1,244 Type 2 AGN in a redshift range  $0.04 < z < 0.05$ . The galaxies are ordered from least to most featured according to their debiased ‘disc or featured’ vote fraction,  $p_d$  (see Willett et al. 2013). The scale for each image is 0.099 arcsec/pixel.

$L[OIII] > 10^{40}$  erg s $^{-1}$ . Above this limit I therefore assume I have selected a complete sample of AGN independent of host galaxy SFR.

Black hole masses of the AGN-HOST sample are derived from the  $M_{BH} - \sigma$  relationship defined in McConnell et al. (2011):

$$\log_{10} \left( \frac{M_{BH}}{M_\odot} \right) = 8.29 + 5.12 \log_{10} \left( \frac{\sigma}{200 \text{ km s}^{-1}} \right). \quad (4.1)$$

where the velocity dispersion,  $\sigma$ , is measured from the Balmer lines and is provided in the MPA-JHU catalog (Kauffmann et al., 2003b; Brinchmann et al., 2004). The Eddington ratio,  $\lambda_{Edd}$ , describes the accretion rate of the black hole and is calculated with the proxy  $\lambda_{Edd} = L_{bol}/L_{Edd}$ , where  $L_{Edd}$  is the Eddington luminosity and  $L_{bol}$  is the bolometric luminosity. For obscured (Type 2) AGN the bolometric luminosity cannot be directly measured and so is inferred from the luminosity of the [OIII] emission line, as derived by Heckman et al. (2004):

$$\log_{10} L_{bol} = 3.54 + \log_{10} L[OIII]. \quad (4.2)$$

The Eddington luminosity,  $L_{Edd}$ , is derived from the black hole mass,  $M_{BH}$ , as outlined in Binney & Merrifield (1998) as:

$$L_{Edd} = 3 \times 10^4 \left( \frac{M_{BH}}{M_\odot} \right) L_\odot. \quad (4.3)$$

Table 4.1: Table showing the decomposition of the AGN-HOST sample by galaxy type into the subsets of the colour-magnitude diagram.

	All	Red Sequence	Green Valley	Blue Cloud
Smooth-like ( $p_s > 0.5$ )	340 (27.3%)	21 (25.0%)	105 (41.2%)	213 (23.5%)
Disc-like ( $p_d > 0.5$ )	871 (70.0%)	63 (75.0%)	148 (58.0%)	660 (72.9%)
Early-type ( $p_s \geq 0.8$ )	66 (5.3%)	1 (1.2%)	14 (5.5%)	51 (5.6%)
Late-type ( $p_s \geq 0.8$ )	569 (45.7%)	39 (46.4%)	74 (29.0%)	456 (50.4%)
<b>Total</b>	<b>1244</b> (100.0%)	84 (6.7%)	255 (20.5%)	905 (72.7%)

The distributions of L[OIII],  $M_{BH}$  and  $\lambda_{Edd}$  of the AGN-HOST sample are shown in Figure 4.2. SDSS images for 10 randomly selected galaxies from the AGN-HOST sample are shown in Figure 4.3. The decomposition of the AGN-HOST sample into red sequence, green valley and blue cloud galaxies is shown in Tables 4.1 and 4.2 along with further division by galaxy type and SFR (where available for the AGN-HOST sample from the MPA-JHU catalog) respectively.

### 4.1.2 Defining a control sample

A control sample of inactive galaxies was constructed by removing from the GZ2-GALEX sample all galaxies with line strengths indicative of potential AGN activity (Kauffmann et al., 2003a), as well as sources identified as Type 1 AGN by the presence of broad emission lines (Oh et al., 2015). I selected a mass- and morphology-matched inactive sample by identifying between 1 and 5 inactive galaxies for each AGN-HOST galaxy with the same stellar mass (to within  $\pm 5\%$ ) and GZ2 ‘smooth’ and ‘disc’ vote fractions (to within  $\pm 0.1$ ) giving 6107 galaxies. This sample will be referred to as the INACTIVE sample.

Figure 4.4 shows the GZ2 disc vote fraction ( $p_d$ ; left) and stellar mass ( $M_*$ ; right) distributions of the AGN-HOST sample in comparison to the matched INACTIVE sam-

Table 4.2: Table showing the decomposition of the AGN-HOST sample galaxies by their star formation rate in the subsets of the colour-magnitude diagram.

	All	Red Sequence	Green Valley	Blue Cloud
Quenched	14	9	4	1
(SFR < $P - 5\sigma$ )	(1.3%)	(12.5%)	(1.7%)	(0.1%)
Quenching ( $P - 5\sigma < \text{SFR} < P - \sigma$ )	335 (30.6%)	45 (64.3%)	139 (59.9%)	151 (19.1%)
Star Forming	744	16	89	639
(SFR > $P - \sigma$ )	(68.0%)	(22.9%)	(38.4%)	(80.7%)
<b>Total</b>	<b>1093</b> (100.0%)	70 (6.4%)	232 (21.2%)	791 (72.4%)

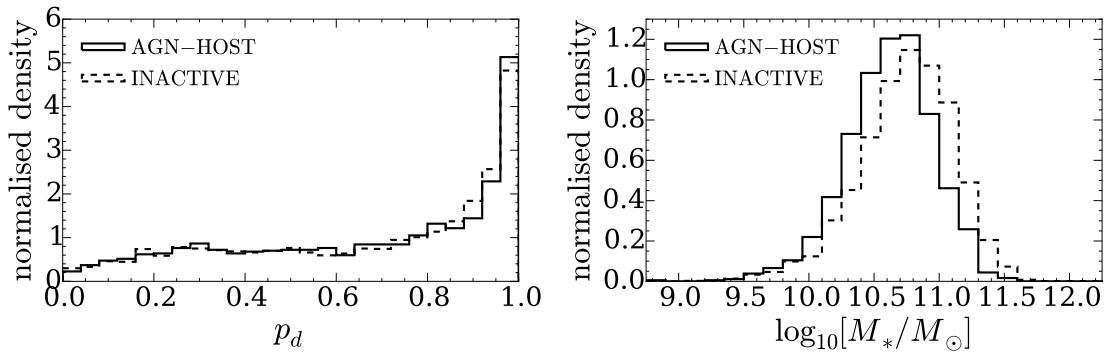


Figure 4.4: Distribution of the GZ2 disc vote fractions ( $p_d$ ; left) and stellar masses (right) in the AGN-HOST sample (solid lines) in comparison to the matched control INACTIVE sample (dashed lines).

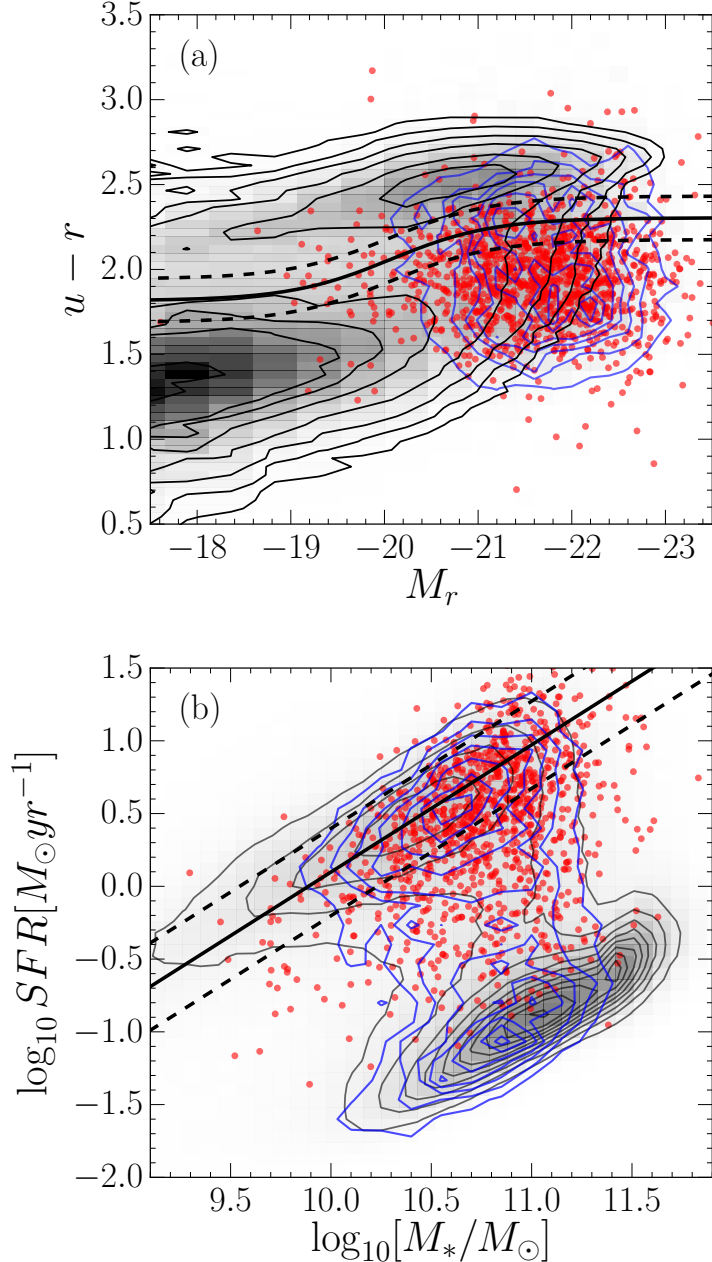


Figure 4.5: (a) Optical colour-magnitude diagram showing the SDSS DR7 (grey filled contours), the AGN-HOST sample (red circles) and INACTIVE sample (blue contours). The definition of the green valley from Baldry et al. (2006) (solid line) with  $\pm 1\sigma$  (dashed lines) is shown. (b) SFR-stellar mass diagram showing the MPA-JHU measurements of SFR and  $M_*$  of SDSS DR7 galaxies (Kauffmann et al. 2003b; Brinchmann et al. 2004; black contours), the AGN-HOST sample (red circles) and INACTIVE sample (blue contours). The star forming ‘main sequence’ from Peng et al. (2010) is shown by the solid line for  $t = 12.8$  Gyr, the average observed age of the GZ2-GALEX sample, with  $\pm 1\sigma$  (dashed lines).

ple. A Kolmogorov-Smirnov test revealed the redshift distributions of the INACTIVE and AGN-HOST samples are statistically indistinguishable ( $D \sim 0.16$ ,  $p \sim 0.88$ ).

The AGN-HOST and INACTIVE samples are also shown on both an optical colour-magnitude diagram and in the SFR-stellar mass plane in Figure 4.5 in comparison to the distribution of SDSS DR7 galaxies. SFRs and stellar masses are obtained from the MPA JHU catalog, where available, which follow the prescriptions outlined in Brinchmann et al. (2004) and Salim et al. (2007) for calculating the total aperture corrected galaxy SFR in the presence of an AGN.

The majority of the AGN-HOST sample would be defined as residing in the blue cloud ( $\sim 73\%$ ) on the optical colour-magnitude diagram despite the fact that a significant proportion of the sample (32%) lie more than  $1\sigma$  (0.3 dex) below the star forming ‘main sequence’ (Peng et al., 2010, see Figure 4.5 and Table 4.2).

### 4.1.3 Results

In Figure 4.6 the AGN-HOST smooth and disc weighted populations are split across three Eddington ratio,  $\lambda_{Edd}$ , bins to investigate any trends with the accretion rate of the black hole in the population densities for the quenching time and rate. The Eddington ratio boundaries were chosen to give equal numbers of AGN-HOST galaxies in each bin.

In Figures 4.7 & 4.8 the AGN-HOST and INACTIVE smooth and disc weighted populations are split across three mass bins to investigate any trends with mass in the population densities for the quenching time and rate respectively. The mass boundaries were chosen to give roughly equal numbers of inactive galaxies in each bin, before mass matching to the AGN-HOST sample. This decision was made to ensure the mass bins were representative of ‘typical’ galaxies rather than being biased by the mass distribution of the agn-host sample which tend to occupy higher mass galaxies.

No cut on the star formation rate is made to the galaxies which contribute to Figures 4.6-4.8, but those galaxies poorly fit by an exponentially declining SFH are down-weighted so that they do not contribute to the results presented here (see Section 2.5 for a description of the POPSTARPY method). Table 4.3 contains the percentages of the population densities shown in Figures 4.7 & 4.8 in the quenching regimes originally defined in Chapter 3 for rapid ( $\tau < 1$  Gyr), intermediate ( $1 < \tau$  [Gyr]  $< 2$ )

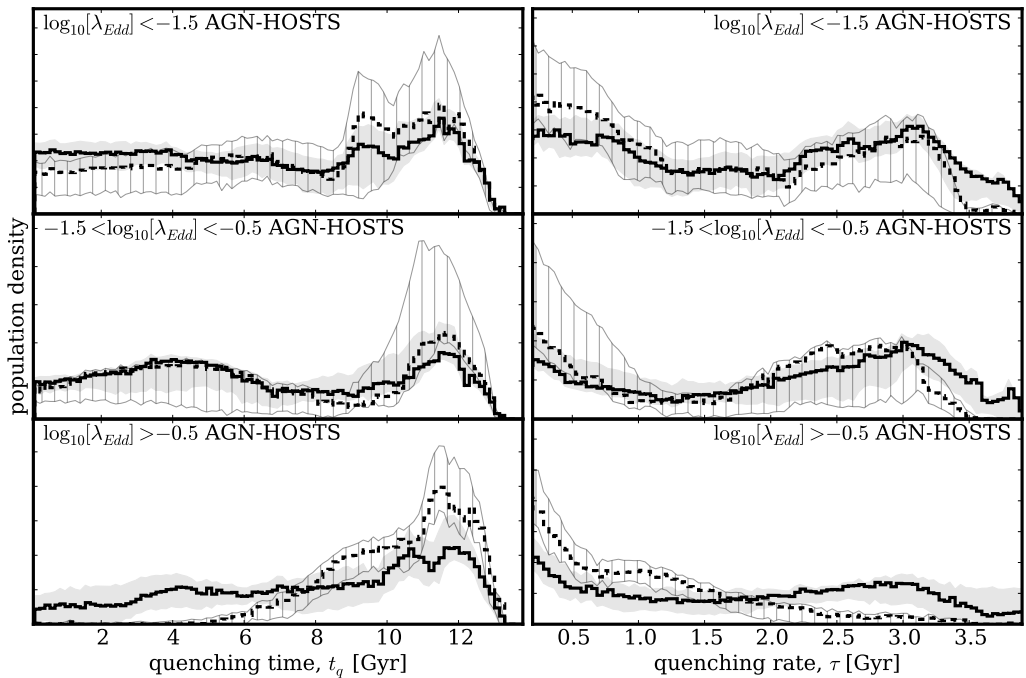


Figure 4.6: Population density distributions for the quenching time ( $t_q$ ; left) and rate ( $\tau$ ; right), normalised so that the areas under the curves are equal. The AGN-HOST sample is split into low (top), medium (middle) and high (bottom) Eddington ratio,  $\lambda_{Edd}$ , for smooth (dashed) and disc (solid) galaxies. Uncertainties from bootstrapping are shown by the shaded regions for the smooth (grey striped) and disc (grey solid) population densities. A small (large) value of  $\tau$  corresponds to a rapid (slow) quench.

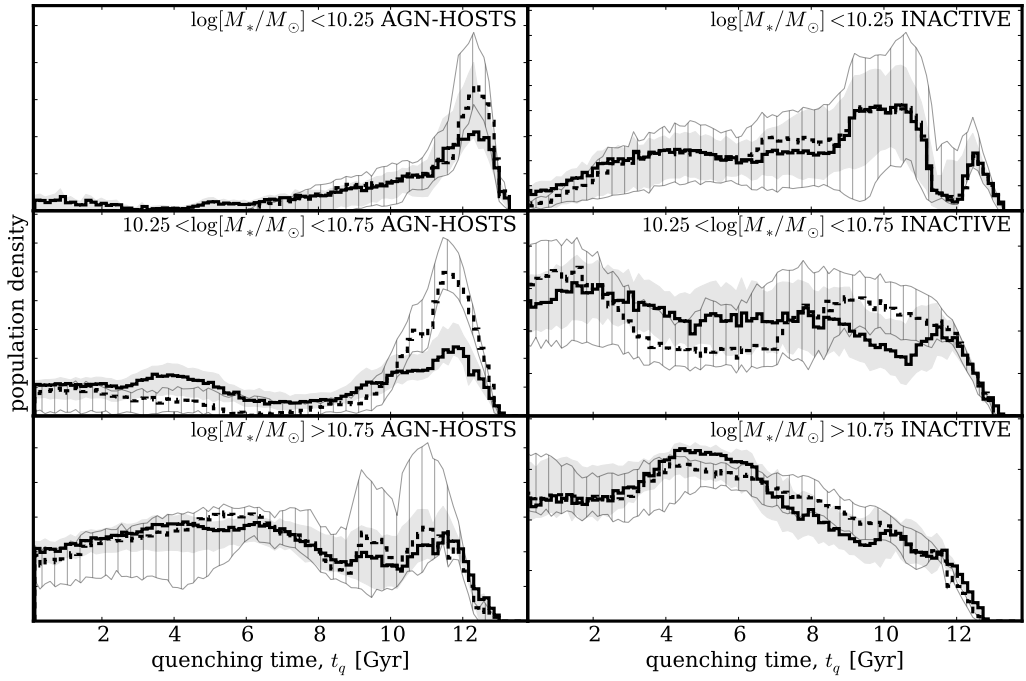


Figure 4.7: Population density distributions for the quenching time ( $t_q$ ) parameter, normalised so that the areas under the curves are equal. AGN-HOST (left) and INACTIVE (right) galaxies are split into low (top), medium (middle) and high (bottom) mass for smooth (dashed) and disc (solid) galaxies. Uncertainties from bootstrapping are shown by the shaded regions for the smooth (grey striped) and disc (grey solid) population densities. A low (high) value of  $t_q$  corresponds to the early (recent) Universe.

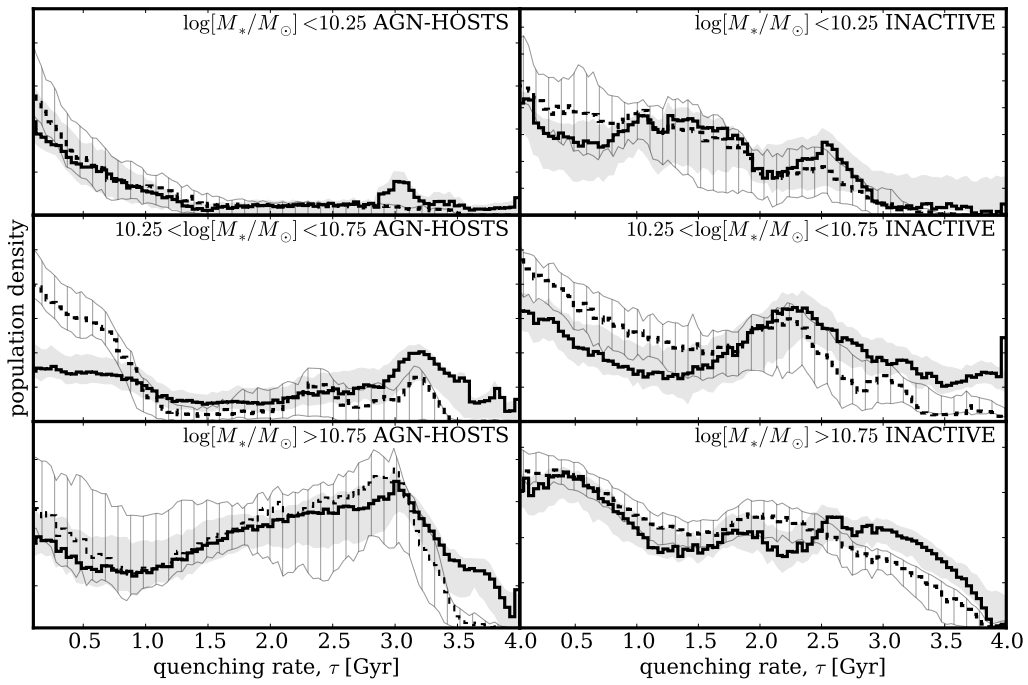


Figure 4.8: Population density distributions for the quenching rate ( $\tau$ ), normalised so that the areas under the curves are equal. AGN-HOST (left) host and INACTIVE (right) galaxies are split into low (top), medium (middle) and high (bottom) mass for smooth (dashed) and disc (solid) galaxies. Uncertainties from bootstrapping are shown by the shaded regions for the smooth (grey striped) and disc (grey solid) population densities. A small (large) value of  $\tau$  corresponds to a rapid (slow) quench.

Table 4.3: Table showing the number of galaxies in each of the three mass bins for both the AGN-HOSTS and INACTIVE galaxy samples and the percentage of the distribution across each morphologically weighted population found in the rapid, intermediate and slow quenching regimes.

SAMPLE	MASS BIN	WEIGHTING	$\tau < 1$ [Gyr]	$1 < \tau$ [Gyr] $< 2$	$\tau > 2$ [Gyr]	NUMBER
AGN-HOSTS	$\log[M_*/M_\odot] < 10.25$	$p_d$	$60 \pm^{23}_{14}$	$13 \pm^9_{6}$	$28 \pm^6_{19}$	165(13.3%)
		$p_s$	$69 \pm^4_{6}$	$17 \pm^{14}_{14}$	$14 \pm^3_{7}$	
	$10.25 < \log[M_*/M_\odot] < 10.75$	$p_d$	$33 \pm^3_{5}$	$15 \pm^4_{4}$	$51 \pm^4_{7}$	
INACTIVE		$p_s$	$69 \pm^5_{5}$	$7 \pm^4_{4}$	$26 \pm^5_{9}$	630(50.6%)
	$\log[M_*/M_\odot] > 10.75$	$p_d$	$20 \pm^5_{4}$	$25 \pm^7_{5}$	$56 \pm^8_{12}$	
		$p_s$	$24 \pm^4_{4}$	$26 \pm^6_{6}$	$50 \pm^7_{7}$	
INACTIVE	$\log[M_*/M_\odot] < 10.25$	$p_d$	$37 \pm^8_{14}$	$39 \pm^8_{9}$	$24 \pm^8_{6}$	807(13.2%)
		$p_s$	$47 \pm^{11}_{11}$	$36 \pm^5_{5}$	$17 \pm^4_{5}$	
	$10.25 < \log[M_*/M_\odot] < 10.75$	$p_d$	$30 \pm^4_{3}$	$18 \pm^2_{3}$	$51 \pm^4_{4}$	
INACTIVE		$p_s$	$42 \pm^2_{2}$	$29 \pm^3_{3}$	$30 \pm^4_{4}$	3094(50.7%)
	$\log[M_*/M_\odot] > 10.75$	$p_d$	$36 \pm^3_{3}$	$24 \pm^3_{4}$	$41 \pm^4_{3}$	
		$p_s$	$38 \pm^2_{2}$	$28 \pm^3_{4}$	$34 \pm^3_{3}$	

and slow ( $\tau > 2$  Gyr) quenching rates in each of the three mass bins. Uncertainties on the population densities (shown by the shaded regions) are determined from the maximum and minimum values spanned by  $N = 1000$  bootstrap iterations, each sampling 90% of the galaxy population.  $1\sigma$  uncertainties are quoted for the percentages in Table 4.3, calculated from the bootstrapped distributions.

At all masses, the population density for galaxies within the AGN-HOST population across the quenching time,  $t_q$  (left panels of Figure 4.7), is different from that of the inactive galaxies (right panels of Figure 4.7). Recent quenching ( $t > 11$  Gyr) is the dominant history for low and medium mass AGN-HOST galaxies, particularly for the smooth weighted population hosting an AGN (solid lines, left panels Figure 4.7). However, this effect is less dominant in higher mass galaxies where quenching at earlier times also has high density (bottom left panel of Figure 4.7).

The population densities for the quenching rate,  $\tau$ , in Figure 4.8 and Table 4.3 show the dominance of rapid quenching ( $\tau < 1$  Gyr) within the AGN-HOST population, particularly for smooth galaxies (solid lines, left panels Figure 4.8). With increasing mass the dominant quenching rate becomes slow ( $\tau > 2$  Gyr). Similar trends in the population density are observed for the INACTIVE population (right panels Figure 4.8) but the overall distribution is very different.

In Figure 4.6 there is no INACTIVE control sample to act as a comparison, since an Eddington ratio cannot be measured for a black hole that is not accreting. The population densities for the AGN-HOST samples however, show the dominance of rapid and recent quenching as the Eddington ratio increases (i.e. higher black hole accretion

rates). A bimodal distribution can be seen for the low Eddington ratio AGN-HOST population (top right panel of Figure 4.6) between both rapid and slow quenching rates.

The population densities for the AGN-HOST galaxies therefore all show evidence for the dominance of rapid, recent quenching. This result implies the importance of AGN feedback for the evolution within this population.

#### 4.1.4 Discussion

The differences between the population density distributions of the AGN-HOST and INACTIVE populations in Figures 4.7 & 4.8 reveal that an AGN can have a significant effect on the SFH of its host galaxy. Both recent, rapid quenching and early, slow quenching are observed in the population densities of the AGN-HOST population.

There are however minimal differences between the smooth and disc weighted distributions of the quenching parameters within the AGN-HOST population (comparing solid and dashed lines in the left panels of Figures 4.6 - 4.8). This is agreement with the conclusions of Kauffmann et al. (2003a) who found that the structural properties of AGN hosts depend very little on AGN power. Quenching caused by AGN feedback is therefore morphologically independent; this is unlike the mechanisms discussed in Chapter 3.

Quenching at early times is observed within the INACTIVE population (see right panels of Figure 4.7), where the population density is roughly constant until recent times where the distribution drops off. This drop-off occurs at earlier times with increasing mass, with a significant lack of quenching occurring at early times for low mass INACTIVE galaxies (top right panel Figure 4.7). This is evidence of downsizing within the INACTIVE galaxy population whereby stars in massive galaxies form first and quench early (Cowie et al., 1996; Thomas et al., 2010).

The population densities for smooth weighted higher mass (bottom left panels Figures 4.7 & 4.8) and lower Eddington ratio (top panels Figure 4.6) AGN-HOST galaxies are also dominated by slow, early quenching. This implies that AGN feedback is not responsible for the cessation of star formation within a proportion of these galaxies, as this quenching has occurred prior to the triggering of the current AGN. I speculate that this is also due to the effects of downsizing rather than being caused

by the current AGN. Since the lower Eddington ratio AGN-HOST population is also dominated by this early quenching at slow rates (top panels Figure 4.6) this supports the idea that the AGN is not strong enough to be the cause of this quenching. This earlier evolution would first form a slowly ‘dying’ or ‘dead’ galaxy typical of massive elliptical galaxies which could then have a recent infall of gas either through a minor merger, galaxy interaction or environmental change, triggering further star formation and feeding the central black hole, triggering an AGN (Kaviraj, 2014a). In turn this AGN can then quench the recent boost in star formation. This track is similar to the evolution history proposed for blue ellipticals (Kaviraj et al., 2013; McIntosh et al., 2014; Haines et al., 2015, and detected in the top panel of Figure 3.7). This SFH would then give rise to the distribution seen within the high mass smooth weighted AGN-HOST population for both time and rate parameters (bottom panels of Figures 4.7 & 4.8).

Alternatively in the high mass disc weighted AGN-HOST population, in which slow, early quenching is also observed (dashed lines bottom left panels of Figures 4.7 & 4.8) this evolution could be due to initially isolated discs evolving slowly by the Kennicutt-Schmidt (Schmidt, 1959; Kennicutt, 1997) law which can then undergo an interaction or merger to reinvigorate star formation, feed the central black hole and trigger an AGN (Varela et al., 2004; Emsellem et al., 2015). These galaxies would need a large enough gas reservoir to fuel both SF throughout their lifetimes and the recent AGN. These high mass galaxies also play host to the most luminous AGN (mean  $\log(L[OIII] [\text{erg s}^{-1}]) \sim 41.6$ ) and so this SFH challenges the typical merger driven co-evolution of luminous black holes and their host galaxies (see Section 4.2 for an investigation into an alternative merger free black hole-galaxy co-evolution).

These recently triggered, low accretion rate AGN in both massive disc and smooth galaxies do not have the ability to impact the SF across the entirety of a high mass galaxy in a deep gravitational potential (Ishibashi & Fabian, 2012; Zinn et al., 2013). This leads to the lower peak for recent, rapid quenching within the high mass, low Eddington ratio AGN-HOST population for both morphologies (left bottom panels of Figures 4.7 & 4.8 and top panels of Figure 4.6).

Conversely, rapid quenching, possibly caused by the AGN itself through negative feedback, is the most dominant history within the low mass (left top panel Figure 4.8) and high Eddington ratio (bottom left panel of Figure 4.6) AGN-HOST population. Within the medium mass AGN-HOST population a bimodal distribution between these

two quenching histories is seen (left middle panel Figure 4.8), highlighting the strength of this method which is capable of detecting such variation in the SFHs within a population of galaxies. These lower and medium mass galaxies have lower gravitational potentials from which gas may be more readily expelled or heated (Tortora et al., 2009) by jets launched by the strongly accreting AGN.

Tortora et al. (2009) model the effects of this jet-induced AGN feedback on a typical early-type galaxy and observe a drastic suppression of star formation on a timescale of  $\sim 3$  Myr. Comparing their synthetic colours with observed colours of SDSS elliptical galaxies, they find the time between the current galaxy age,  $t_{\text{gal}}$  and the time that the feedback began,  $t_{\text{AGN}}$ , peaks at  $t_{\text{gal}} - t_{\text{AGN}} \sim 0.85$  Gyr. In the top panel of Figure 4.7, the population density for low mass AGN-HOST galaxies has a difference between the peak of the distribution and the average age of the population (galaxy age is calculated as the age of the Universe at the observed redshift, by assuming all galaxies form at  $t = 0$ ) of  $\sim 0.83$  Gyr. This is in agreement with the timescales for AGN feedback driven quenching derived in the simulations by Tortora et al. (2009). This implies that this SFH dominated by recent quenching is *caused* directly by negative AGN feedback.

Rapid quenching is particularly dominant for low-to-medium mass smooth galaxies as seen in the level panels of Figure 4.8. In Chapter 3 I discussed how these incredibly rapid quenching rates could be attributed to mergers of galaxies in conjunction with AGN feedback, which are thought to be responsible for creating the most massive smooth galaxies (Conselice et al., 2003; Springel et al., 2005; Hopkins et al., 2008a). This dominance of rapid quenching across the smooth AGN-HOST population (solid lines in left panels of Figure 4.8) supports this hypothesis that a merger, having caused a morphological transformation to a smooth galaxy, can also trigger an AGN, causing feedback and cessation of star formation (Sanders et al. 1988; Pontzen et al. 2016).

Simulations by Sparre & Springel (2016) show that major merger remnants are only quenched when the prescription used for AGN feedback in the model is stronger than their initial fiducial level. They increase the strength of their AGN feedback by decreasing the metallicity,  $Z$ , of the gas accreted by the black hole; this impacts on the cooling function of the gas  $\Lambda(T, Z)$  (see Section 2.1 of Sparre & Springel, 2016). This suggests that AGN feedback will therefore have a larger effect on galaxies with lower metallicity. Considering the mass-metallicity relation (Tremonti et al., 2004), it

follows from this argument that AGN feedback will have a greater effect on galaxies with lower mass. This provides more support to the hypothesis that the dominance of rapid, recent quenching across the low and medium mass AGN-HOST population (left panels Figures 4.7 & 4.8) is caused directly by the AGN.

This mechanism of AGN feedback was originally proposed to regulate the number galaxies at the bright (or high mass) end of the luminosity function in cosmological simulations (see Chapter 1). The shape of the observed K-band luminosity function can be seen in Figure 4.9 (Figure 1 from Benson et al., 2003), falling away from model estimates below a K-band magnitude of  $M_K - 5 \log_{10} h \sim 23.5$ , or above an approximate stellar mass of  $\log_{10}[M_*/M_\odot] \gtrsim 10.3$ , assuming a mass-to-light ratio of  $(M/L)_K = 0.8$  (Brinchmann & Ellis, 2000). However, it is the low and medium mass AGN-HOST populations where this rapid recent quenching is dominant (see left panels Figures 4.7 & 4.8). At first this seems contradictory to the arguments posed to constrain the shape of the luminosity function, but with some thought the two results can be reconciled.

The knee of the luminosity function is the point at which AGN feedback starts to impact the masses of galaxies; this occurs at  $\log_{10}[M_*/M_\odot] \gtrsim 10.3$ , which lies at the lower edge of the medium mass AGN-HOST population studied here. The quenching observed in the low and medium mass AGN-HOST populations will stop the masses of these galaxies from growing any larger in the future. In turn these now quenched galaxies will contribute to dry mergers, which would otherwise have had high gas fractions; limiting the mass of the merger remnants. The combination of these two effects, caused initially by the quench of a lower mass galaxy by negative AGN feedback, will reduce the number of galaxies which will be able to grow to populate the high mass end of the luminosity function.

However, there still remains the possibility that the AGN is not the cause of the quenching observed, but merely a *consequence* of an alternative quenching mechanism. This idea is supported by simulations showing that the exhaustion of gas by a merger fuelled starburst could cause such a rapid quench in star formation and in turn also trigger an AGN (Croton et al., 2006; Wild et al., 2009; Snyder et al., 2011; Hayward et al., 2014). Yesuf et al. (2014) also showed that AGN are more commonly hosted by post starburst galaxies, with the peak AGN activity appearing  $\geq 200 \pm 100$  Myr after the starburst. Such a SFH is not accounted for in the models presented here (see Section 7.2 for a discussion), however this scenario is still consistent with the results

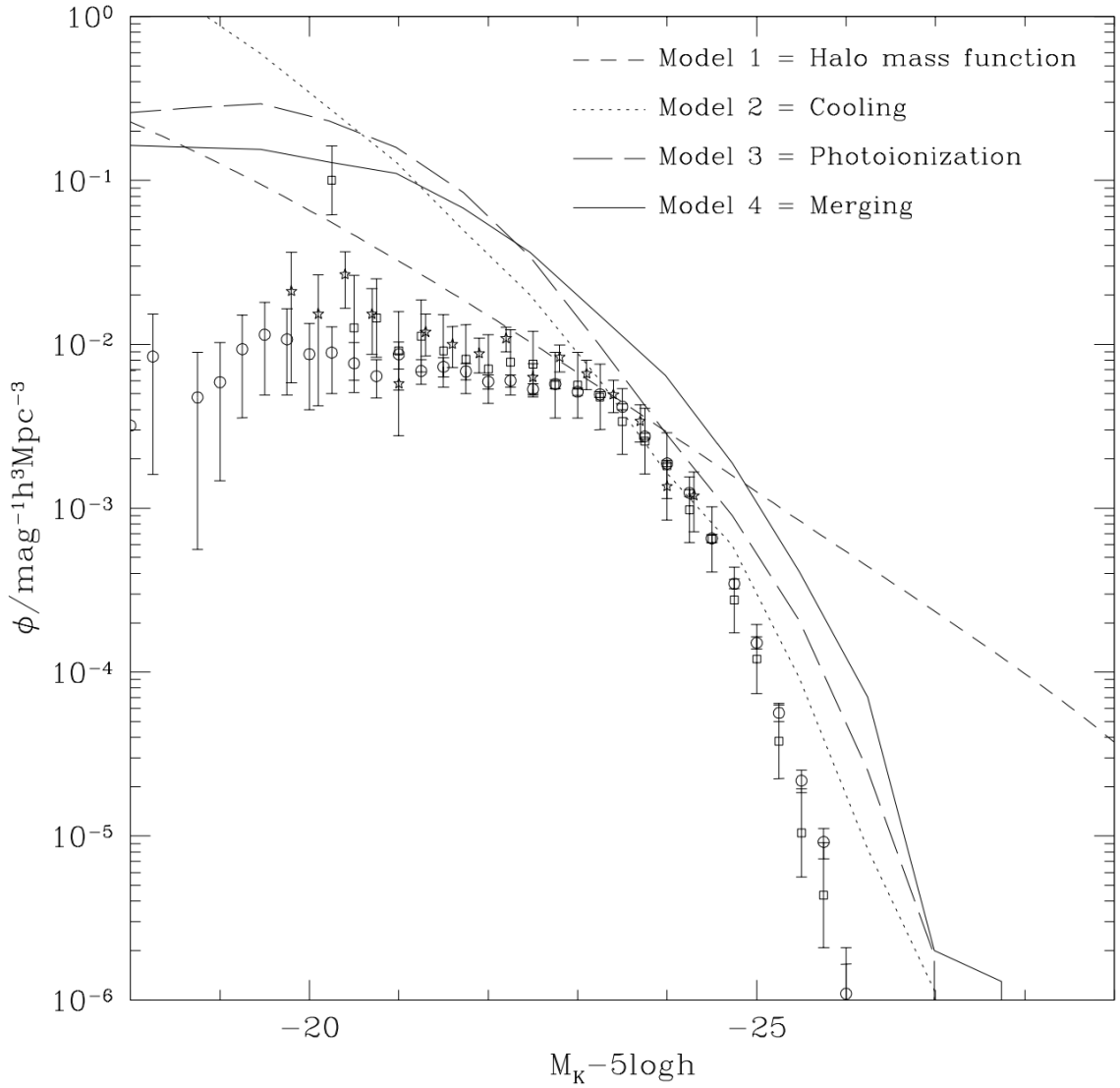


Figure 4.9: Figure 1 from Benson et al. (2003) showing the K-band luminosity function of galaxies, with  $h = 0.65$ . The points show the observational determinations of (Cole et al., 2001, circles), (Kochanek et al., 2001, squares), and (Huang et al., 2003,  $z < 0.1$ , stars). Lines show model results investigated by Benson et al. (2003) to determine what shapes this luminosity function; they concluded that including prescriptions for AGN feedback (supernova feedback winds) can help match the simulations to the data at the bright (faint) end of the luminosity function. The knee of the function occurs at  $M_K - 5 \log_{10} h \sim 23.5$ , which is an approximate stellar mass of  $\log_{10}[M_*/M_\odot] \sim 10.3$ , assuming a mass-to-light ratio of  $(M/L)_K = 0.8$  (Brinchmann & Ellis, 2000).

presented in this paper; that AGN which are *currently* active have been detected in host galaxies  $\sim 1$  Gyr after the onset of quenching. Solving this issue of *cause* vs. *consequence* will not be possible with the currently available SDSS photometry. The advent of Integral Field Unit (IFU) surveys with many aperture fibres per galaxy per observation (such as the MaNGA (Bundy et al., 2015), SAMI (Croom et al., 2012) and CALIFA (Sánchez et al., 2012) surveys) will allow this problem to be studied by observing the change in quenching parameters with increasing distance from the galaxy nucleus (see Section 7.2 for a more detailed discussion).

Not all galaxies in the AGN-HOST and INACTIVE samples are quenching (as seen in Figure 4.5) with a significant proportion of both the AGN-HOST and INACTIVE samples lying on the star forming ‘main sequence’. A galaxy can therefore still maintain star formation whilst hosting an AGN. The results presented in Section 4.1.3 only reflect the trends for galaxies that have undergone or are currently undergoing quenching within the AGN-HOST population and can therefore be accurately fit by an exponentially declining SFH. This prevalence of star forming AGN host galaxies, combined with the results above allows us to consider that either: (i) the AGN are the cause of the rapid quenching observed but only in gas-poor host galaxies where they can have a large impact, (ii) the AGN are a consequence of another quenching mechanism but can also be triggered by other means which do not cause quenching, or (iii) the SFR of a galaxy can recover post-quench and return to the star forming sequence after a few Gyr (see recent simulations by Pontzen et al. 2016 and Sparre & Springel 2016). Further investigation will therefore be required to determine the nature of this quenching (see Section 7.2 for a discussion of proposed future work).

## 4.2 Bulgeless galaxies hosting growing black holes

*The work in the following chapter is in preparation for submission to MNRAS in Simmons, Smethurst & Lintott (in prep.). I was responsible for the spectral data reduction and statistical analysis and assisted in the interpretation of the results.*

Although the study of large populations of galaxies provides crucial information to constrain the processes governing galaxy evolution, valuable insight can still be discerned from detailed observations of a smaller sample of rare objects.

The strong correlations that exist between black hole mass and bulge luminosity (Marconi & Hunt, 2003; Häring & Rix, 2004), velocity dispersion (Magorrian et al., 1998; ?; ?; ?; McConnell et al., 2011) and total stellar mass (Cisternas et al., 2011) suggest a co-evolution of a galaxy with its central super massive black hole (SMBH). Since mergers can grow both bulges and black holes these correlations have been interpreted as the result of a few mergers within a Hubble time (?Hopkins et al., 2008b; ?). A growing black hole must accrete matter and is therefore observed as an AGN during this time period. Understanding the triggering mechanisms of AGN which kick-start this process of both galaxy and black hole growth and possible subsequent feedback from the AGN, is therefore important. However in Section 4, I presented the argument that disc galaxies currently hosting an AGN could have started quenching at early times with very slow quenching rates, suggesting an alternative to this typical merger driven galaxy-black hole coevolution scenario (Hopkins et al., 2008b).

A secular co-evolution of galaxy and black hole has been proposed by previous works (??Cisternas et al., 2011; ?; Schawinski et al., 2011; Kocevski et al., 2012) and was investigated by Simmons et al. (2013) who studied 13 AGN residing in disc dominated host galaxies, whose accretion histories are assumed to be merger free. In the following work I examine a larger sample of disc galaxies visually identified as bulgeless or disc dominated hosting an AGN and investigate the locations of these galaxies on typical galaxy-black hole scaling relations. Since the disc galaxies in this sample have different dynamical histories to bulge dominated galaxies, their black hole masses are not expected to correlate in the same way to their stellar masses if different dynamical histories lead to different mechanisms for black hole growth.

### 4.2.1 Observational Data

The goal of this study is to investigate black hole growth in galaxies whose growth histories have been dominated by relatively calm, slow processes. A sample of growing (i.e. active) black holes hosted in disc-dominated galaxies is therefore required. Optimally, the AGN should have broad emission lines to facilitate measurement of black hole masses via well-established relations between line flux and width and black hole masses. Previously, Simmons et al. (2013) investigated a sample of 13 pure disc galaxies hosting AGN. The selection method used in that study selected against very massive black holes with unobscured emission: only 2 AGN of 13 showed clear signs of broadened line emission in their SDSS spectra, leading to calculated black hole masses of  $4 \times 10^6 M_\odot$  and  $1 \times 10^7 M_\odot$ . Here the aim is to select AGN hosted in disc-dominated galaxies at all masses with broad emission lines that can be used to calculate black hole masses through virial assumptions (see Section 4.2.2.4). Below the methods used to select both a disc dominated AGN sample along with a control sample of typical AGN host galaxies are described.

#### 4.2.1.1 AGN Selection

In order to examine the black hole-galaxy scaling relation for such galaxies, first a sample of unobscured AGN with broad emission lines must be selected, so that black hole masses may be measured from well-established correlations between emission line properties, such as the FWHM of the broadened  $H\alpha$  emission line, and black hole masses (e.g., Greene & Ho, 2007; Jiang et al., 2011; Xiao et al., 2011; Peterson, 2014).

Unobscured AGN have characteristic colours in multi-wavelength imaging, particularly in X-ray, optical and infrared bands (Kauffmann et al., 2003a; Stern et al., 2005; Goulding & Alexander, 2009; Kauffmann & Heckman, 2009; Aird et al., 2012; Mendez et al., 2013; Azadi et al., 2016; Cowley et al., 2016; Harrison et al., 2016). Given the existence of all-sky surveys at many of the wavelengths relevant to the selection of unobscured AGN, it is now possible to construct larger samples of sources identified as unobscured AGN with high likelihood.

An initial sample of AGN was selected using the W2R sample of Edelson & Malkan (2012), comprised of 4316 sources identified using multi-wavelength data from the

*Wide-field Infrared Survey Explorer* (*WISE*; Wright et al., 2010), Two Micron All-Sky Survey (2MASS; Skrutskie et al., 2006), and *ROSAT* all-sky survey (RASS; Voges et al., 1999). This multi wavelength photometric, all-sky selection, selects unobscured AGN at  $> 95$  per cent confidence (Edelson & Malkan, 2012).

#### 4.2.1.2 Selecting disc-dominated AGN host galaxies

Following the selection of AGN using the catalog of Edelson & Malkan (2012) described in the previous section, galaxies imaged by the Sloan Digital Sky Survey are then further sub-selected. There are 1,844 W2R sources with positional matches having reported coordinates within  $3''$  of a source in the SDSS (York et al., 2000) Data Release 8, a fraction consistent with the fractional area of the SDSS versus an all-sky catalog.

Each SDSS ugriz colour cutout was then examined to identify disc-dominated features. 101 disc-dominated AGN host galaxies were identified on the basis of clearly identifiable spiral arms, bars or obvious edge-on discs. I shall refer to these galaxies as the DISCDOM sample. Figures 4.10 & 4.11 collectively show the SDSS postage stamps for all galaxies in the sample, with all images showing the expected bright nebular emission of the unobscured AGN.

#### 4.2.1.3 Spectra

Of the 101 disc-dominated AGN host galaxies with SDSS imaging observations, 96 have spectra from SDSS Data Release 9 (Ahn et al., 2012). 23 of which were first identified as AGN by Shen et al. (2008) and Edelson & Malkan (2012). Example spectra centred around the broad  $H\alpha$  emission at  $6562\text{\AA}$  for 5 of these SDSS spectra are shown in Figure 4.12.

The broad  $H\alpha$  emission for 5 additional sources were measured using long-slit spectra using Intermediate Dispersion Spectrograph (IDS) on the Isaac Newton Telescope (INT) from 21st-23rd May 2014. I reduced spectra using the standard reduction pipeline of Massey, Valdes & Barnes (1992) using IRAF modules to debiase, dark subtract, flat field, calibrate, sky subtract, flux calibrate and extract spectra. The redshift of these sources was also measured from the reduced spectra, using the

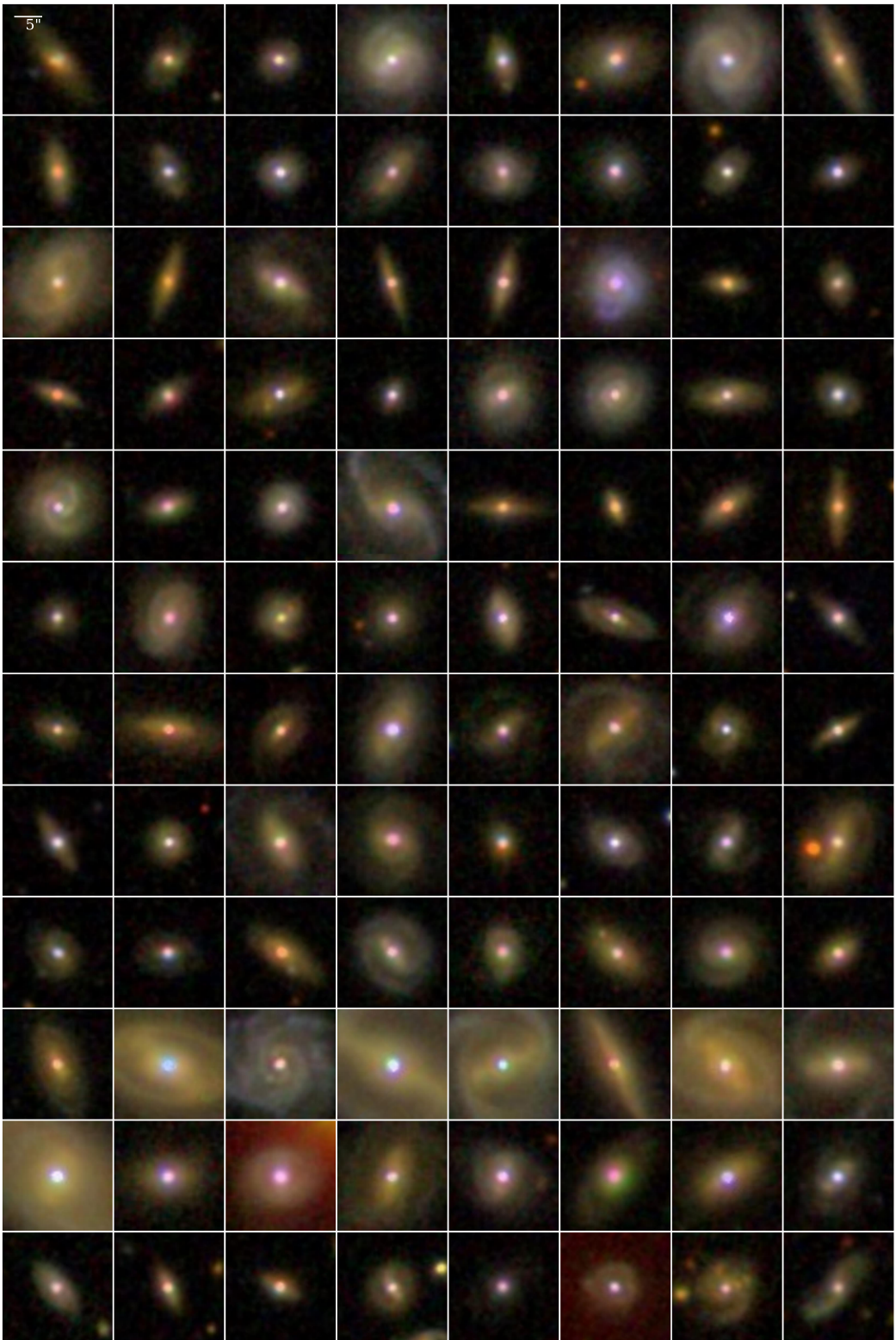


Figure 4.10: Postage stamp SDSS images of the 96 galaxies within the DISCDOM sample for which SDSS spectra were available. The scale for each image is shown by the 5" ruler in the top left panel.

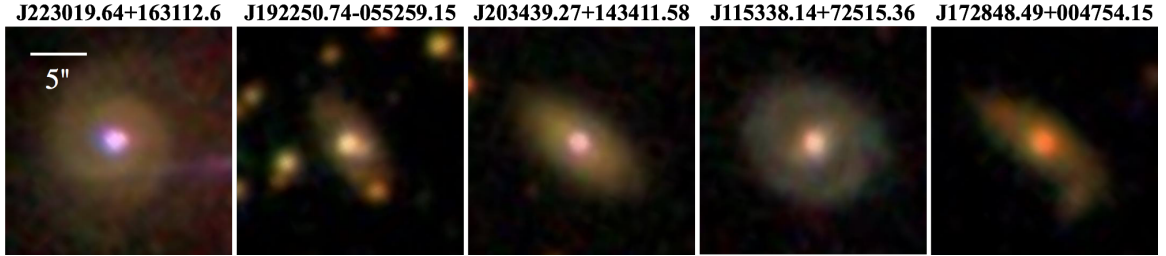


Figure 4.11: Postage stamp SDSS images of the 5 galaxies observed with the IDS on the INT within the DISCDOM sample. The scale for each image is shown by the 5" ruler in the left panel.

peak of the broadened  $H\alpha$  emission to measure  $\lambda_{obs}$ . These reduced spectra, centred around the broad  $H\alpha$  emission at  $6562\text{\AA}$ , are shown in Figure 4.13 for the 5 galaxies observed.

Figure 4.14 shows the redshift distribution of all 101 sources for which we have spectra; the mean redshift of the sample is  $\langle z \rangle = 0.129$ , with the highest-redshift source having  $z = 0.244$ .

#### 4.2.1.4 Selecting a Control Sample

Since the majority of the galaxies in the DISCDOM sample have been observed using SDSS, I constructed a control sample from the SDSS quasar catalog of Shen et al. (2011). Using this sample I compiled a sample of 191 galaxies which were redshift matched to within  $\pm 5\%$  of the DISCDOM sample. I shall refer to these galaxies as the QSOCONTROL sample. 124 of the QSOCONTROL sample also had measured ( $B/T$ ) ratios from Simard et al. (2011, matched with a 3" search radius, see Section 4.2.2.2).

This provides a control sample of ‘typical’ AGN host galaxies representative of the population in the redshift range probed in this study.

#### 4.2.2 Galaxy and Black Hole Properties

In order to study the relation between galaxy and black hole in these disc dominated systems, their properties shall be compared to well tested black hole-galaxy scaling relations. The most famous of these scaling relations is the  $M - \sigma$  relations. This is a

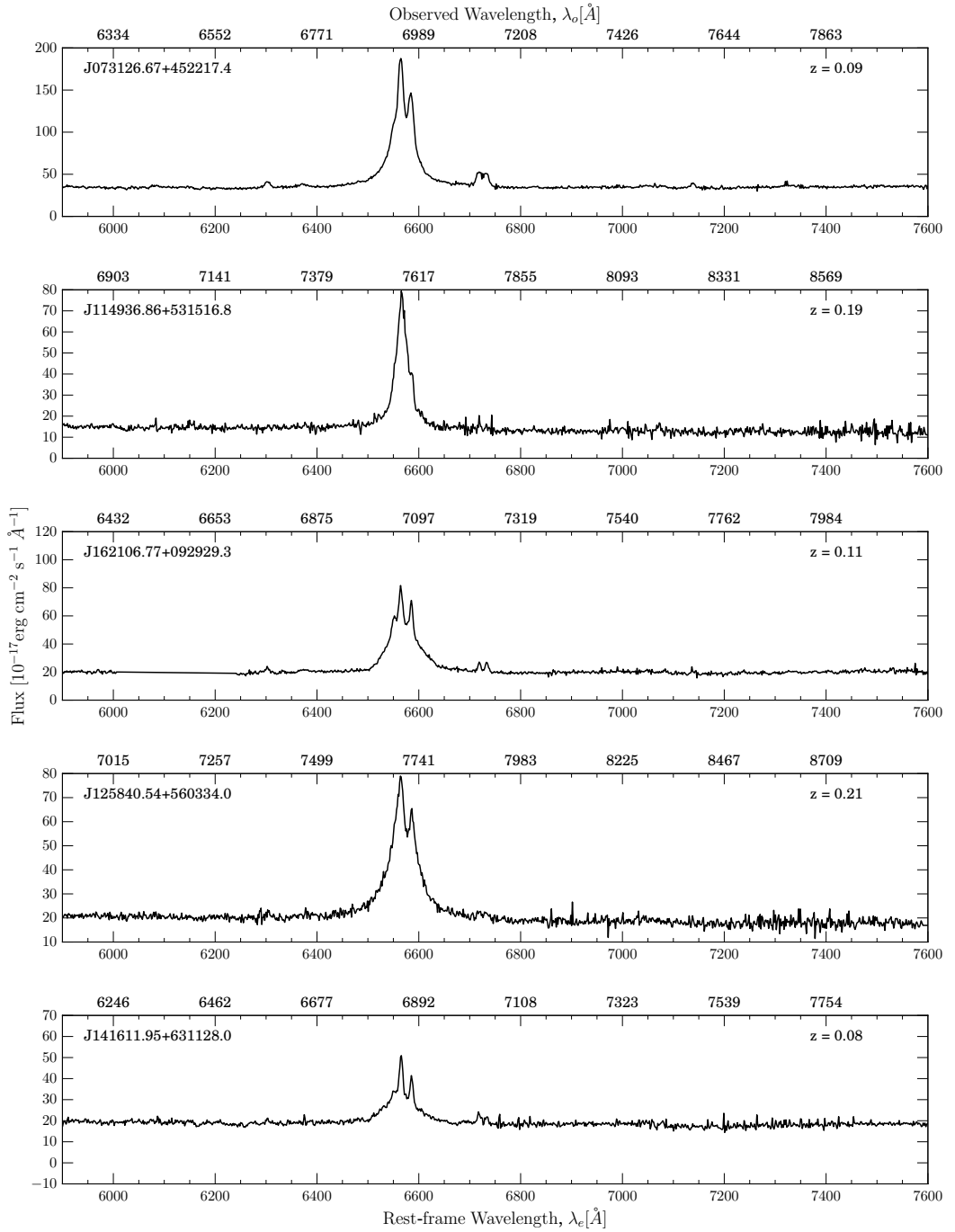


Figure 4.12: 5 example SDSS spectra from with the corresponding measured redshift values shown. Each panel shows the same rest-frame wavelength range (bottom axis of each panel); observed wavelengths are shown on the top axis of each panel. All spectra show broadened  $H\alpha$  emission, confirming that the multi-wavelength AGN selection employed here efficiently selects unobscured AGN.

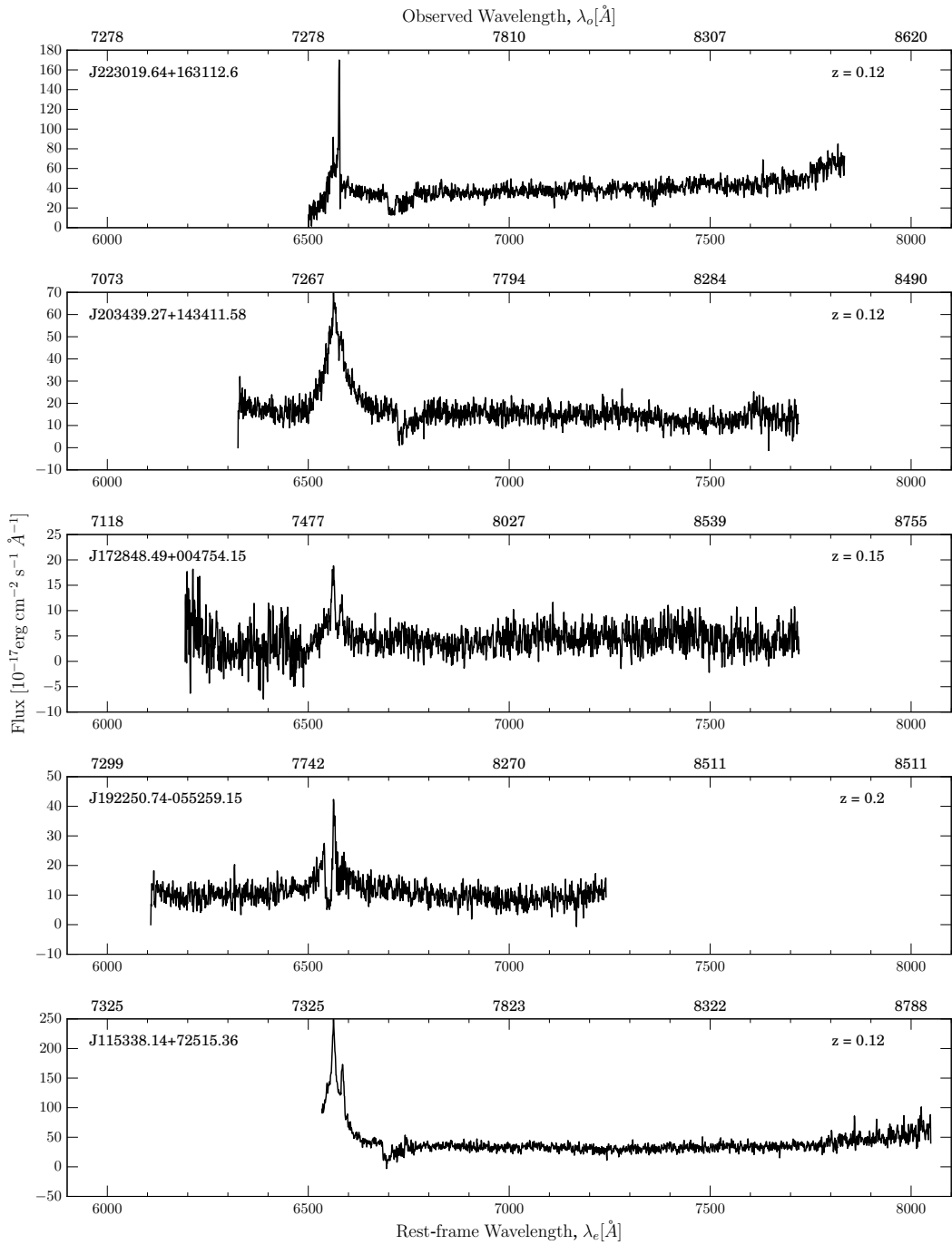


Figure 4.13: Reduced spectra from the IDS on the INT for the 5 galaxies observed. Each panel shows the same rest-frame wavelength range (bottom axis of each panel); observed wavelengths are shown on the top axis of each panel, with redshifts in the top right of each panel. All spectra one again show broadened  $H\alpha$  emission, confirming that the multi-wavelength AGN selection employed here efficiently selects unobscured AGN.

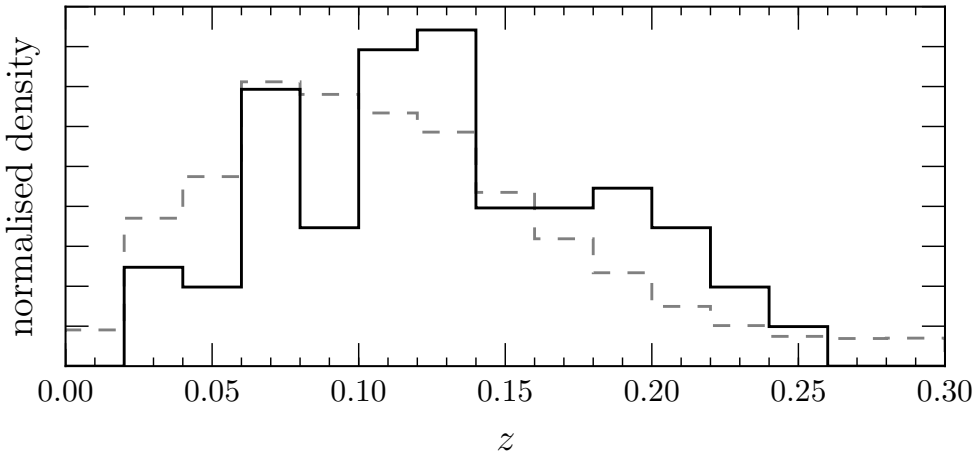


Figure 4.14: Normalised redshift distribution for all 101 sources (solid) for which we have spectra, either from SDSS or measurements with the IDS on the INT. Also shown is the overall redshift distribution of SDSS DR7 in the relevant redshift range of our sources (dashed).

well studied relationship (Magorrian et al., 1998; ?; Kormendy & Gebhardt, 2001; ?; ?; Graham, 2007; ?; ?; McConnell et al., 2011; ?; ?) and is hypothesised to arise due to the merger driven co-evolution increasing the mass of the black hole at the same time as increasing the velocity dispersion of the galaxy (?Hopkins et al., 2008b; Jahnke & Macciò, 2011). The black hole mass has similarly been found to correlate with the stellar mass of the galaxy bulge (Marconi & Hunt, 2003; Häring & Rix, 2004) and the total galaxy stellar mass (Cisternas et al., 2011). In order to test where the galaxies of the DISCDOM sample lie in these parameter planes in comparison to ‘typical’ AGN host galaxies, black hole, total and bulge stellar masses were derived for each galaxy. In the following section I describe how this was achieved across the DISCDOM sample.

#### 4.2.2.1 Photometry

The AGN contribution to the magnitude of each galaxy,  $m_{\text{gal}}$ , is calculated by subtracting the flux in the SDSS `psfMag`,  $m_{\text{psf}}$ , from the flux in `modelMag`,  $m_{\text{model}}$  in a given wave band,  $b$  as follows:

$$m_{b,\text{gal}} = -2.5 \log_{10} \left[ 10^{\left( \frac{m_{b,\text{model}}}{-2.5} \right)} - 10^{\left( \frac{m_{b,\text{psf}}}{-2.5} \right)} \right], \quad (4.4)$$

since the normalisation constants in the flux-magnitude conversion will be constant for different sized apertures in a given band. `psfMag` is the best estimate of unresolved emission, while `modelMag` is the optimal quantity for computing aperture-matched source colours<sup>1</sup>. A galaxy magnitude in both the SDSS  $u$  and  $r$  bands was calculated in order to determine the galaxy  $u - r$  colour.

A similar NUV galaxy magnitude can be calculated using the GALEX apertures, however matching these apertures to those provided by SDSS cannot be done with a large enough degree of accuracy to derive a reliable galaxy  $NUV - u$  colour. This therefore means that STARPY cannot be run on these unobscured AGN of the DISCDOM sample. However, the locations of the DISCDOM sample on the optical colour-magnitude diagram can still be explored; this is studied in Section 5.2 (see Figure ??).

#### 4.2.2.2 Total stellar masses

Total stellar masses are calculated using the well-studied relation between stellar mass, absolute galaxy  $r$ -band magnitude,  $M_{r,\text{gal}}$ , and  $u - r$  galaxy colour (corrected for galactic extinction; Schlegel et al., 1998), following the method of Baldry et al. (2006, see Section 1). Uncertainties are propagated from the colour-magnitude relationship and due to the subtraction of the central AGN component. The average uncertainty on each measurement is  $\sim 0.3$  dex. The distribution of the stellar masses calculated for the DISCDOM sample is shown in the right panel of Figure 4.17.

#### 4.2.2.3 Bulge stellar masses

Calculation of the bulge stellar mass for the DISCDOM sample is more complicated than the stellar mass in the previous section. The nuclear emission (as estimated via comparison of `psfMag` to `modelMag`) is generally between 20 to 200 per cent of the galaxy-only emission. The presence of the luminous AGN therefore severely compromises the estimates of the bulge-to-total ratio, ( $B/T$ ), in the host galaxy provided by, e.g., the `fracDev` parameter reported in the SDSS catalogs. The `fracDev` parameter estimates that  $\sim 80\%$  of the galaxies in this sample are pure de Vaucouleurs (1953) bulges in the  $r$ -band, despite the fact that the sample was selected on the basis of clear visual signatures of dominant discs (Figure 4.10). None of the photometric

---

<sup>1</sup><https://www.sdss3.org/dr10/algorithms/magnitudes.php>

parameters measured by the SDSS pipeline allow for the dual presence of an AGN and a host galaxy. Without such considerations the unresolved AGN light is likely to be attributed to the compact bulge component in a bulge-disc model fit (Simmons & Urry, 2008; Koss et al., 2011).

AGN-host decomposition based on 2-dimensional image fitting (e.g., Simard, 1998; Peng et al., 2002, 2010) is more reliable (e.g. McLure et al., 1999; Urry et al., 2000; McLure & Dunlop, 2001; Sánchez et al., 2004; Pierce et al., 2007; Gabor et al., 2009; Simmons et al., 2011, 2013; Koss et al., 2011). However even in high-resolution *Hubble Space Telescope (HST)* images (Simmons & Urry, 2008) or SDSS imaging at  $z \gtrsim 0.06$  (Koss et al., 2011; ?) the recovered bulge-to-total ratio can be highly uncertain, particularly for disc-dominated galaxies with a small bulge or pseudo-bulge (Kormendy & Kennicutt, 2004) component. While the AGN-host decompositions of the galaxies studied by ? recovered reliable bulge-to-total ratios for 11 of the 13 galaxies, those sources were at substantially lower redshift than this sample (with the majority at  $z < 0.08$ ), and their AGN were significantly less luminous ( $L_{bol} \lesssim 10^{44}\text{erg s}^{-1}$ , whereas in the DISCDOM sample  $L_{bol} \gtrsim 10^{44}\text{erg s}^{-1}$ , see Section 4.2.2.5).

Bulge-to-total fits were first undertaken for the 5 galaxies observed at the INT with the IDS in the DISCDOM sample using the GALFIT software (Peng et al., 2002); the results of which are shown in Figure 4.15. I used a Sérsic light profile (Sérsic, 1968) to model bulge and disc components, defined by an effective radius,  $R_e$ , and light concentration index,  $n$ , as:

$$I(R) = I_e \exp \left( -b_n \left[ \left( \frac{R}{R_e} \right)^{1/n} - 1 \right] \right), \quad (4.5)$$

where  $I_e$  is the intensity at the effective radius,  $R_e$  and  $b_n$  is a constant defined in relation to the sérsic index,  $n$ . Typical disc (bulge) profiles have  $n = 1$  ( $n = 3$ ). Each of the galaxies observed with the INT were fitted with a disc, bulge and PSF component (to account for the bright nuclear emission of the AGN). PSFs were extracted from the SDSS FITS images using the standard `read_PSF` IDL code provided by the SDSS <sup>2</sup>. Initial guesses of  $n = 2.5$  are used on the first pass of the GALFIT algorithm, which uses a  $\xi^2$  minimisation method to determine the best fit sérsic index, effective radius, magnitude and position for each of the components. This first pass allows the positions of the components to be determined, which are then fixed as a second pass of the algorithm is run to ensure the correct magnitudes, radii and sérsic indices

---

<sup>2</sup>[http://www.sdss.org/dr12/algorithms/read\\_psf/](http://www.sdss.org/dr12/algorithms/read_psf/)

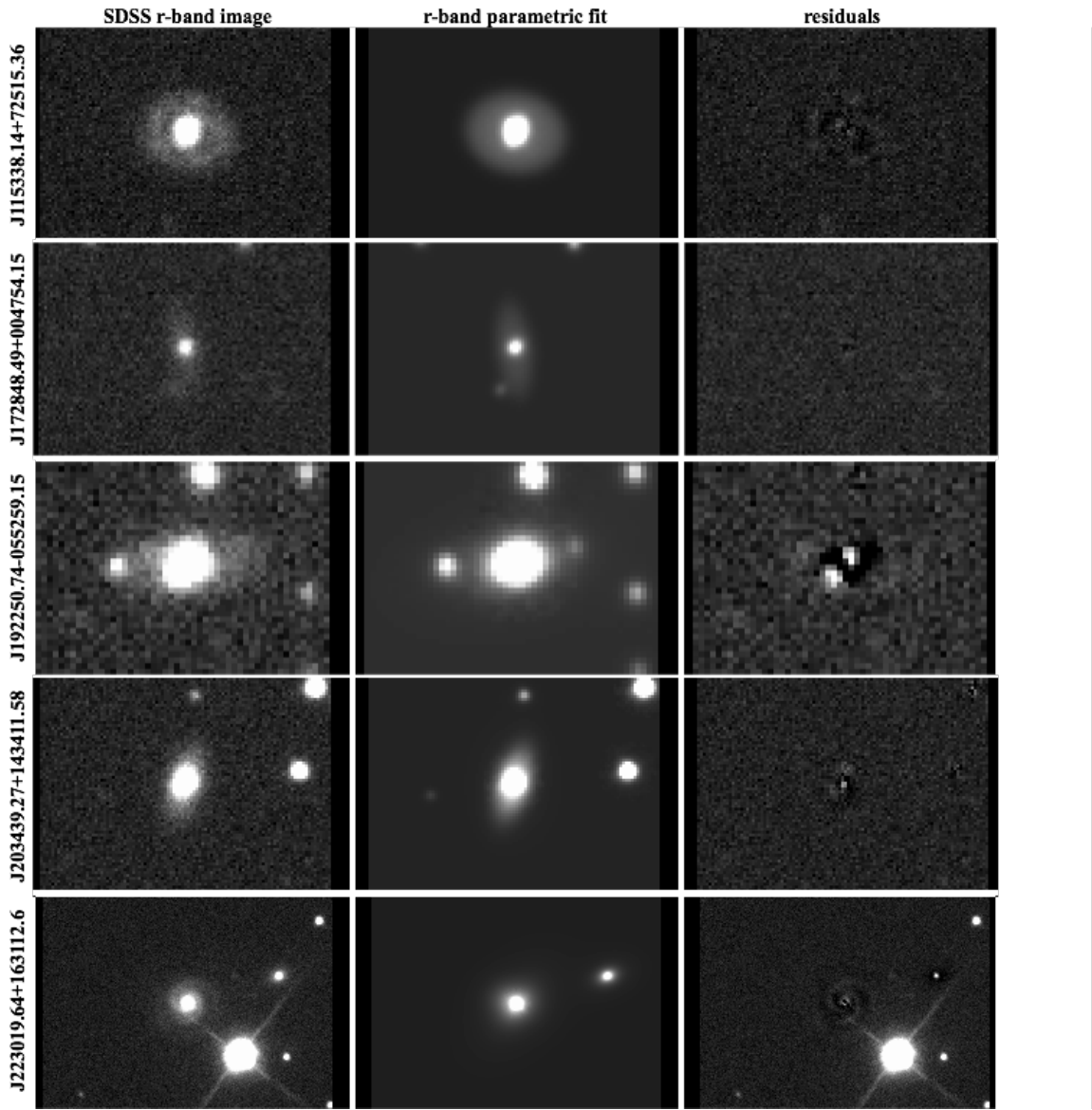


Figure 4.15: SDSS r-band images (left), with the parametric fits from GALFIT (middle) and the residuals (right; with the same scale as the original image) for the 5 galaxies observed with the IDS at the INT. Stable, but uncertain, bulge-to-total ratios were only recovered for the galaxies in the top two rows. In the bottom three rows the nuclear emission was too bright and resolution too low to derive a reliable estimate of the bulge-to-total ratio.

have been fitted. From these models, the GALFIT r band magnitudes of the bulge and disc components were converted to fluxes and the bulge-to-total ratio,  $(B/T)_r$  was calculated as follows:

$$(B/T)_r = \frac{10^{(\frac{m_{r,\text{bulge}}}{-2.5})}}{\left[10^{(\frac{m_{r,\text{bulge}}}{-2.5})} + 10^{(\frac{m_{r,\text{disc}}}{-2.5})}\right]}. \quad (4.6)$$

Stable, but highly uncertain, bulge-to-total ratios were recovered for only 2 of the 5 galaxies (the top two galaxies in Figure 4.15). In the remaining 3 cases the nuclear emission was too bright and the resolution too low for a reliable bulge-to-disc decomposition. Detailed AGN-host fits to the SDSS images in the entire sample are therefore not likely to produce useful measurements of bulge masses. *HST* imaging would enable these measurements, and although currently not available for the galaxies in this sample, observations are currently underway in Cycle 24 (ID: 14606).

Nevertheless, it is possible to constrain the bulge contribution to the host galaxies using existing structural parameters from large-scale studies performing bulge-disc decompositions of SDSS galaxies. While such studies do not account for the presence of an AGN, their tendency to overestimate the bulge-to-total ratio as a result means that bulge masses derived from these quantities may be taken to be conservative upper limits.

Simard et al. (2011) fit multiple models to 1.12 million galaxies in the SDSS catalog to determine best-fit models and structural parameters for each galaxy. Their *r*-band bulge-to-total ratio of the best-fit model is taken as an upper limit to the true bulge-to-total ratio of the DISCDOM sample. To convert limits on bulge luminosities to limits on bulge masses, we assume the mass-to-light ratio of the bulge is equal to the mass-to-light ratio of the disc. This is a reasonable assumption for disc-dominated galaxies, where many of the “bulge” components are likely to be rotationally-supported pseudo-bulges (Kormendy & Kennicutt, 2004) with stellar populations similar to that of the disc (e.g., Graham, 2001).

The upper bulge-to-total limits of the 89 galaxies in the DISCDOM sample which were included in the Simard et al. study, range from  $0.13 \leq (B/\text{Tot})_{\text{max}} \leq 1.0$ , with a mean value of 0.5. Applying these bulge-to-total limits to the stellar masses computed using the colour-luminosity relation (Bell & de Jong, 2001; ?) results in bulge mass upper limits of  $3 \times 10^9 M_\odot < M_{\text{bulge}} < 7 \times 10^{10} M_\odot$ . The distribution of bulge stellar masses for the DISCDOM sample are shown in the middle panel of Figure 4.17

#### 4.2.2.4 Black hole mass estimates

The selection of unobscured AGN facilitates the accurate estimate of black hole masses using a viral assumption. Unobscured AGN have broad emission lines originating from within the black hole sphere of influence; this photoionized broad line region (BLR) can be used as a dynamical tracer of the black hole mass. The viral black hole mass (Peterson, 2014) can be expressed simply as:

$$M_{BH} = f \frac{R \Delta v^2}{G}, \quad (4.7)$$

where  $\Delta v$  is the velocity dispersion of the emitting BLR, which has radius  $R$ , which is assumed to be spherical and the factor,  $f = 0.75$  (?) corrects for this assumption. The velocity dispersion of the BLR can be inferred from the FWHM of a broad line, such as  $H\alpha$  or  $H\beta$  and the radius from the luminosity of the same broad line. This radius-luminosity relationship is calibrated using the more precise black hole mass measurement technique of reverberation mapping (??Barth et al., 2015) in which the radii are measured based on the observed delay between variations in the AGN continuum and the BLR emission (??). Masses derived with this virial method, under these simplifying geometric assumptions, have been shown to be accurate to within a factor of  $\sim 3$  when compared to masses derived using the  $M - \sigma$  method (???, and see Section 4.1.1).

Using the  $M - \sigma$  relation to calculate black hole masses (as in Section 4.1.1) is not possible in this case since I am trying to investigate how these galaxies evolve in comparison to the ‘typical’ AGN host galaxy population used to fit the  $M - \sigma$  relation. Instead I employ the established relation between the black hole mass and the FWHM and luminosity in the broad  $H\alpha$  line defined by Greene & Ho (2007):

$$M_{BH} = (3.0^{+0.6}_{-0.5}) \times 10^6 \left( \frac{L_{H\alpha}}{10^{42} \text{ erg s}^{-1}} \right)^{0.45 \pm 0.03} \left( \frac{\text{FWHM}_{H\alpha}}{10^3 \text{ km s}^{-1}} \right)^{2.06 \pm 0.06} M_\odot, \quad (4.8)$$

with the virial method described above.

To obtain an estimate of the FWHM of the broadened  $H\alpha$  lines, I performed spectral fitting on each of the SDSS and INT spectra described in Section 4.2.1.3 to recover narrow- and broad-line strengths and widths of the  $H\alpha$  6563 Å line, by using **GANDALF** (Sarzi et al., 2006) to fit multiple simultaneous lines as well as the

continuum of the spectra. `GANDALF` is optimised for use with SDSS spectra and so using the program with the INT spectra required minimal data re-formatting. I logarithmically binned and de-redshifted the spectra. From the continuum-subtracted best fit, I determine the FWHM and line flux of the broad and narrow components of the H $\alpha$  line simultaneously, one again employing `emcee`<sup>3</sup>, the Python implementation of a Markov Chain Monte Carlo (MCMC; Mackay, 2003; ?) affine invariant ensemble sampler by Foreman-Mackey et al. (2013) described in Chapter 2.

The uncertainties reported by `emcee` encapsulate the separation of narrow and broad line components in measurement of the FWHM. The reported uncertainties on black hole masses include this source of uncertainty as well as the reported uncertainties in the black hole-broad line relation (Greene & Ho, 2007). There are other sources of uncertainties, such as those involved in implicitly assuming the fixed geometric correction factor,  $f = 0.75$  (?), for each SMBH, the spectral noise, and the error introduced by assuming a Gaussian line profile for all measured broad lines. Determining uncertainties for the last two is outside the scope of this study; based on visual inspection of the line fits, the first is very small compared to the other uncertainties. These fits to the broad and narrow line H $\alpha$  components in the INT spectra are shown in Figure 4.16.

The black hole masses for the 101 galaxies of the DISCDOM sample range from  $10^6 M_\odot \leq M_{\text{BH}} \leq 2 \times 10^9 M_\odot$  and the distribution is shown in the left panel of Figure 4.17 in comparison to those from the QSOCONTROL sample. We compare these black hole masses to galaxy stellar masses and bulge mass upper limits in Section 5.2.

#### 4.2.2.5 Bolometric Luminosities

Bolometric luminosities are calculated from the wavelength-dependent bolometric corrections of Richards et al. (2006) using the conversion from the  $12\mu\text{m}$  infrared luminosities,  $L_{12\mu\text{m}}$ :

$$L_{\text{bol}} \approx 8 \times L_{12\mu\text{m}}. \quad (4.9)$$

The infrared luminosity,  $L_{12\mu\text{m}}$ , is calculated from the WISE W3 magnitudes,  $M_{W3}$ , for which all of the DISCDOM sources have a detection, as follows:

$$L_{12\mu\text{m}} = \left( \frac{4\pi d^2}{10^{-2} \text{ m}^2} \right) \left( \frac{c}{\lambda} \right) \left( \frac{F_{\nu,0}}{1 \times 10^{23} \text{ Jy}} \right) 10^{\left( \frac{M_{W3}}{-2.5} \right)}. \quad (4.10)$$

---

<sup>3</sup>[dan.iel.fm/emcee/](http://dan.iel.fm/emcee/)

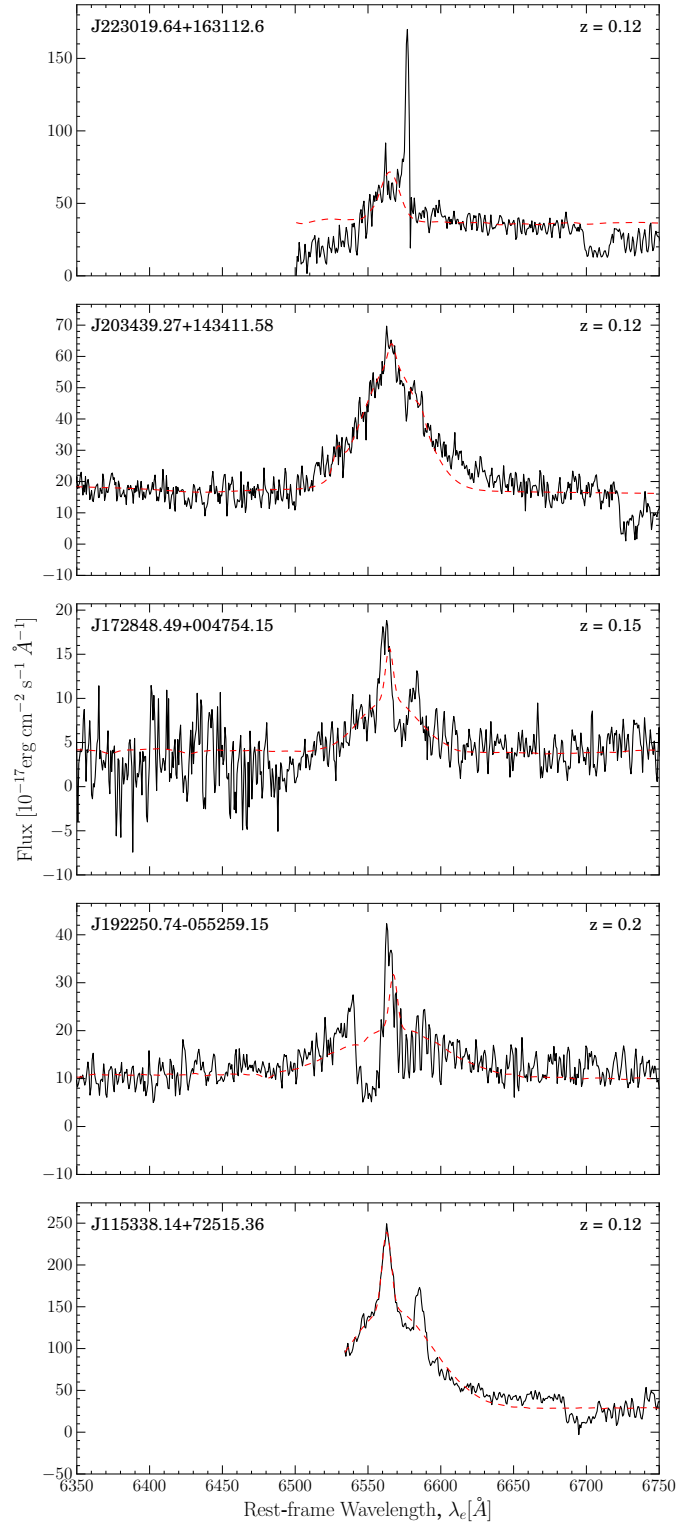


Figure 4.16: Reduced spectra from the IDS on the INT for the 5 galaxies observed with the corresponding measured redshift values shown. Spectra are aligned with the broad  $H\alpha$  emission line, the gaussian fits to which are shown by the dashed red line.

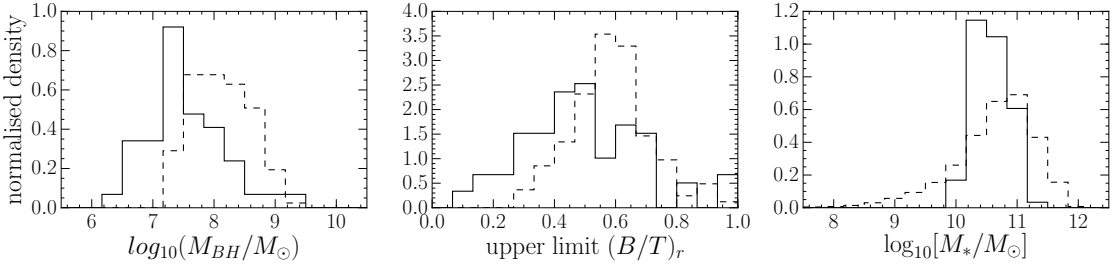


Figure 4.17: Distributions of black hole mass (left), upper limits on the r-band bulge-to-total mass ratio from Simard et al. (2011, middle) and stellar mass (right) of the DISCDOM sample (solid) in comparison to the QSOCONTROL sample (dashed).

The derived bolometric luminosities were then used to calculate Eddington ratios,  $\lambda_{Edd}$ , for the DISCDOM sample using the method outlined in Section 4.1.1, and the black hole mass accretion rate,  $\dot{m}$ , using a simple matter to energy conversion:

$$L = \frac{E}{t} = f \cdot \frac{mc^2}{t}, \quad (4.11)$$

where  $f = 0.15$  (Elvis et al., 2002), is a lower limit on the radiative efficiency factor (i.e. what fraction of the accreted mass can be turned into radiated energy). The black hole mass accretion rate,  $\dot{m}$  can therefore be calculated as:

$$\frac{\dot{m}}{t} = \left( \frac{\dot{m}}{M_\odot \text{ yr}^{-1}} \right) = \left( \frac{1.58 \times 10^{-26}}{f} \right) \left( \frac{\text{cm s}^{-1}}{c} \right)^2 \left( \frac{L_{\text{bol}}}{\text{erg s}^{-1}} \right). \quad (4.12)$$

### 4.2.3 Results

The total stellar mass and estimated bulge masses (see Section 4.2.2.2) are shown against the black hole masses for the DISCDOM sample in Figures 4.18 & 4.19 respectively. I fit a multiple linear regression model to both of these relations using an inference method which encompasses the uncertainties on both  $x$ - and  $y$ -dimensions and the intrinsic scatter in the data. The full method is outlined in Kelly (2007) and is publicly available as a *Python* module LINMIX<sup>4</sup>; a brief outline of the method is provided below.

A multiple linear regression model assumes a simple linear relationship between two independent variables,  $x$  and  $y$ , where both variables are unknown, with added

---

<sup>4</sup><http://linmix.readthedocs.org/>

noise,  $\epsilon$ , from an unknown unobserved random variable. In the LIMMIX package this is modelled with the following form:

$$\eta = \alpha + \beta * x_i + \epsilon \quad (4.13)$$

$$x = x_i + x_{err} \quad (4.14)$$

$$y = \eta + y_{err}. \quad (4.15)$$

Here  $\alpha$  and  $\beta$  are the regression coefficients to be inferred (like  $m$  and  $c$  in a traditional  $y = mx + c$  linear regression),  $x_{err}$  is the error on the measured values  $x_i$ , and  $y_{err}$  is the error on the measured values  $\eta$ .  $\epsilon$  is assumed to be normally-distributed, centred around zero, with a variance  $\sigma^2$ .  $x_{err}$  and  $y_{err}$  are also assumed to be normally-distributed and centred around zero with variances  $\sigma_x^2$  and  $\sigma_y^2$ , respectively and covariance  $xy_{cov}$ . This linear regression method can also incorporate the upper limits on the bulge mass measurements of the 89 SDSS galaxies measured by Simard et al. (2011, see Section 4.2.2.2), which is shown by the solid line in Figure 4.19, by treating them as ‘censored values’ (see Section 7.2 of Kelly, 2007).

Using LINMIX, I also fit to the observations of 30 early-type galaxies from Häring & Rix (2004). Despite the fact that galaxies in the DISCDOM sample are disc dominated and contain either a pseudo-bulge or no bulge, they preferentially lie above the relationship between black hole and bulge stellar mass derived using the bulge dominated galaxies of Häring & Rix (2004), as seen in Figure 4.19.

I consider how the black hole mass compares to the Eddington ratio, or accretion rate, of these disc dominated galaxies and compared with the QSOCONTROL sample in Figure 4.20. The galaxies of the DISCDOM sample have both lower black hole masses and lower bolometric luminosities in comparison to the QSOCONTROL sample, however the Eddington ratio’s are very similar, see Figure 4.21. In fact, the Eddington ratio’s of the redshift matched sample are on average, lower than that for the DISCDOM sample. I can reject the null hypothesis that the disc dominated galaxies are drawn from the same distribution as the QSOCONTROL sample but not for the entire quasar sample of Shen et al. (2011).

Within the QSOCONTROL sample, 108 galaxies were morphologically classified by the Galaxy Zoo 1 project Lintott et al. (2008, 2011), all of which have a debiased combined spiral vote fraction (Galaxy Zoo 1 did not ask whether a galaxy was a disc, therefore we can approximate the combined spiral vote fraction as a disc vote

fraction) of  $p_{CS} < 0.5$  and mean value of  $\langle p_{CS} \rangle = 0.17$ . The QSOCONTROL sample is therefore mainly comprised of bulge dominated galaxies unlike the DISCDOM sample.

Slightly higher accretion rates are therefore occurring in the AGN of the galaxies in the DISCDOM sample than in a bulge dominated QSOCONTROL sample.

The colour magnitude diagram for the DISCDOM sample is also shown in Figure 4.22 in comparison to the SDSS sample and green valley definition from Baldry et al. (2004). The unobscured AGN host galaxies in the DISCDOM sample are found across the entirety of this parameter space, however those with higher black hole mass accretion rates are found preferentially in the green valley and at brighter r-band magnitudes.

#### 4.2.4 Discussion

The large number of purely disk galaxies of the DISCDOM sample hosting growing SMBHs provides a very powerful probe of the simultaneous evolution of galaxies and their black holes driven without typical bulge-forming mechanisms. Despite the rarity of the morphology of these DISCDOM galaxies, they are not found in common areas of black-hole-galaxy scaling relations as seen in Figures 4.18, 4.19 & 4.20 frequented by typical AGN host galaxies of all morphologies (they also lie in the common regions of the local  $M_{BH} - \lambda_{Edd}$  plane shown in Figure 1 of the review paper of ?). Significant black hole growth has occurred up to  $M_{BH} \sim 10^8 - 10^9 M_\odot$  in the DISCDOM sample whilst the disk dominated nature of the galaxy has been preserved. Simulations have repeatedly shown that mergers with mass ratios larger than 1:10 (i.e. mergers where the mass of the satellite is greater than 10% of the main galaxy's mass) will form a classical bulge (???), therefore how is this mass growth possible in the absence of such a major merger dominated (and minor merger limited) formation history?

Using Equation 4.12 and given the bolometric luminosities of the DISCDOM sample, the black hole mass accretion rates can be estimated to lie in the range  $0.01 \leq \dot{m} \geq 0.37 M_\odot \text{ yr}^{-1}$ . Simulations by ? and more recently by (?) show that such accretion rates are completely achievable by cold accretion of minor satellites with mass ratios less than 1:10 (i.e. the mass of the satellite galaxy is less than 10% of the main galaxy mass). However, there is also evidence that such accretion rates may also be possible via merger free, secular processes alone. One such secular process, is bar

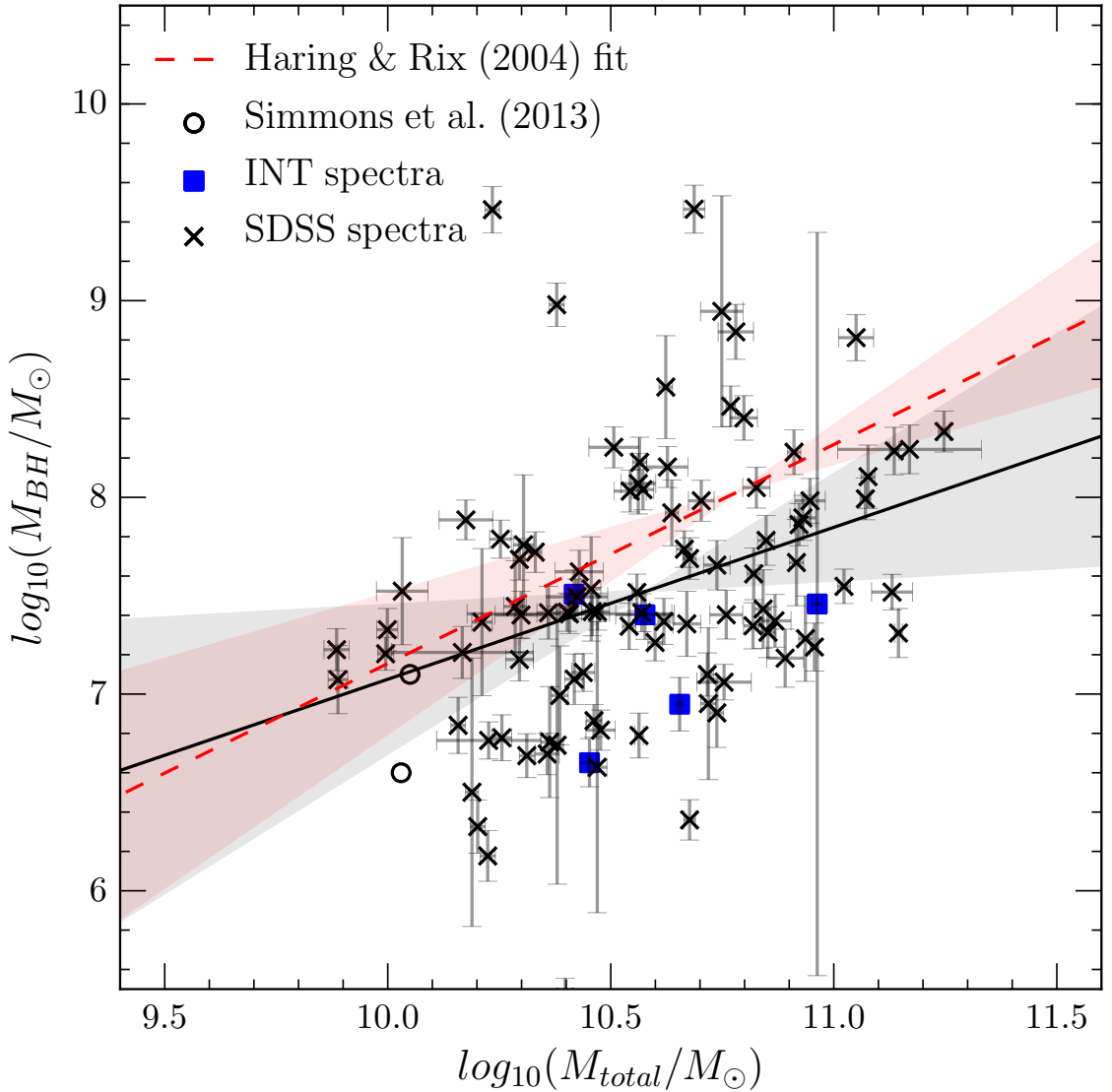


Figure 4.18: Total stellar mass against the black hole mass of the 101 galaxies, including those observed by SDSS (crosses), with the IDS on INT (blue squares) and detections from Simmons et al. (2013, open circles). The best fit line to the data points and two-dimensional errors from linear regression is shown (solid line) with  $\pm 3\sigma$  (grey shaded). I also show the best fit found using this same method to the early-type galaxies of Häring & Rix (2004) (dashed line) with  $\pm 3\sigma$  (red shaded) and the measured values shown by the red circles. Despite the fact that these galaxies are predominantly disc dominated they are found in the same region of parameter space as the bulge dominated systems used to derive the Häring & Rix (2004) relationship (see discussion in Section 4.2.4).

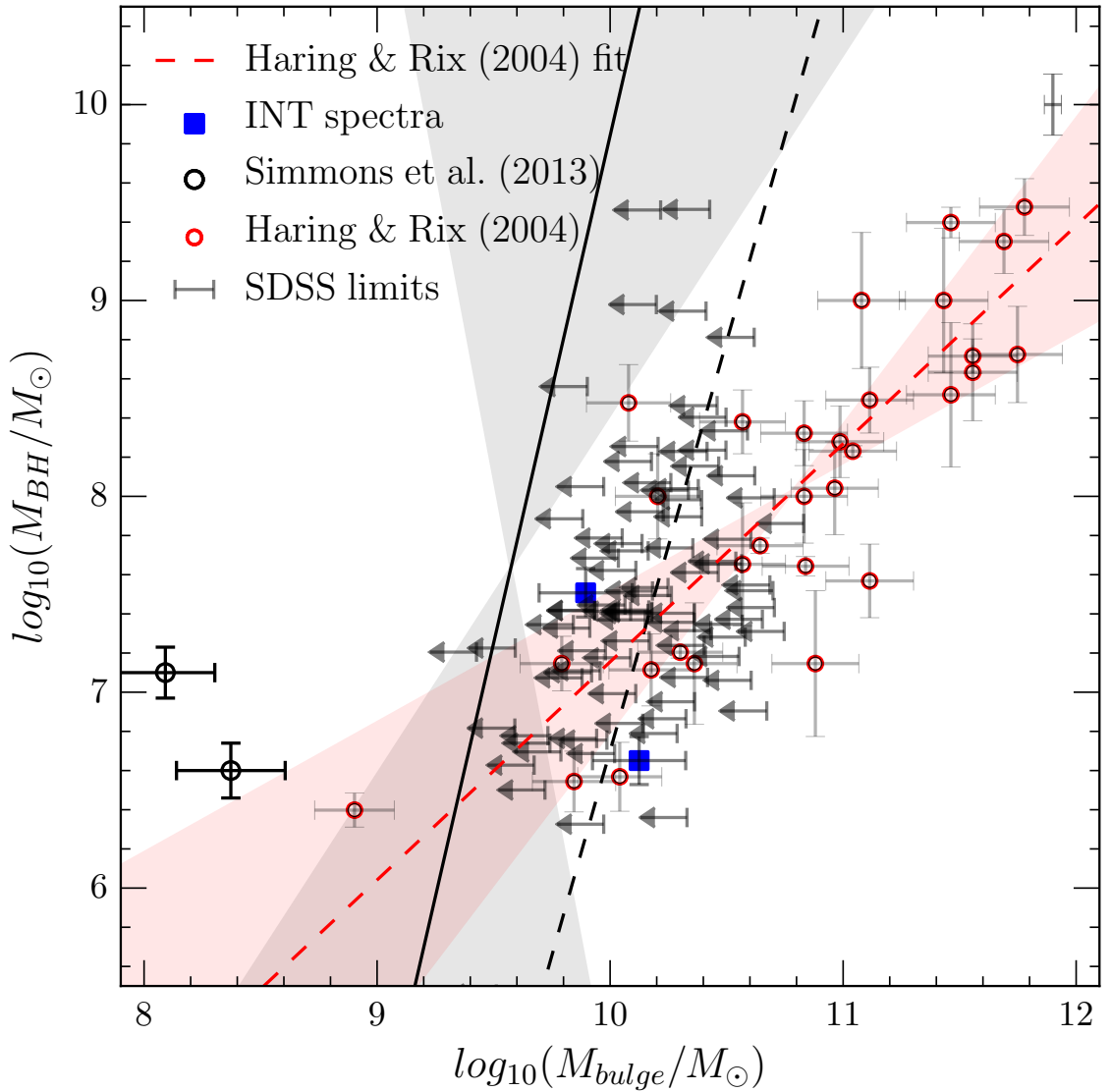


Figure 4.19: The upper limits on the calculated bulge masses are plotted against the black hole mass with the best fit to these upper limits and two-dimensional errors using linear regression methods (solid line) shown with  $\pm 3\sigma$  (grey shaded). The dashed line shows the fit if the upper limits are not treated as such. I also show the best fit found using this same method to the early-type galaxies of Häring & Rix (2004) (dashed line) with  $\pm 3\sigma$  (red shaded) and the measured values shown by the red circles. Despite the fact that these galaxies are predominantly disc dominated they will are most likely to lie above the Häring & Rix (2004) relationship found for bulge dominated systems (see discussion in Section 4.2.4).

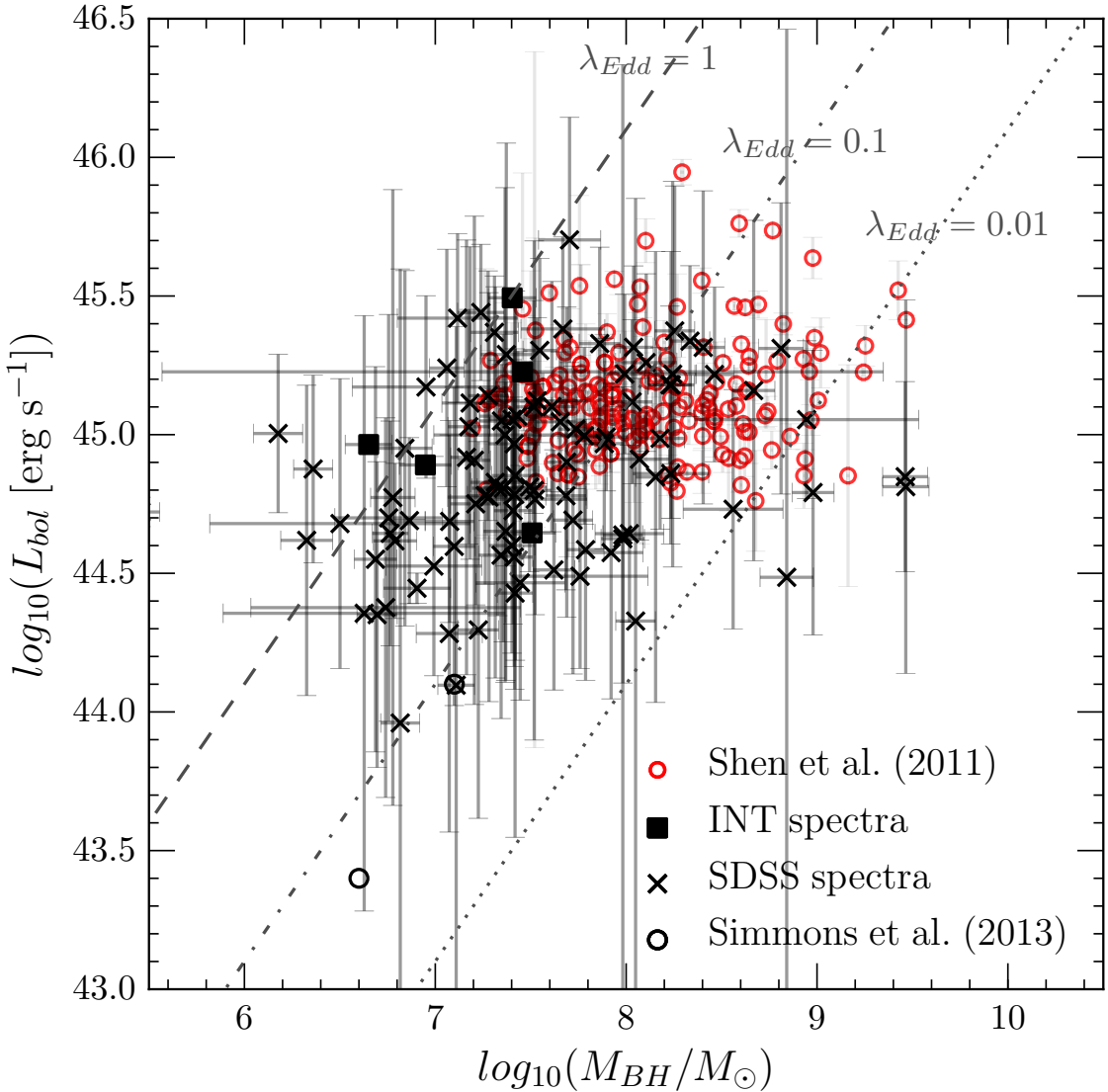


Figure 4.20: Black hole mass against bolometric luminosity for the 101 galaxies, including those observed by SDSS (crosses) and with the IDS on INT (squares). We also show detections from Simmons et al. (2013) (open circles) and those from the redshift matched sample of Shen et al. (2011). For reference we show lines of example Eddington ratios of  $\Lambda_{Edd} = 1$  (dashed),  $\Lambda_{Edd} = 0.1$  (dot-dashed) and  $\Lambda_{Edd} = 0.01$  (dotted).

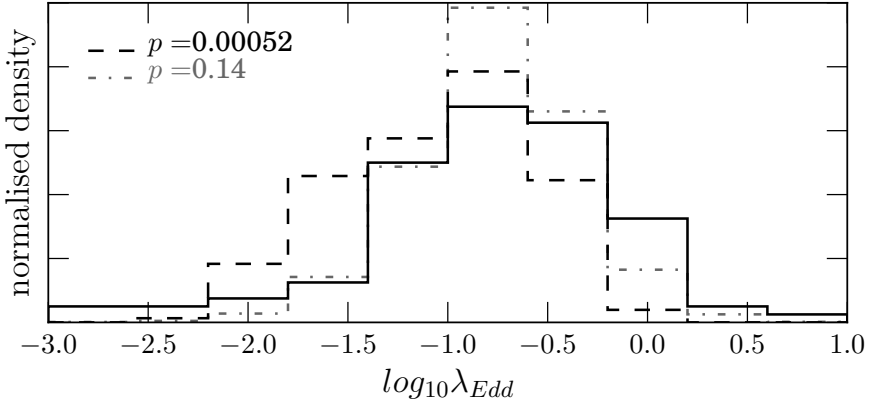


Figure 4.21: Normalised distributions of logarithmic Eddington ratio for the sample of 101 disc dominated galaxies (solid line), compared with that for the redshift matched sample from Shen et al. (2011; dashed line) and the entire sample (dot-dashed line). We also provide the p-values of a 2 sample KS test between the disc dominated sample and each of the quasar samples. We reject the null hypothesis that the two samples are drawn from the same population for the redshift matched quasar sample but accept the null hypothesis for the entire quasar sample of Shen et al. (2011).

driven gas inflow into the central regions of galaxies. Simulations of barred galaxies have repeatedly shown that gas inflow rates due to a morphological bar range from  $0.1 - \text{few } M_{\odot} \text{ yr}^{-1}$  (?????) and may increase to up to  $\sim 7 M_{\odot} \text{ yr}^{-1}$  (?) with increasing bar length, bar strength and axis ratio. These simulations do struggle to show that this gas which is funnelled to the central regions of the galaxy is indeed accreted into the central few parsecs, often accumulating in a nuclear ring and causing a starburst (?). Similarly, no observational correlation has yet been found between the presence of a bar and that of an AGN either locally (?????) or out to  $z \sim 1$  (?). I estimate a bar fraction in this sample (which is by no means complete), by visual inspection of the SDSS images (see Figure 4.10), of  $f_{\text{bar}} \sim 0.42$ ; this is a lower limit due to the edge on nature of some of the galaxies in the DISCDOM sample.

Using these calculated black hole mass accretion rates, the time required to grow the black holes in the DISKDOM sample from a seed mass of  $10^2 M_{\odot}$  can be derived. This calculation assumes that the black holes have grown at the bolometric luminosity currently observed since the mass at which that luminosity was the Eddington luminosity and prior to this underwent Eddington limited growth. This means that the accretion rates,  $\dot{m}$ , calculated will be the maximum rates at which the black holes

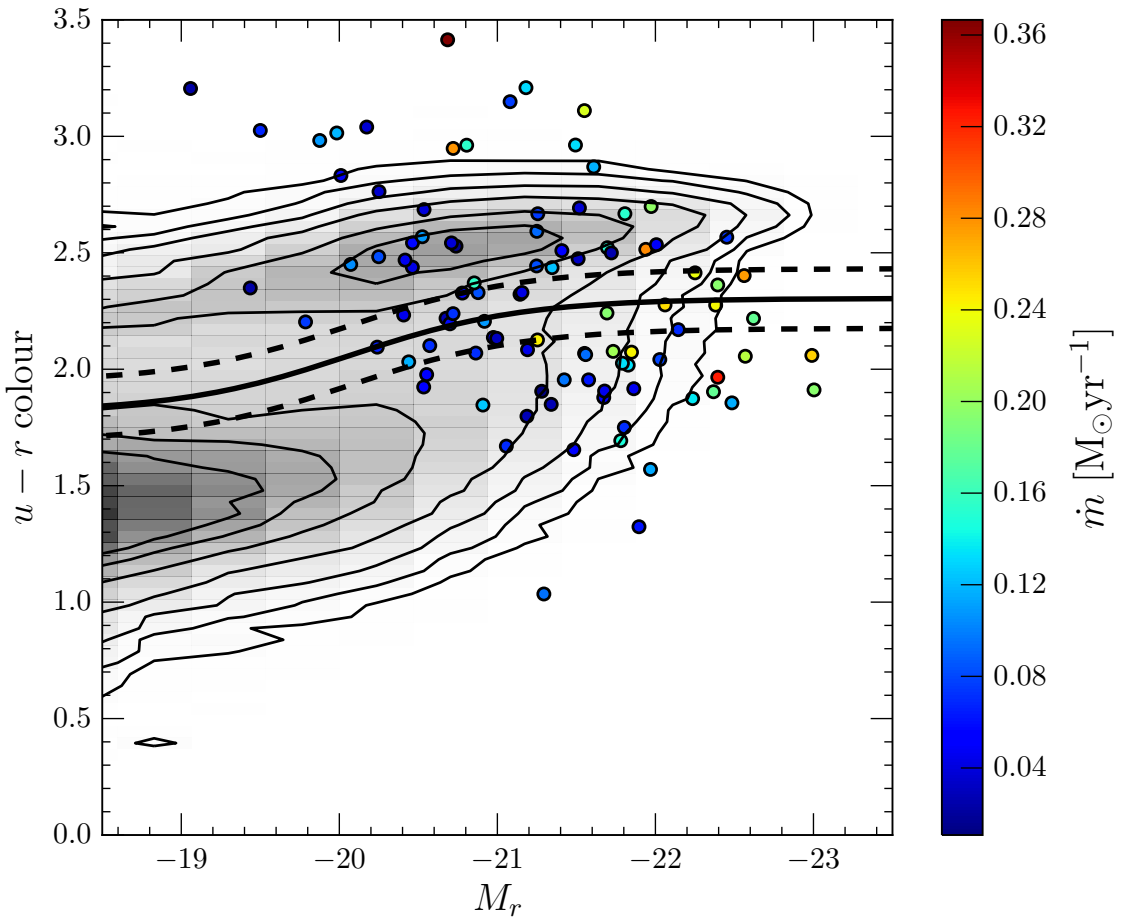


Figure 4.22: Optical colour-magnitude diagram showing the positions of the DISCDOM sample (circles) in comparison to the SDSS DR7 sample from Baldry et al. (2004). The galaxies of the DISCDOM sample are coloured by their black hole mass accretion rate,  $\dot{m}$  (see Equation 4.12). The definition between the blue cloud and red sequence from Baldry et al. (2004) is shown by the solid line (as defined in Equation 3.1) with  $\pm 1\sigma$  shown by the dashed lines. The DISCDOM sample are found across the colour magnitude diagram, however those with higher mass accretion rates are found preferentially in the green valley and at brighter r-band magnitudes.

have grown over their lifetimes. This is a conservative assumption but gives an estimate of the total time these black holes would need to spend in actively growing phase if the calculated rates are typical of black holes residing in disk dominated host galaxies. The mean (median) time taken for the black holes of the DISCDOM sample to grow from a seed black hole mass is  $\sim 1.68\text{Gyr}$  ( $\sim 0.37$  Gyr), with a range of times from  $\sim 0.005 - 38$  Gyr. A time of  $\sim 38$  Gyr was calculated for two of the most massive black holes in the DISCDOM sample, with very low current Eddington ratios (see Figure 4.20). Since this time frame is beyond the calculated age of the Universe () we can assume that this value is an overestimate of the time taken to grow these black holes. Since AGN are believed to go through a duty cycle of varying accretion rates (????), then we can assume that these two black holes were accreting at a higher rate at some point in their history. If these two black holes are assumed to grow within the median (mean) time derived for the rest of the DISCDOM sample, then the past accretion rate will have been on the order,  $\dot{m} \sim 7.95$  ( $1.73$ ) $M_{\odot}\text{ yr}^{-1}$ . As discussed earlier, similar gas inflow rates due to the presence of a bar have been simulated (??). The two host galaxies are at too high a redshift however to allow the detection of a morphological bar in the SDSS image.

The black hole mass accretion rates are shown in Figure 4.22, wherein the locations of the DISCDOM sample on the optical colour magnitude diagram are shaded by  $\dot{m}$ . Those hosts with higher black hole mass accretion rates are found preferentially in the green valley and at brighter r-band magnitudes. This once again supports the arguments of Section 4.1 that feedback from AGN could cause galaxies to quench and therefore transition through the green valley after a sustained period of high mass accretion.

Since the disc galaxies in this sample have different dynamical histories to bulge dominated galaxies, their black hole masses are not expected to correlate in the same way to their stellar masses if different dynamical histories lead to different mechanisms for black hole growth. However, Figure 4.18 shows how the black hole and total stellar masses of the DISCDOM sample occupy the same region of parameter space as the bulge dominated elliptical galaxies used to derive the Häring & Rix (2004) relationship. Similarly Figure 4.19 shows how the black hole masses of the DISKDOM sample (which contain either no bulge, or a possible small pseudo bulge) lie well above the Häring & Rix (2004) relationship, particularly when the upper limits on DISCDOM bulge masses are taken into account. In other words, given what we know about black hole growth mechanisms, the black holes in these disk dominated systems

are  $\sim 1 - 2$  dex more massive than they should be, given the mass (or lack thereof) of their bulge component.

This is in agreement with the results of Simmons et al. (2013) who found a similar excess in the black hole masses of  $\sim 1.5$  dex and  $\sim 2$  dex for the two measured black hole masses in their sample of 13 purely disk galaxies. Both this result and the results shown in Figures 4.18 & 4.19 at first seem to be in contradiction with previous works which find that galaxies with pseudo-bulges have lower black hole masses than predicted by the typical scaling relation (see work by ??Jiang et al., 2011; ?; ?). However, all these studies are biased by their sample selection methods, first selecting based on black hole mass to produce a sample of low mass black holes ( $M_{BH} < 10^6 M_\odot$ ) within which they hoped to find bulgeless or pseudo-bulge morphologies. With the larger sample shown in Figure 4.19, we can see that the fitted relationship between the black hole mass and the upper limits of the measured bulge masses of the DISCDOM sample (solid black line), intersects with that of the elliptical sample of Häring & Rix (2004) at  $M_{BH} \sim 10^{6.4} M_\odot$ . At this point, the relationship predicts that for disk dominated galaxies the black hole masses will indeed be less than those predicted for bulge dominated systems, as concluded by the studies referenced above.

Splitting the AGN host population by morphology in this way however, also leads to a biased conclusion. As discussed in Chapter 3, the strength of the POPSTARPY method lies partly due to the fact that no thresholds are applied to the GZ morphological vote fractions, allowing the dominance of intermediate quenching rates across the colour magnitude to be revealed (see Section 3.2). Similarly, if one does not *discriminate* against morphology and a linear regression fit is made to all galaxies in the DISCDOM sample (with proper consideration of upper limits) along with those from Häring & Rix (2004) and Simmons et al. (2013), the result is an almost vertical line in the bulge-black hole mass plane. This suggests that there is perhaps no intrinsic correlation between black hole mass and galaxy bulge mass across the full morphological spectrum of galaxies.

This argument is supported by the agreement between the relationships between the total stellar and black hole mass for the DISCDOM and Häring & Rix (2004) samples shown in Figure 4.18. This agreement arises despite the two extremes in galaxy formation histories. This indicates that the mechanisms driving the dynamical and morphological structure of the galaxy may not be fundamental to the growth of the black hole. The black hole-galaxy relations observed in the  $M_{BH}-\sigma$ ,  $M_{BH}-M_{\text{bulge}}$

and  $M_{BH}$ - $M_*$  planes although demonstrating a correlation, have never implied a *causation*. All of these parameters however, share mutual correlations to the overall gravitational potential of the dark matter halo of the galaxy (??), suggesting the true cause of the black-hole galaxy scaling relations is an outcome of hierarchical galaxy evolution Jahnke & Macciò (2011) regardless of merger history of the galaxy.

This once again supports the arguments of Section 4.1 that feedback from AGN could cause galaxies to quench and therefore transition through the green valley after a sustained period of high mass accretion.

### 4.3 Conclusions

# Chapter 5

## The influence of the group environment

### 5.1 Group Identification

We used the Berlind et al. (2006) catalogue, which uses a friends-of-friends algorithm to identify group and cluster galaxies in the SDSS. This was cross matched to the GZ-GALEX sample and limited to  $z < 0.1$  to ensure GALEX completeness of the red sequence (see ?). Centrals were selected as the brightest galaxy in a group and all others were designated as satellites. This resulted in a sample of 14,199 group galaxies with 3,468 centrals and 10,731 satellites within a projected cluster centric radius range of  $0 < R/R_{200} < 25$  and  $z < 0.084$ .

In this work we focus on galaxies which are either quenching or quenched and are more than  $\pm 1\sigma$  below the star forming ‘main sequence’. This encompasses 4629 satellite and 2314 central galaxies and will be referred to as the GZ-GROUP sample. These galaxies are highlighted in red on Figure ??.

#### 5.1.1 Field sample

For all galaxies in the GZ-GALEX sample, we calculated the smallest projected cluster centric radii from each of the central galaxies in the Berlind et al. (2006) catalog and selected candidate field galaxies as those with (i)  $R/R_{200} > 25$  and (ii)  $\log \Sigma < -0.8$

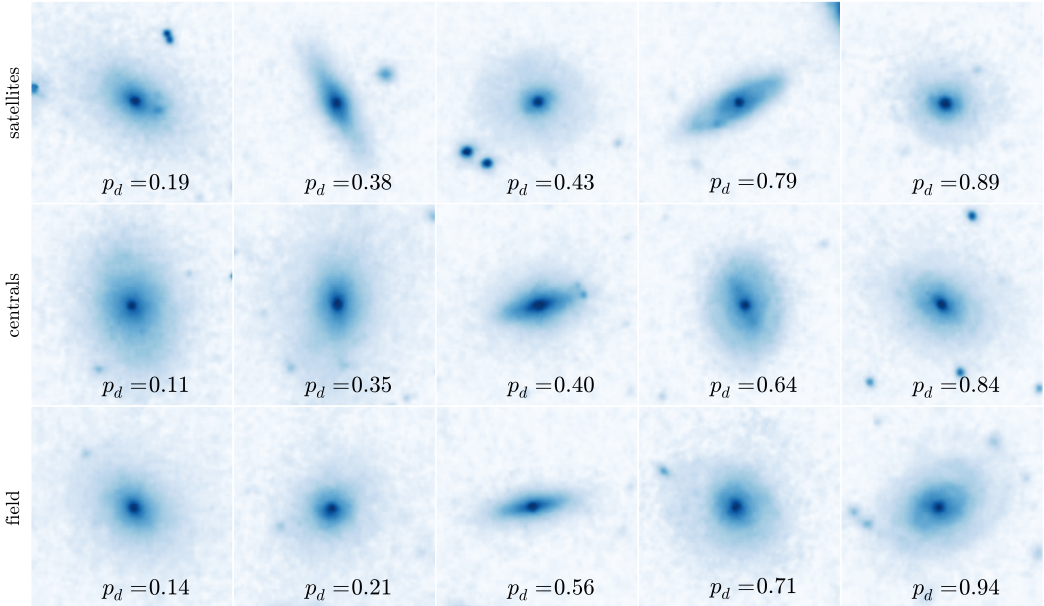


Figure 5.1: Randomly selected SDSS *gri* composite images of satellite and central galaxies in the GZ-GROUP sample in comparison to those from the GZ-FIELD sample. All galaxies lie within  $0.04 < z < 0.05$  and in the central galaxy mass range  $10^{10.5} < M_*(M_\odot) < 10^{11}$ , used as a proxy for halo mass. The galaxies are ordered from least to most featured according to their debiased ‘disc or featured’ vote fraction,  $p_d$  (see Willett et al. 2013). The scale for each image is 0.099 arcsec/pixel.

from ?. This sample of field galaxy candidates was then matched in redshift and stellar mass firstly to the central galaxies of the GZ-GROUP sample to give 2,309 field galaxies with  $z < 0.084$  which will be referred to as the GZ-CENT-FIELD sample. Secondly, the field galaxy candidates were then matched in redshift and stellar mass to the satellite galaxies of the GZ-GROUP sample to give 6,849 field galaxies with  $z < 0.084$  which will be referred to as the GZ-SAT-FIELD. These galaxies in the GZ-SAT-FIELD sample will be used as a control when investigating the morphological trends of satellite galaxies with environment.

As in Section 5.1 we select all those galaxies in the central matched sample  $\pm 1\sigma$  below the star forming ‘main sequence’, giving 1596 quenching or quenched field galaxies for use as a control sample, which will be referred to as the GZ-CENT-FIELD-Q sample. These galaxies will be used as a control when investigating the quenching parameters of the different environments in order to ensure that each galaxy under comparison resides in similar stellar mass halos.

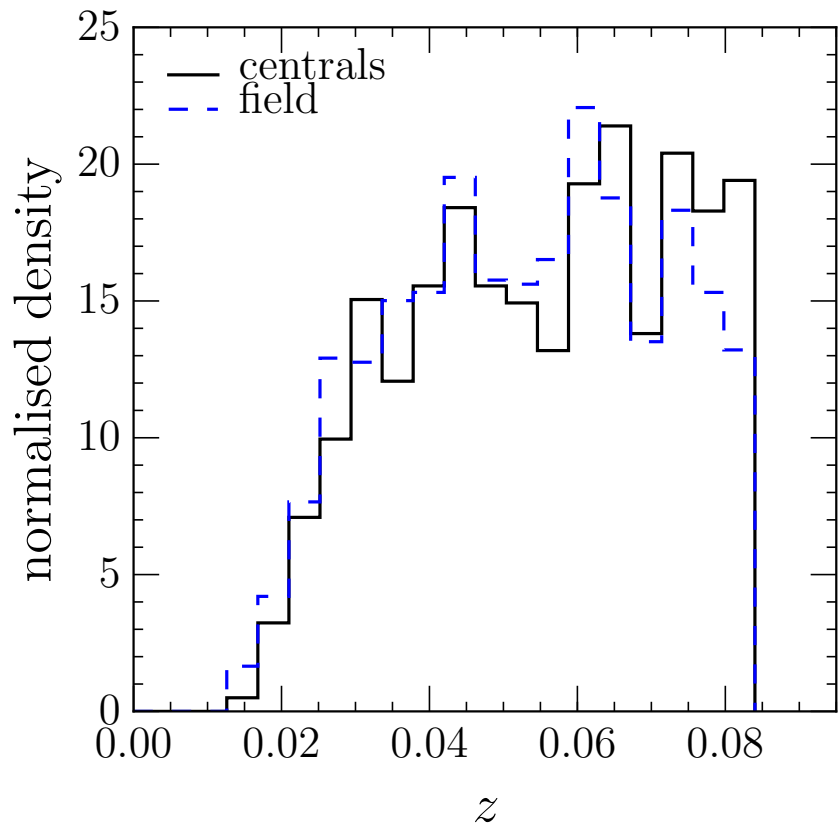


Figure 5.2: Redshift distributions of quenching or quenched central galaxies in the GZ-GROUP sample (black solid line) in comparison to the redshift and mass matched GZ-CENT-FIELD-Q sample (blue dashed line).

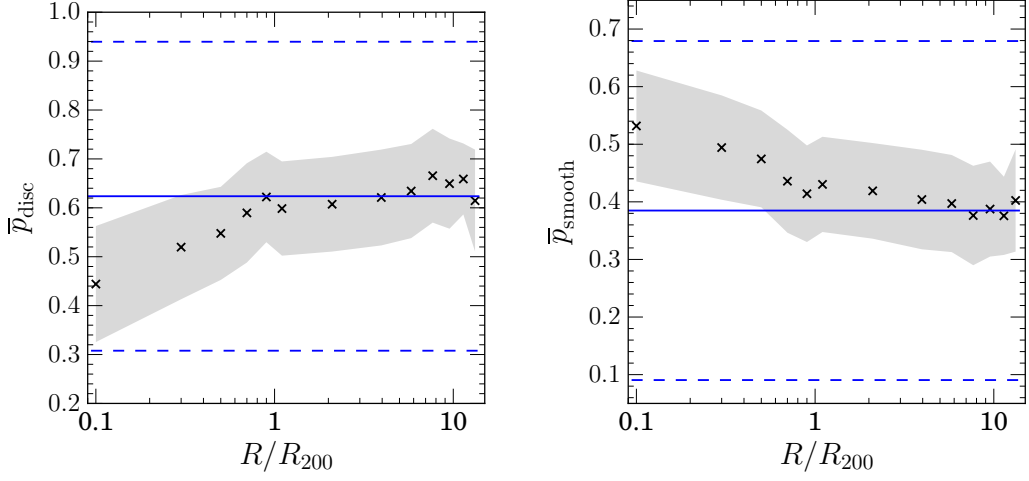


Figure 5.3: Mean GZ vote fraction for disc (top) and smooth (bottom) galaxies in the GZ-GROUP sample binned in projected cluster centric radius, normalised by  $R_{200}$ , a proxy for the virial radius of a group. The shaded region shows  $\pm 1\sigma$  on the mean vote fraction. The mean vote fraction of the FIELD sample are also shown (blue solid lines) with  $\pm 1\sigma$  (blue dashed lines).

## 5.2 Results

With the output from STARPY we can also study the time since quenching onset ( $\Delta t = t_{obs} - t_q$ , see Section ??) binned in projected cluster centric radius, normalised by  $R_{200}$  (a proxy for virial radius) for satellite galaxies and central galaxies in the GZ2-GROUP sample, compared with galaxies in the GZ2-FIELD sample. We can investigate these trends with group properties as shown in Figures 5.8 & 5.9.

Across all the panels in Figures 5.8 & 5.9 we see a general trend for increasing time since quenching onset with decreasing distance from the group centre, which is suggestive that this trend is due to an environmental quenching mechanism. As earlier, in Figures 5.3–5.6 significant differences from the field value arise inside  $\sim$  one virial radius.

If mergers are an important evolutionary mechanism for satellite galaxies as the morphological evidence in Figures 5.2 & 5.6 suggests, we would expect to see a difference in the quenching histories of satellites in groups with a higher number of galaxies,  $N_{group}$ . However, the bottom panel of Figure 5.8 shows that there is no trend with time since quenching onset with increasing  $N_{group}$  for the satellite galaxies. The cen-

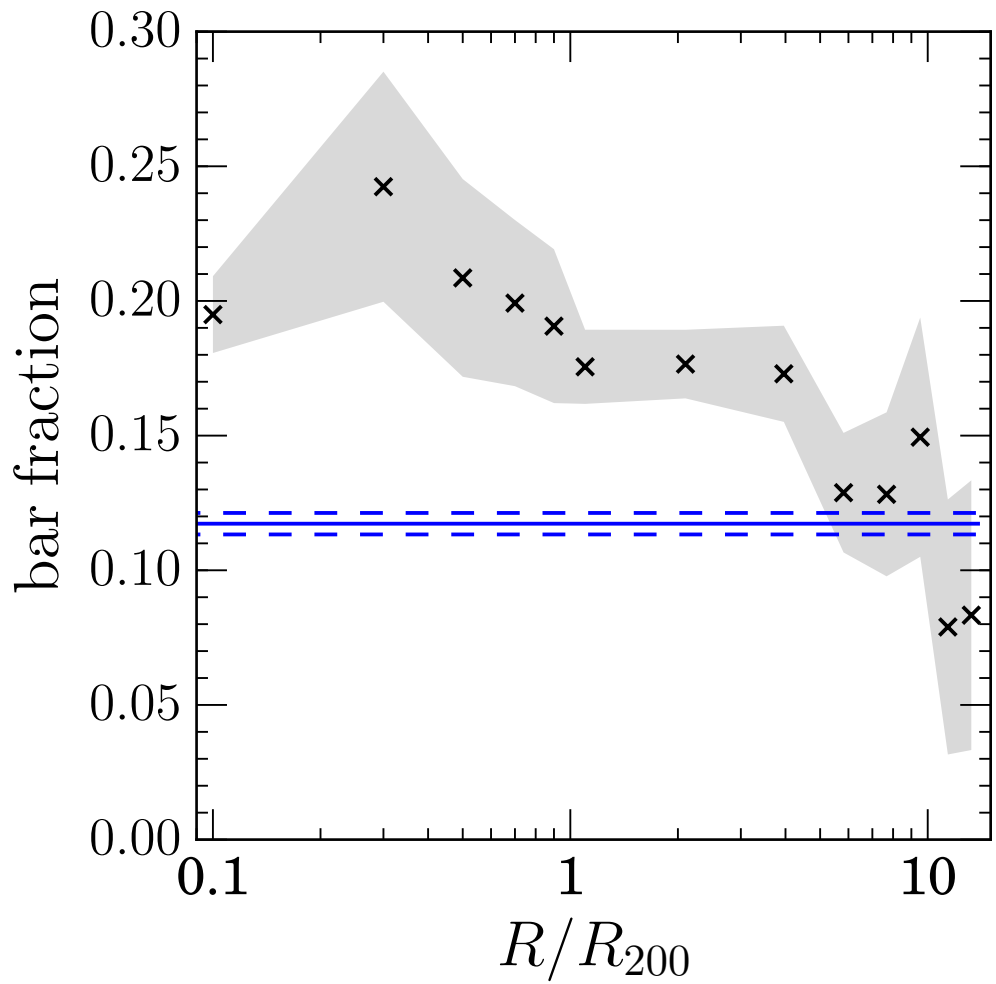


Figure 5.4: Bar fraction (number of barred disc galaxies over number of disc galaxies) in the GZ-GROUP sample binned in projected cluster centric radius, normalised by  $R_{200}$ , a proxy for the virial radius of a group. The shaded region shows  $\pm 1\sigma$  on the bar fraction. The bar fraction of the GZ-SAT-FIELD sample is also shown (blue solid line) with  $\pm 1\sigma$  (blue dashed line).

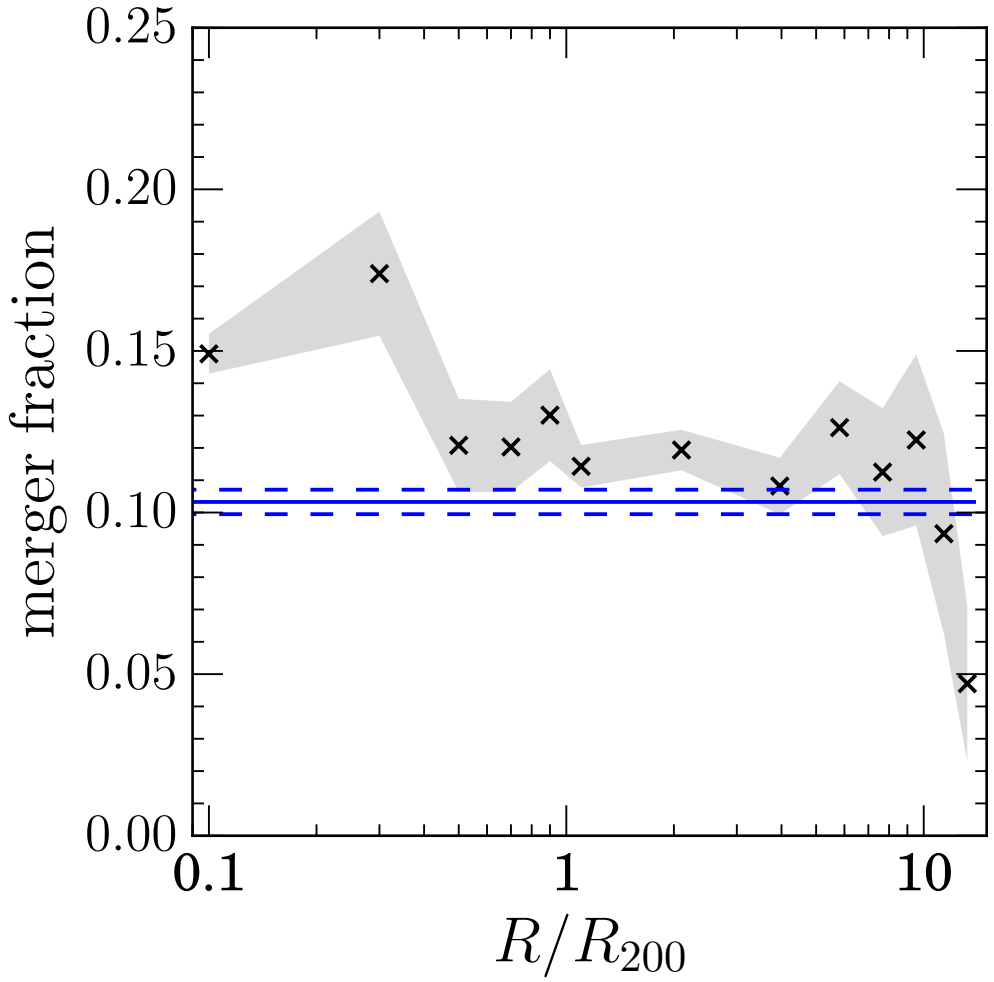


Figure 5.5: Merger fraction in the GZ-GROUP sample binned in projected cluster centric radius, normalised by  $R_{200}$ , a proxy for the virial radius of a group. The shaded region shows  $\pm 1\sigma$  on the merger fraction. The merger fraction of the GZ-SAT-FIELD sample is also shown (blue solid line) with  $\pm 1\sigma$  (blue dashed line).

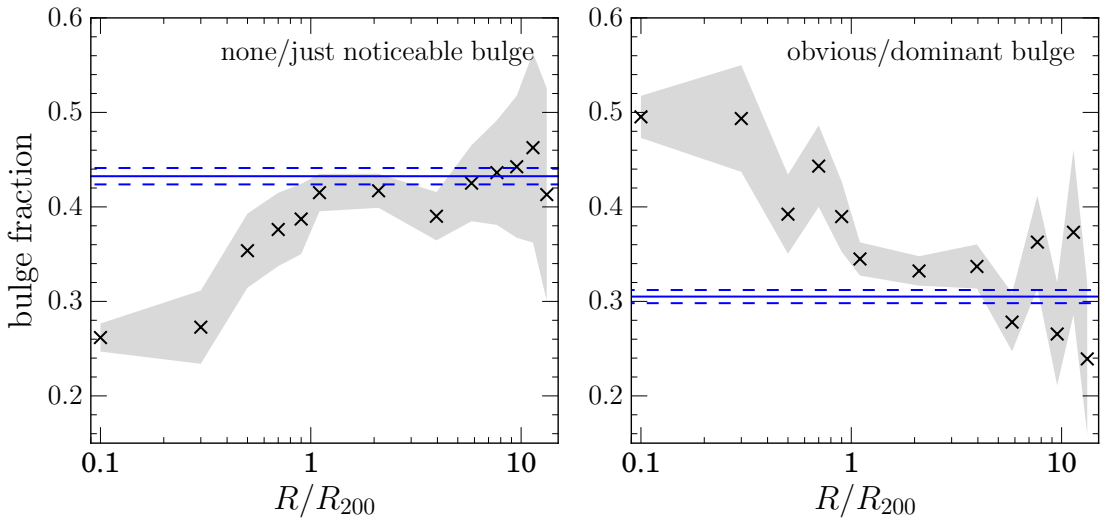


Figure 5.6: Fraction of galaxies with none/just noticeable bulge classifications (left) and with obvious/dominant bulge classifications (right) in the GZ-GROUP sample binned in projected cluster centric radius, normalised by  $R_{200}$ , a proxy for the virial radius of a group. The shaded regions shows  $\pm 1\sigma$  on the bulge fractions. The bulge fractions of the GZ-SAT-FIELD sample are also shown (blue solid lines) with  $\pm 1\sigma$  (blue dashed lines).

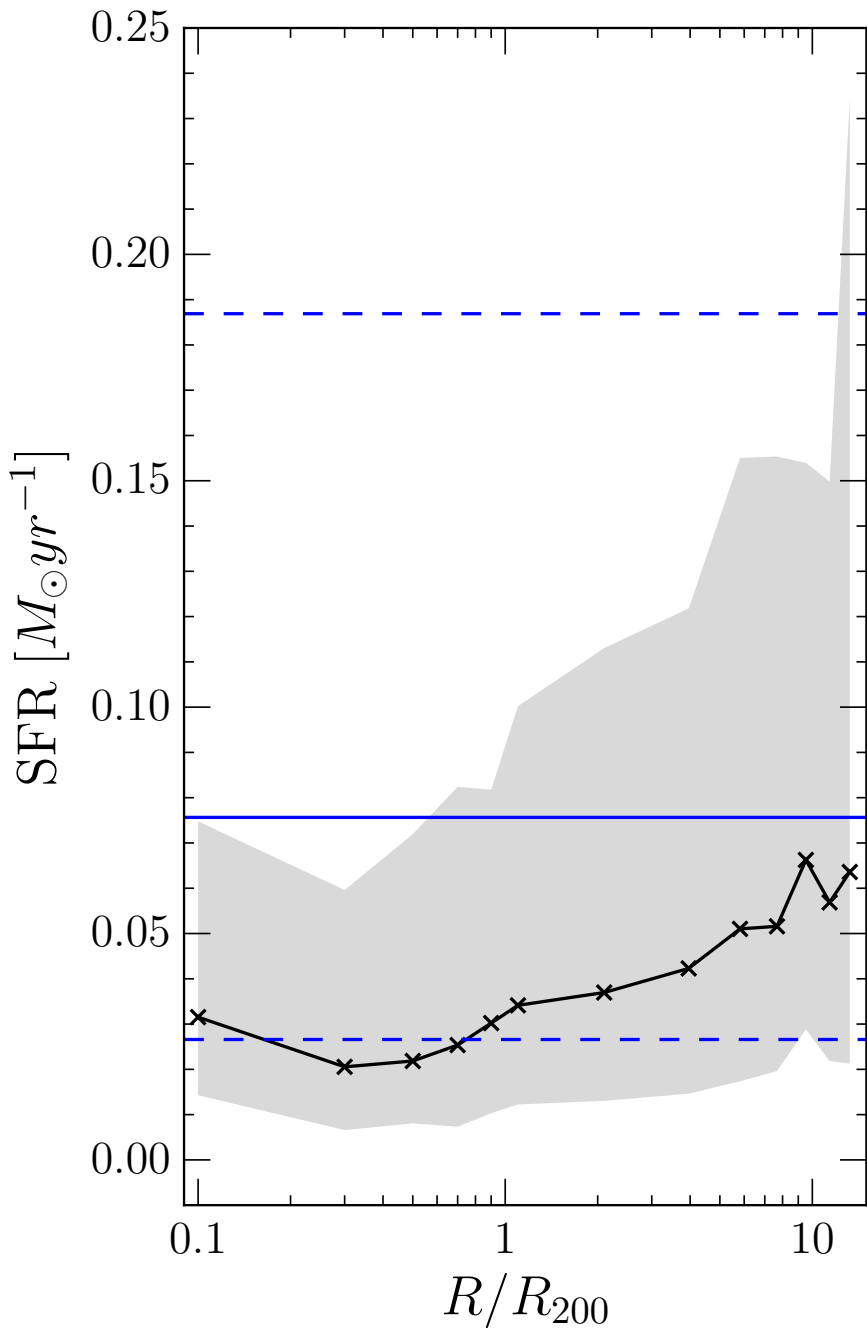


Figure 5.7: Median  $H\alpha$  derived star formation rates of satellite galaxies in the GZ-GROUP sample, binned in projected cluster centric radius, normalised by  $R_{200}$ , a proxy for the virial radius of a group. The shaded region shows the SFRs encompassed by 50% of the population in a given bin. The median SFR of the GZ-SAT-FIELD sample is shown (blue solid line) along with the 25th and 75th percentiles (blue dashed lines).

tral galaxies (shown by the square points at  $\sim 0.01R/R_{200}$ ) however, do show a trend for increasing time since quenching with  $N_{group}$ . Suggesting that mergers are not the dominant quenching mechanism for satellite galaxies but are for centrals.

In the middle panel of Figure 5.8 the satellite galaxies of the GZ2-GROUP sample are now split by their stellar mass (calculated from the absolute r-band magnitude and  $u - r$  colour by the method outlined in ?) and we do see a clear trend for increasing time since quenching onset with increasing stellar mass for both satellite and central galaxies. This is suggestive of mass quenching among the group galaxy population. This is contrary to previous work suggesting that mass quenching is only of import for central galaxies (???). Interestingly, the inner satellites of a given mass have quenched less recently than the centrals at the same mass range, suggesting some episode of more recent star formation may have occurred in the central galaxies but not in the inner satellites. This is once again suggestive of a merger dominated evolutionary history for central galaxies, with mergers postulated to cause a burst of star formation before then quenching the remnant galaxy (??Pontzen et al., 2016).

In simulations, the three things that are found to most constrain galaxy evolution are redshift, mass and halo mass ???. To study the effect that halo mass has on the quenching properties of group galaxies we shall use a proxy for halo mass by splitting by the GZ2-GROUP sample by the stellar mass of the corresponding central galaxy of a group.

This is shown in the top panel of Figure 5.8 where we can once again see a clear trend for increasing time since quenching onset with increasing stellar mass of the group central for both satellite and central galaxies. More massive halos therefore have a greater impact on the star formation histories of their satellites than less massive halos. This is often though to be attributed to hotter inter galactic medium (IGM) temperatures in higher mass halos which can then impact on a galaxy through ram pressure stripping (RPS) of gas for star formation. If RPS is indeed a dominant environmental quenching mechanism we should therefore see a trend in  $\Delta t$  with the speed of a satellite galaxy relative to the group central. In the bottom panel of Figure 5.9 we split the satellite galaxies of the GZ2-GROUP sample into bins of relative velocity to their central galaxies. We can see that there is no trend with time since onset of quenching with increasing relative velocity for satellite galaxies, however the trend with decreasing projected group centric radius, seen in each panel in Figure 5.8

is still present. This suggests that any environmental processes causing this quenching are not corrected with satellite velocity and therefore RPS is not the dominant environmental quenching mechanism, in support of the conclusions of (?).

We can also account for both the stellar mass and the halo mass of the central galaxy simultaneously by considering the stellar mass ratio of the satellite to its central galaxy,  $\mu_* = M_*/M_{*,c}$ , once again using the stellar mass of the central galaxy as a proxy for halo mass. In the middle panel of Figure 5.9 we show the time since quenching of the GZ2-GROUP sample with projected cluster centric radius split into bins of  $\mu_*$ . The change in  $\Delta t$  with projected cluster centric radius occurs more steeply (particularly beyond  $\sim$  a virial radius) for satellite galaxies with much smaller masses than their group central ( $-2.0 < \log_{10} \mu_* < -1.0$ , shown by the blue curve). Since the stellar mass of the central galaxy is correlated with the halo mass and therefore the potential of the system, this suggests that smaller mass galaxies in larger halos are most effected by environmental effects, therefore the dominant environmental quenching mechanism must be correlated with the group potential.

Previous studies have claimed that the property which correlates most with whether a galaxy is quenched is the stellar velocity dispersion,  $\sigma_*$ . Shown in the top panel of Figure 5.9 is the time since quenching of the GZ2-GROUP sample with projected cluster centric radius split into bins of  $\sigma_*$ . Along with the stellar mass (shown in the middle panel of Figure 5.8), the stellar velocity dispersion shows the largest trend in  $\Delta t$  for satellite galaxies, with galaxies with the smallest (largest) stellar velocity dispersions have quenched more (less) recently.

### 5.3 Discussion

Across all panels of Figures 5.8-5.9 a trend for increasing time since quenching onset with decreasing projected cluster centric radius was present. This suggests that the environment does directly cause quenching; galaxies closer in, fell into the group earlier and as they did so they started to quench giving rise to a larger  $\Delta t$ . However, as seen in Figure 5.9 there is no trend in the time since quenching onset with the relative velocity of the satellites to their corresponding central and a steeper trend with  $R/R_{200}$  for lower mass satellites in larger mass halos. This suggests that whatever environmental mechanism is at play here, it is dependant on the size of the halo, either

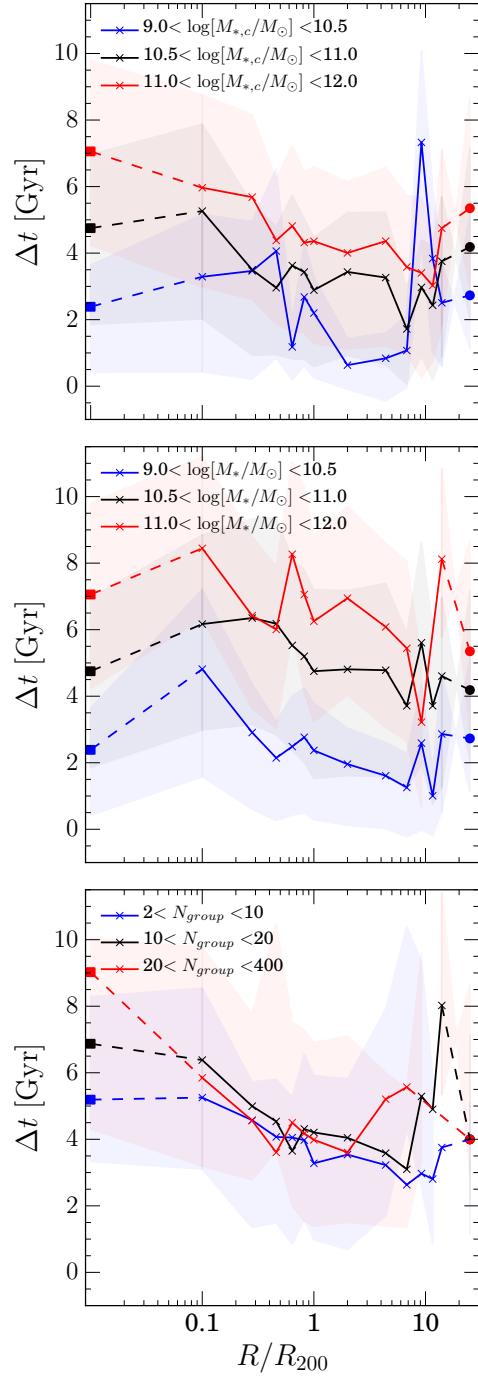


Figure 5.8: The time since quenching onset ( $\Delta t = t_{obs} - t_q$ ) binned in projected cluster centric radius, normalised by  $R_{200}$ , for satellite galaxies (triangles) split by stellar mass of the corresponding central galaxy (top), stellar mass (middle) and the number of galaxies within the group (bottom). The corresponding values for central galaxies (squares) and galaxies in the GZ-CENT-FIELD sample (circles) are shown and connected by the dashed lines to aid the reader.

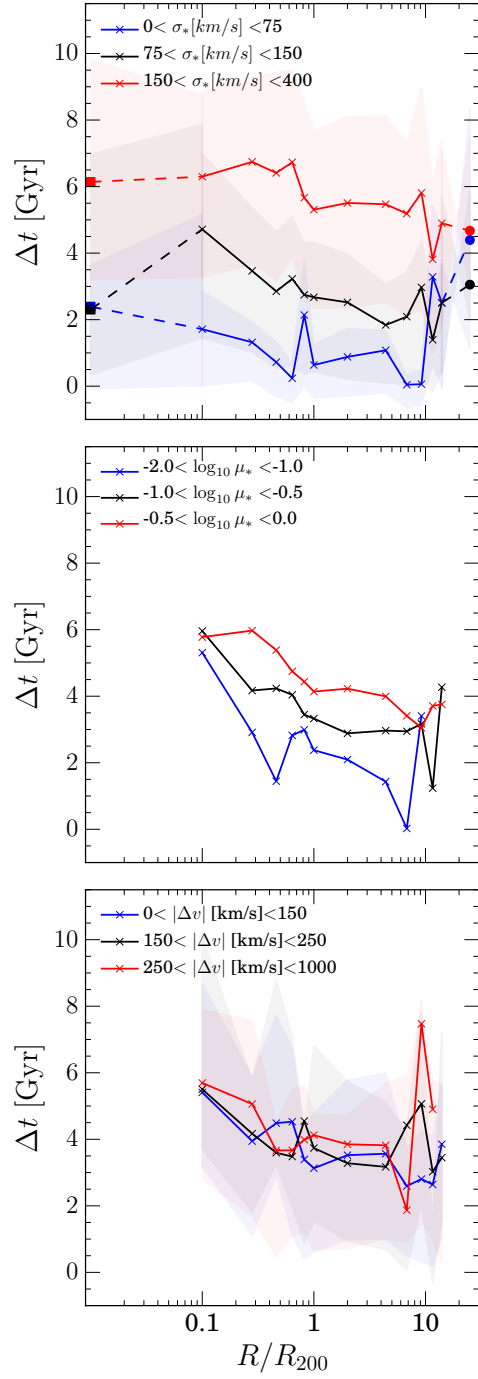


Figure 5.9: The time since quenching onset ( $\Delta t = t_{\text{obs}} - t_q$ ) binned in projected cluster centric radius, normalised by  $R_{200}$ , for satellite galaxies (triangles) split by velocity dispersion (top), stellar mass ratio ( $\mu_* = M_*/M_{*,c}$ ) (middle) and the difference in velocity from the associated central galaxy (bottom). The corresponding values for central galaxies (squares) and galaxies in the GZ-CENT-FIELD sample (circles) are shown and connected by the dashed lines to aid the reader in the top panel where appropriate.

due to the potential or temperature of the halo, but not dependant on the speed of the satellite. This suggests that ram pressure stripping is not the dominant environmental quenching mechanism at play.

We have shown that mergers are important for centrals not for satellites in the bottom panel of Figure 5.8. That mass quenching is important for satellites as well as centrals in the middle panel of Figure 5.8 and that larger halos have a stronger environmental effect on their satellites in the top panel of Figure 5.8.

# Chapter 6

## Discussion

In Section 4.1.3 we have discussed how our results of the changing morphological features and quenching timescales with projected cluster centric radius in the group environment show evidence for both merger driven, secular and environmentally driven evolutionary histories. This suggests that not one mechanism is dominant in the group environment but that a superposition of all these effects gives rise to the observed morphology-density and morphology-SFR relations.

All these mechanisms are striving towards the same end result with no single mechanisms dominating over the other. Those mechanisms traditionally associated with the field, such as secular evolution can also occur in more dense environments, however will often eventually be overwhelmed by those more rapid and violent mechanisms of mergers and interactions (and the triggered outflows from AGN that are associated with such mechanisms; see Smethurst et al. 2016). Similarly, the environmental quenching mechanisms are at work as soon as a galaxy falls into a group or cluster, but such a process can be interrupted momentarily by an interaction or a merger as a galaxy enters the more dense environment.

Just as morphology is a spectrum from disc-dominated to spheroid-dominated systems, so to are the quenching mechanisms which cause this morphological transformation. Mergers and interactions are a spectrum of mass ratios from the micro mergers (?) through to major mergers, with increasing impact upon the morphology and SFR of a galaxy. Secular quenching mechanisms are a spectrum of stellar mass, with a larger impact on those galaxies with smaller masses. Environmental quenching mechanisms are a spectrum of increasing halo potential, giving rise to a stronger

impact on the SFR of smaller mass galaxies in larger halos.

All of these mechanisms coalesce will give rise to the distributions in galaxy properties we see across the Universe through their constant interplay across cosmic time.

# Chapter 7

## Conclusions

### 7.1 Summary

Quenching is morphologically dependant.

AGN may be responsible for some of this quenching.

The environment plays less of a role than typical mass quenching.

### 7.2 Future Work

In reality, there are many possible forms of SFH that a galaxy can take, a few of which have been investigated in previous literature; starbursts (Canalizo & Stockton, 2001), a power law (Glazebrook et al., 2003), single stellar populations (Trager et al., 2000; Sánchez-Blázquez et al., 2006; Vazdekis et al., 2010), log-normal distributions (Abramson et al., 2016) and metallicity enrichment (De Lucia et al., 2014). Incorporating these different SFHs along with prescriptions for mergers and a possible reinvigoration of star formation post quench (e.g. see recent work by Pontzen et al. 2016) into the SFH models is a possible future extension to this work once the results of this study are well enough understood to permit additional complexity to be added.

# Bibliography

- Abramson L. E., Gladders M. D., Dressler A., Oemler A., Poggianti B., Vulcani B., 2016, ArXiv e-prints, 1604.00016
- Ahn C. P. et al., 2012, ApJS, 203, 21
- Aird J. et al., 2012, ApJ, 746, 90
- Arnouts S. et al., 2007, A&A, 476, 137
- Astropy Collaboration et al., 2013, A&A, 558, A33
- Azadi M. et al., 2016, ArXiv e-prints, 1608.05890
- Baldry I. K., Balogh M. L., Bower R. G., Glazebrook K., Nichol R. C., Bamford S. P., Budavari T., 2006, MNRAS, 373, 469
- Baldry I. K., Glazebrook K., Brinkmann J., Ivezić Ž., Lupton R. H., Nichol R. C., Szalay A. S., 2004, ApJ, 600, 681
- Baldwin J. A., Phillips M. M., Terlevich R., 1981, PASP, 93, 5
- Ball N. M., Loveday J., Brunner R. J., 2008, MNRAS, 383, 907
- Bamford S. P. et al., 2009, MNRAS, 393, 1324
- Barro G. et al., 2013, ApJ, 765, 104
- Barth A. J. et al., 2015, ApJS, 217, 26
- Bell E. F., de Jong R. S., 2001, ApJ, 550, 212
- Bell E. F., Phleps S., Somerville R. S., Wolf C., Borch A., Meisenheimer K., 2006, ApJ, 652, 270

- Bell E. F. et al., 2004, ApJ, 608, 752
- Bell E. F., Zheng X. Z., Papovich C., Borch A., Wolf C., Meisenheimer K., 2007, ApJ, 663, 834
- Benson A. J., Bower R. G., Frenk C. S., Lacey C. G., Baugh C. M., Cole S., 2003, ApJ, 599, 38
- Berlind A. A. et al., 2006, ApJS, 167, 1
- Béthermin M. et al., 2012, ApJ, 757, L23
- Binney J., Merrifield M., 1998, Galactic astronomy. Galactic astronomy / James Binney and Michael Merrifield. Princeton, NJ : Princeton University Press, 1998. (Princeton series in astrophysics) QB857 .B522 1998 (\$35.00)
- Bower R. G., Benson A. J., Malbon R., Helly J. C., Frenk C. S., Baugh C. M., Cole S., Lacey C. G., 2006, MNRAS, 370, 645
- Bower R. G., Lucey J. R., Ellis R. S., 1992, MNRAS, 254, 601
- Brammer G. B. et al., 2009, ApJ, 706, L173
- Brinchmann J., Charlot S., White S. D. M., Tremonti C., Kauffmann G., Heckman T., Brinkmann J., 2004, MNRAS, 351, 1151
- Brinchmann J., Ellis R. S., 2000, ApJ, 536, L77
- Bruzual G., Charlot S., 2003, MNRAS, 344, 1000
- Buat V. et al., 2005, ApJ, 619, L51
- Bundy K. et al., 2015, ApJ, 798, 7
- Bundy K., Treu T., Ellis R. S., 2007, ApJ, 665, L5
- Canalizo G., Stockton A., 2001, ApJ, 555, 719
- Chabrier G., 2003, PASP, 115, 763
- Chen X. Y., Liang Y. C., Hammer F., Prugniel P., Zhong G. H., Rodrigues M., Zhao Y. H., Flores H., 2010, A&A, 515, A101
- Chester C., Roberts M. S., 1964, AJ, 69, 635

- Cheung E. et al., 2013, ApJ, 779, 162
- Cheung E. et al., 2012, ApJ, 760, 131
- Cisternas M. et al., 2011, ApJ, 741, L11
- Coil A. L. et al., 2008, ApJ, 672, 153
- Cole S. et al., 2001, MNRAS, 326, 255
- Conroy C., Gunn J. E., White M., 2009, ApJ, 699, 486
- Conselice C. J., Bershady M. A., Dickinson M., Papovich C., 2003, AJ, 126, 1183
- Constantin A., Hoyle F., Vogeley M. S., 2008, ApJ, 673, 715
- Cowie L. L., Barger A. J., 2008, ApJ, 686, 72
- Cowie L. L., Songaila A., Hu E. M., Cohen J. G., 1996, AJ, 112, 839
- Cowley M. J. et al., 2016, MNRAS, 457, 629
- Croom S. M. et al., 2012, MNRAS, 421, 872
- Croton D. J. et al., 2006, MNRAS, 365, 11
- Daddi E. et al., 2007, ApJ, 670, 156
- Daddi E. et al., 2010, ApJ, 714, L118
- Darg D. W. et al., 2010, MNRAS, 401, 1043
- De Lucia G., Tornatore L., Frenk C. S., Helmi A., Navarro J. F., White S. D. M., 2014, MNRAS, 445, 970
- de Vaucouleurs G., 1953, MNRAS, 113, 134
- Di Matteo T., Springel V., Hernquist L., 2005, Nature, 433, 604
- Dressler A., 1980, ApJ, 236, 351
- Driver S. P. et al., 2006, MNRAS, 368, 414
- Edelson R., Malkan M., 2012, ApJ, 751, 52
- Elbaz D. et al., 2007, A&A, 468, 33

- Elvis M., Risaliti G., Zamorani G., 2002, ApJ, 565, L75
- Eminian C., Kauffmann G., Charlot S., Wild V., Bruzual G., Rettura A., Loveday J., 2008, MNRAS, 384, 930
- Emsellem E., Renaud F., Bournaud F., Elmegreen B., Combes F., Gabor J. M., 2015, MNRAS, 446, 2468
- Faber S. M. et al., 2007, ApJ, 665, 265
- Fabian A. C., 2012, ARA&A, 50, 455
- Falkenberg M. A., Kotulla R., Fritze U., 2009, MNRAS, 397, 1954
- Fang J. J., Faber S. M., Koo D. C., Dekel A., 2013, ApJ, 776, 63
- Foreman-Mackey D., Hogg D. W., Lang D., Goodman J., 2013, PASP, 125, 306
- Gabor J. M. et al., 2009, ApJ, 691, 705
- Gelman A., Roberts G., Gilks W., 1996, Bayesian statistics 5. Oxford University Press, pp. 599–607
- Genel S. et al., 2008, ApJ, 688, 789
- Glazebrook K. et al., 2003, ApJ, 587, 55
- Gonçalves T. S., Martin D. C., Menéndez-Delmestre K., Wyder T. K., Koekemoer A., 2012, ApJ, 759, 67
- González V., Labb   I., Bouwens R. J., Illingworth G., Franx M., Kriek M., Brammer G. B., 2010, ApJ, 713, 115
- Goodman J., Weare J., 2010, CAMCS, 5, 65
- Goulding A. D., Alexander D. M., 2009, MNRAS, 398, 1165
- Graham A. W., 2001, AJ, 121, 820
- Graham A. W., 2007, MNRAS, 379, 711
- Greene J. E., Ho L. C., 2007, ApJ, 670, 92
- Haines T., McIntosh D. H., S  nchez S. F., Tremonti C., Rudnick G., 2015, MNRAS, 451, 433

- Häring N., Rix H.-W., 2004, ApJ, 604, L89
- Harrison C. M. et al., 2016, MNRAS, 456, 1195
- Hayward C. C., Torrey P., Springel V., Hernquist L., Vogelsberger M., 2014, MNRAS, 442, 1992
- Heckman T. M., Kauffmann G., Brinchmann J., Charlot S., Tremonti C., White S. D. M., 2004, ApJ, 613, 109
- Heinis S. et al., 2014, MNRAS, 437, 1268
- Hickox R. C. et al., 2009, ApJ, 696, 891
- Hopkins P. F., Cox T. J., Kereš D., Hernquist L., 2008a, ApJS, 175, 390
- Hopkins P. F., Hernquist L., Cox T. J., Kereš D., 2008b, ApJS, 175, 356
- Huang J.-S., Glazebrook K., Cowie L. L., Tinney C., 2003, ApJ, 584, 203
- Ishibashi W., Fabian A. C., 2012, MNRAS, 427, 2998
- Jahnke K., Macciò A. V., 2011, ApJ, 734, 92
- Jiang Y.-F., Greene J. E., Ho L. C., 2011, ApJ, 737, L45
- Kauffmann G., Heckman T. M., 2009, MNRAS, 397, 135
- Kauffmann G. et al., 2003a, MNRAS, 346, 1055
- Kauffmann G. et al., 2003b, MNRAS, 341, 33
- Kauffmann G., White S. D. M., Heckman T. M., Ménard B., Brinchmann J., Charlot S., Tremonti C., Brinkmann J., 2004, MNRAS, 353, 713
- Kaviraj S., 2014a, MNRAS, 440, 2944
- Kaviraj S., 2014b, MNRAS, 437, L41
- Kaviraj S. et al., 2013, MNRAS, 428, 925
- Kaviraj S., Tan K.-M., Ellis R. S., Silk J., 2011, MNRAS, 411, 2148
- Kelly B. C., 2007, ApJ, 665, 1489

- Kennicutt R. C., 1997, in Astrophysics and Space Science Library, Vol. 161, Astrophysics and Space Science Library, pp. 171–195
- Kennicutt, Jr. R. C., Roettiger K. A., Keel W. C., van der Hulst J. M., Hummel E., 1987, AJ, 93, 1011
- Kewley L. J., Groves B., Kauffmann G., Heckman T., 2006, MNRAS, 372, 961
- Kewley L. J., Heisler C. A., Dopita M. A., Lumsden S., 2001, ApJS, 132, 37
- Ko J., Hwang H. S., Lee J. C., Sohn Y.-J., 2013, ApJ, 767, 90
- Kocevski D. D. et al., 2012, ApJ, 744, 148
- Kochanek C. S. et al., 2001, ApJ, 560, 566
- Kormendy J., Drory N., Bender R., Cornell M. E., 2010, ApJ, 723, 54
- Kormendy J., Gebhardt K., 2001, in AIP Conf. Proc. 586: 20th Texas Symposium on relativistic astrophysics, pp. 363–+
- Kormendy J., Kennicutt, Jr. R. C., 2004, ARA&A, 42, 603
- Koss M., Mushotzky R., Veilleux S., Winter L. M., Baumgartner W., Tueller J., Gehrels N., Valencic L., 2011, ApJ, 739, 57
- Kriek M. et al., 2010, ApJ, 722, L64
- Lahav O., Bridle S. L., Hobson M. P., Lasenby A. N., Sodré L., 2000, MNRAS, 315, L45
- Lintott C. et al., 2011, MNRAS, 410, 166
- Lintott C. J. et al., 2009, MNRAS, 399, 129
- Lintott C. J. et al., 2008, MNRAS, 389, 1179
- Lotz J. M., Jonsson P., Cox T. J., Croton D., Primack J. R., Somerville R. S., Stewart K., 2011, ApJ, 742, 103
- Lotz J. M., Jonsson P., Cox T. J., Primack J. R., 2008, MNRAS, 391, 1137
- Mackay D. J. C., 2003, Information Theory, Inference and Learning Algorithms. p. 640

- Magorrian J. et al., 1998, AJ, 115, 2285
- Marasco A., Fraternali F., Binney J. J., 2012, MNRAS, 419, 1107
- Maraston C., 2005, MNRAS, 362, 799
- Marconi A., Hunt L. K., 2003, ApJ, 589, L21
- Martin D. C. et al., 2007, ApJS, 173, 342
- Masters K. L. et al., 2010a, MNRAS, 405, 783
- Masters K. L. et al., 2010b, MNRAS, 404, 792
- Masters K. L. et al., 2012, MNRAS, 424, 2180
- Masters K. L. et al., 2011, MNRAS, 411, 2026
- McConnell N. J., Ma C.-P., Gebhardt K., Wright S. A., Murphy J. D., Lauer T. R., Graham J. R., Richstone D. O., 2011, Nature, 480, 215
- McIntosh D. H. et al., 2014, MNRAS, 442, 533
- McLure R. J., Dunlop J. S., 2001, MNRAS, 327, 199
- McLure R. J., Kukula M. J., Dunlop J. S., Baum S. A., O'Dea C. P., Hughes D. H., 1999, MNRAS, 308, 377
- Melbourne J. et al., 2012, ApJ, 748, 47
- Mendez A. J. et al., 2013, ApJ, 770, 40
- Mendez A. J., Coil A. L., Lotz J., Salim S., Moustakas J., Simard L., 2011, ApJ, 736, 110
- Miner J., Rose J. A., Cecil G., 2011, ApJ, 727, L15
- Nair P. B., Abraham R. G., 2010, ApJL, 714, L260L264
- Nandra K. et al., 2007, ApJ, 660, L11
- Noeske K. G. et al., 2007, ApJ, 660, L43
- Oh K., Yi S. K., Schawinski K., Koss M., Trakhtenbrot B., Soto K., 2015, ApJS, 219, 1

- Pan Z., Li J., Lin W., Wang J., Kong X., 2014, ApJ, 792, L4
- Peng C. Y., Ho L. C., Impey C. D., Rix H.-W., 2002, AJ, 124, 266
- Peng C. Y., Ho L. C., Impey C. D., Rix H.-W., 2010, AJ, 139, 2097
- Peng Y.-j., Lilly S. J., Renzini A., Carollo M., 2012, ApJ, 757, 4
- Peterson B. M., 2014, Space Sci. Rev., 183, 253
- Pierce C. M. et al., 2007, ApJ, 660, L19
- Pimbblet K. A., Shabala S. S., Haines C. P., Fraser-McKelvie A., Floyd D. J. E., 2013, MNRAS, 429, 1827
- Pontzen A., Tremmel M., Roth N., Peiris H. V., Saintonge A., Volonteri M., Quinn T., Governato F., 2016, ArXiv e-prints, 1607.02507
- Richards G. T. et al., 2006, ApJS, 166, 470
- Sánchez S. F. et al., 2004, ApJ, 614, 586
- Saintonge A. et al., 2012, ApJ, 758, 73
- Salim S. et al., 2007, ApJS, 173, 267
- Sánchez S. F. et al., 2012, A&A, 538, A8
- Sánchez-Blázquez P., Gorgas J., Cardiel N., González J. J., 2006, A&A, 457, 809
- Sanders D. B., Soifer B. T., Elias J. H., Madore B. F., Matthews K., Neugebauer G., Scoville N. Z., 1988, ApJ, 325, 74
- Sarzi M. et al., 2006, MNRAS, 366, 1151
- Sarzi M. et al., 2010, MNRAS, 402, 2187
- Schawinski K., Thomas D., Sarzi M., Maraston C., Kaviraj S., Joo S.-J., Yi S. K., Silk J., 2007, MNRAS, 382, 1415
- Schawinski K., Treister E., Urry C. M., Cardamone C. N., Simmons B., Yi S. K., 2011, ApJ, 727, L31+
- Schawinski K. et al., 2014, MNRAS, 440, 889

- Schawinski K. et al., 2010, ApJ, 711, 284
- Schawinski K., Virani S., Simmons B., Urry C. M., Treister E., Kaviraj S., Kushkuley B., 2009, ApJ, 692, L19
- Schiminovich D. et al., 2007, ApJS, 173, 315
- Schlegel D. J., Finkbeiner D. P., Davis M., 1998, ApJ, 500, 525
- Schmidt M., 1959, ApJ, 129, 243
- Scoville N. et al., 2007, ApJS, 172, 1
- Sérsic J. L., 1968, Atlas de galaxias australes. Cordoba, Argentina: Observatorio Astronomico, 1968
- Shen Y., Greene J. E., Strauss M. A., Richards G. T., Schneider D. P., 2008, ApJ, 680, 169
- Shen Y. et al., 2011, ApJS, 194, 45
- Sheth K., Melbourne J., Elmegreen D. M., Elmegreen B. G., Athanassoula E., Abraham R. G., Weiner B. J., 2012, ApJ, 758, 136
- Silk J., Rees M. J., 1998, A&A, 331, L1
- Simard L., 1998, in Astronomical Society of the Pacific Conference Series, Vol. 145, Astronomical Data Analysis Software and Systems VII, Albrecht R., Hook R. N., Bushouse H. A., eds., p. 108
- Simard L., Mendel J. T., Patton D. R., Ellison S. L., McConnachie A. W., 2011, ApJS, 196, 11
- Simmons B. D. et al., 2013, MNRAS, 429, 2199
- Simmons B. D., Urry C. M., 2008, ApJ, 683, 644
- Simmons B. D., Van Duyne J., Urry C. M., Treister E., Koekemoer A. M., Grogin N. A., The GOODS Team, 2011, ApJ, 734, 121
- Singh R. et al., 2013, A&A, 558, A43
- Sivia D., Skilling J., 2006, Data Analysis: A Bayesian Tutorial, Oxford science publications. OUP Oxford

- Skibba R. A. et al., 2009, MNRAS, 399, 966
- Skrutskie M. F. et al., 2006, AJ, 131, 1163
- Smethurst R. J. et al., 2016, MNRAS
- Smethurst R. J. et al., 2015, MNRAS, 450, 435
- Snyder G. F., Cox T. J., Hayward C. C., Hernquist L., Jonsson P., 2011, ApJ, 741, 77
- Somerville R. S., Hopkins P. F., Cox T. J., Robertson B. E., Hernquist L., 2008, MNRAS, 391, 481
- Sparre M., Springel V., 2016, MNRAS, 462, 2418
- Springel V., Di Matteo T., Hernquist L., 2005, ApJ, 620, L79
- Stern D. et al., 2005, ApJ, 631, 163
- Strateva I. et al., 2001, AJ, 122, 1861
- Thomas D., Maraston C., Schawinski K., Sarzi M., Silk J., 2010, MNRAS, 404, 1775
- Tojeiro R., Heavens A. F., Jimenez R., Panter B., 2007, MNRAS, 381, 1252
- Tojeiro R. et al., 2013, MNRAS, 432, 359
- Tortora C., Antonuccio-Delogu V., Kaviraj S., Silk J., Romeo A. D., Becciani U., 2009, MNRAS, 396, 61
- Trager S. C., Faber S. M., Worthey G., González J. J., 2000, AJ, 120, 165
- Tremonti C. A. et al., 2004, ApJ, 613, 898
- Urry C. M., Scarpa R., O'Dowd M., Falomo R., Pesce J. E., Treves A., 2000, ApJ, 532, 816
- van der Wel A., Rix H.-W., Holden B. P., Bell E. F., Robaina A. R., 2009, ApJ, 706, L120
- Varela J., Moles M., Márquez I., Galletta G., Masegosa J., Bettoni D., 2004, A&A, 420, 873

- Vazdekis A., Sánchez-Blázquez P., Falcón-Barroso J., Cenarro A. J., Beasley M. A., Cardiel N., Gorgas J., Peletier R. F., 2010, MNRAS, 404, 1639
- Voges W. et al., 1999, A&A, 349, 389
- Weiner B. J. et al., 2006, ApJ, 653, 1049
- Wild V., Walcher C. J., Johansson P. H., Tresse L., Charlot S., Pollo A., Le Fèvre O., de Ravel L., 2009, MNRAS, 395, 144
- Willett K. W. et al., 2013, MNRAS, 435, 2835
- Willmer C. N. A. et al., 2006, ApJ, 647, 853
- Wong O. I. et al., 2012, MNRAS, 420, 1684
- Wright E. L. et al., 2010, AJ, 140, 1868
- Wyder T. K. et al., 2007, ApJS, 173, 293
- Xiao T., Barth A. J., Greene J. E., Ho L. C., Bentz M. C., Ludwig R. R., Jiang Y., 2011, ApJ, 739, 28
- Yan R., Blanton M. R., 2012, ApJ, 747, 61
- Yesuf H. M., Faber S. M., Trump J. R., Koo D. C., Fang J. J., Liu F. S., Wild V., Hayward C. C., 2014, ApJ, 792, 84
- York D. G. et al., 2000, AJ, 120, 1579
- Zinn P.-C., Middelberg E., Norris R. P., Dettmar R.-J., 2013, ApJ, 774, 66